

ANNEXES:

Deliverable 2.7 Geological Models - EBRO

BASIN SPAIN

WP2

Release Status:

Author: : I. Moreno, J. García, J. F. Mediato, P. Fernández-Canteli, B. Benjumea, F. Rubio, C. Ayala, D. M. García, J. Martínez, C. Rey, P. Clariana, B. del Moral, E. R. Berrezueta, B. Ordóñez, E. Fernández de Arévalo, R. Soto, J. López, A. García, J. M. Llorente, M. Castillo, E. Pueyo

Date: July 2023

Filename and Version: Project ID Number: 101022664

PilotSTRATEGY (H2020- Topic LC-SC3-NZE-6-2020 - RIA)

1. Document History

1.1 Location

This document is stored in the following location:

Filename	
Location	

1.2 Revision History

This document has been through the following revisions:

Version No.	Revision Date	Filename/Location stored:	Brief Summary of Changes

1.3 Authorisation

This document requires the following approvals:

AUTHORISATION	Name	Signature	Date
WP Leader	Mark Wilkinson		DD/MM/YY
Project Coordinator	Fernanda de Mesquita Lobo Veloso		DD/MM/YY

For Deliverables, the Project Coordinator should receive the final version at least one week prior to the due date.

1.4 Distribution

document has been distributed to:

Name	Title	Version Issued	Date of Issue
			00/00/0000

© European Union, 2023

No third-party textual or artistic material is included in the publication without the copyright holder's prior consent to further dissemination by other third parties.

Reproduction is authorised provided the source is acknowledged.

Disclaimer [to be added to any public deliverables]

The information and views set out in this [report/study/article/publication...] are those of the author(s) and do not necessarily reflect the official opinion of the European Union. Neither the European Union institutions and bodies nor any person acting on their behalf may be held responsible for the use which may be made of the information contained therein.



1. Document History.....	1
1.1 Location.....	1
1.2 Revision History.....	1
1.3 Authorisation.....	1
1.4 Distribution	1
9. Annex.....	5
9.1 Structural context review of the Area of Interest	5
9.1.1 Geological setting and main characteristics of the study area.....	5
9.1.2 Tectonic evolution of the study area	8
9.1.3 Structures of the Iberian deformation front	9
9.2 Faults interpretation in the area of interest.....	12
9.2.1 Structural interpretation.....	12
9.2.2 Tectonic evolution of the study area.....	16
9.2.3 Partial reactivation in the study area during the Alpine compression	18
9.3 Geophysical Models Implementation.....	19
9.3.1 Methodology used in implementation of the Geophysical models	19
9.3.2 Interpretation	29
9.4 Logs and well data analysis	45
9.4.1 Methodology Introduction	45
9.4.2 Reservoir Pressure and Temperature Assessment.....	47
9.4.3 Log analysis methodology	48
9.4.4 Reservoir Pressure and Temperature Assessment.....	54
9.4.5 Logs analysis	57
9.5 Well-Seismic stratigraphic correlation.....	68
9.6 Time-Depth Conversion	72
9.7 Reservoir Facies	74
9.7.1 Stratigraphy	74
9.7.2 Reservoir Architecture	81
9.7.3 Reservoir Properties	81
9.8 Seal Facies	86
9.8.1 Stratigraphy	86
9.8.2 Seal Properties.....	87

9.9	Surface Data	87
10.	Depositional environments and geological conceptual model	87
10.1	Field Analogues.....	88
11.	References.....	89



9. Annex

9.1 Structural context review of the Area of Interest

9.1.1 Geological setting and main characteristics of the study area

The study area is situated near the southern edge of the Ebro basin, which is located in the northeastern region of the Iberian Peninsula (Figure 9-1 a). In particular, the study area lies near the northern boundary of the Aragonese branch of the Iberian Chain. This basin has a triangular shape and serves as the foreland basin for the Pyrenees, Iberian Chain, and Catalan Coastal Ranges located north, south, and east, respectively (Figure 9-1 b). The formation of the foreland basin commenced during the Paleocene, induced by flexural subsidence resulting from the development of these three mountain ranges (e.g. Pardo et al., 2004). Towards the central part of the Ebro Basin, the structure corresponds to a gentle syncline (the Ebro syncline, Quirantes, 1978) (Figure 9-1 b), which was interpreted, based on surface (mapping and structural data) and subsurface (wells and seismic reflection data) data, as a bending fold that accommodated the slight reactivation of WNW-ESE basement faults originated at the beginning of the Mesozoic extension (Arlegui and Simón, 2001).

Cenozoic deposits with subhorizontal bedding are the predominant feature of the Ebro basin's surface. Deformation caused by thrusting and folding in the Cenozoic autochthonous deposits of the Ebro basin is only visible at the margins of the basin, with the deformation varying from thin-skinned at the Pyrenean margin to thick-skinned at the Iberian and Catalan margins (e.g. Cortés and Casas, 1999; Soto et al. 2016). The youngest Neogene sediments lie flat and unconformably upon older rocks (Cortés and Casas, 1999; Pardo et al., 2004). Subsurface data reveal the presence of several structures inside the Ebro basin that affect the Paleozoic and Mesozoic rocks below the subhorizontal Cenozoic deposits. According to Klimowitz (1992), tectonic activity might have even influenced Lower Miocene rocks. These structures are aligned parallel to the Iberian and Catalan deformation fronts, oriented NW–SE and NE–SW, respectively (Arlegui and Simón, 2001; Butillé et al., 2012; Mediato et al., 2017; Izquierdo-Llaval et al., 2019) (Figure 9-1 c).

The sedimentary register of the study area has been analysed by means of the following wells: Lopín-1, La Zaida-1, Monegrillo-1, Ebro-1 and Caspe-1 (see information of wells in Lanaja, 1987 and Arenillas et al., 2014) (Figure 9-2 and Figure 9-3). The underlying basement is formed by rocks from the Paleozoic, the majority of which have undergone deformation and metamorphism during the Late Carboniferous Variscan orogeny (Ábalos et al., 2002). Above the Variscan basement, Triassic sediments display the typical Germanic facies, including Buntsandstein red beds, Muschelkalk dolostones, limestones, and evaporites and Keuper evaporites and shales. The Buntsandstein facies, which represent the target reservoir series, exhibit detrital sedimentation. Three different Triassic evaporitic sequences characterize the sedimentary pile at this sector: (i) a thin basal evaporite layer up to 30 meters (Röt facies), (ii) a thick succession of Middle Triassic evaporites (M2, middle Muschelkalk facies) up to 325 m, and (iii) up to 400 m thick succession of continental evaporites and fine clastics Late Triassic in age (Keuper facies) (Jurado, 1990; Ortí et al., 2017). These Middle and Upper Triassic evaporitic successions might serve as potential secondary seals. The oldest Jurassic rocks of the Ebro Basin constitute 50 m of dolomites overlain by a cyclic anhydrite unit bearing dolomitic interbeds (Lécera Fm) with a total thickness of 200 – 450 m (Jurado, 1990; Gómez et al., 2007).

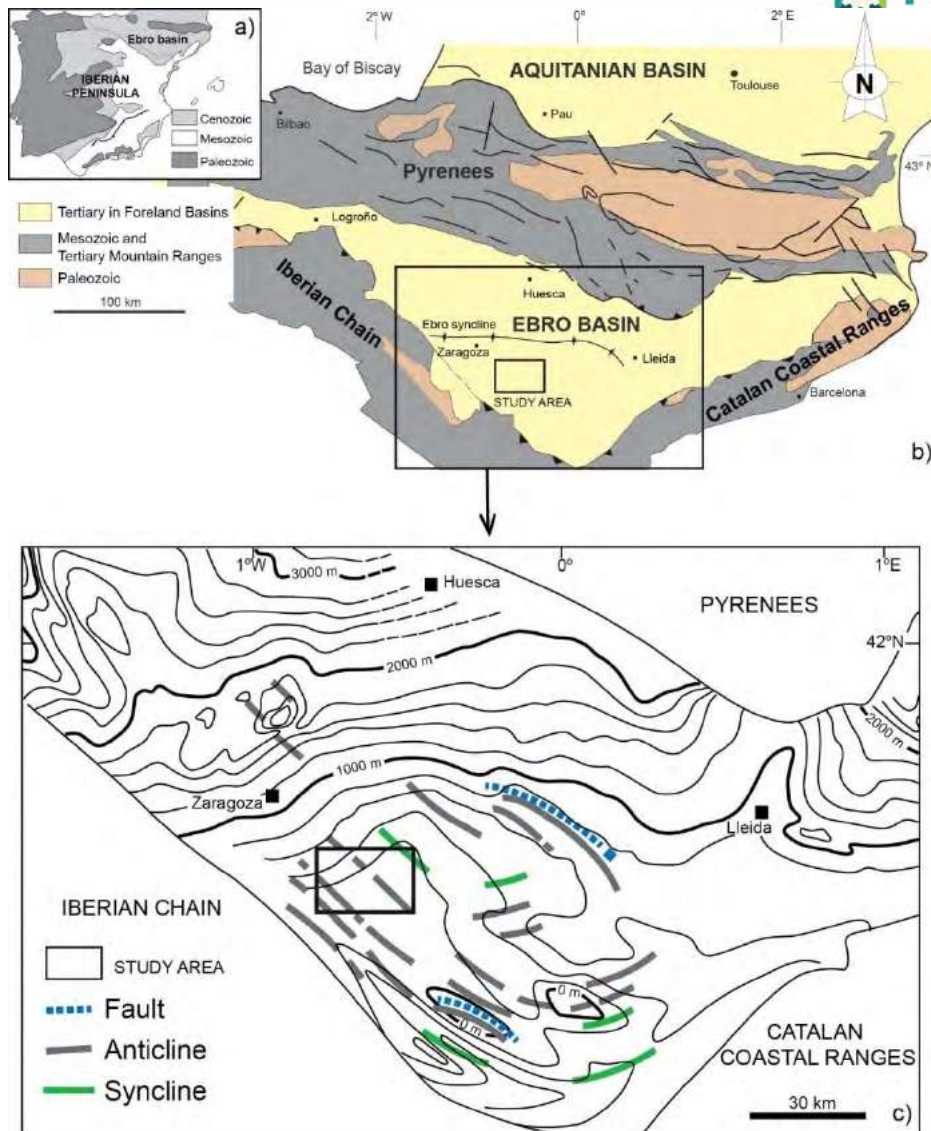


Figure 9-1 a) Simplified geological sketch of the Iberian Peninsula (from Soto et al., 2009). b) Geological sketch of the northeastern part of Iberia showing the study area in the central part of the Ebro basin and the Alpine ranges (modified from Soto et al., 2016). c) Contour map of the base of the Cenozoic sequence (modified from ITGE, 1990), and major structures in the Paleozoic, Mesozoic and Paleogene deduced from Klimowitz (1992) (modified from Soto et al., 2016).

This sequence is, in turn, overlaid by up to 300 m thick succession comprising several shallow platform carbonate sequences. This succession contains dolomites, limestones and limestones with interbedded marls, it is overlaid by continental carbonate and detrital Cretaceous deposits. Early Cretaceous strata are characterized by strong variations linked to deformation during a rifting period (García-Quintana, 1977). The base of the Cenozoic rocks is unconformable. This erosional surface cuts the Cretaceous and Jurassic deposits. The Cenozoic succession is made of continental evaporitic and detrital sequences.

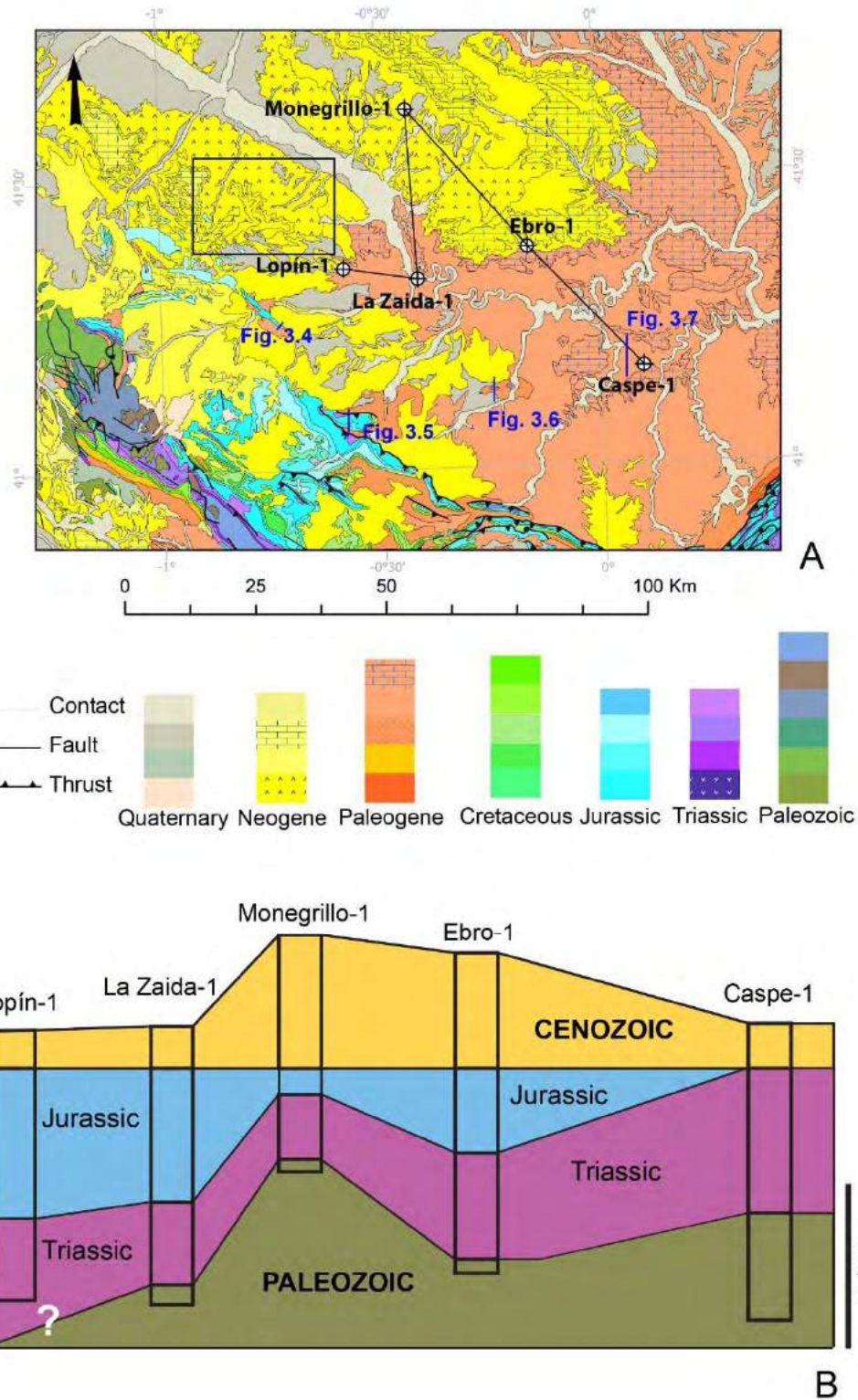


Figure 9-2 a) Geological map of the southern Ebro basin showing the location of the study area and the location of wells Lopín-1, La Zaida-1, Monegrillo-1, Ebro-1 and Caspe-1. b) Sketch showing the rocks in terms of age crossed by the above mentioned wells.

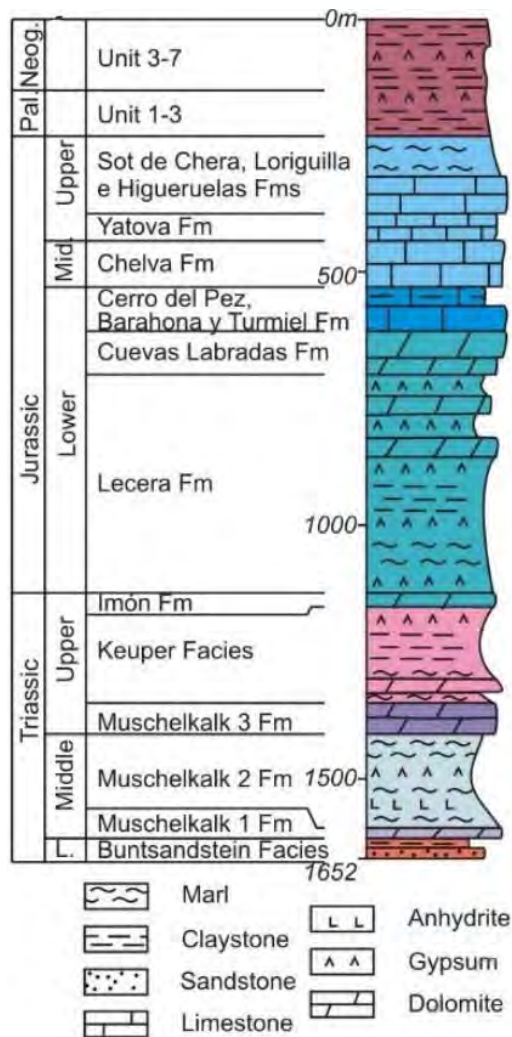


Figure 9-3 Stratigraphic column of Lopin-1 well.

9.1.2 Tectonic evolution of the study area

The geodynamic evolution of the northeastern part of the Iberian Peninsula is rather complex. The structural features of the Iberian Chain have been largely analysed due to the presence of suitable outcrops of very good quality. However, the tectonic evolution of the Ebro basin before its foreland stage has not been extensively studied. Recent kinematic reconstructions have interpreted the Ebro area as a continental block named the Ebro block during the Mesozoic (e.g. Tugend et al., 2014; Angrand et al., 2020; King et al., 2023).

The Variscan Orogeny in northeast Iberia took place in Middle-Late Carboniferous (i.e. Pyrenees, Iberian Chain) (e.g. Vera, 2004). During the Mesozoic, in northeast Iberia, a generalized extension took place in two rifting stages: a first rifting stage during the Permian and Triassic and a second one during the Late Jurassic and Early Cretaceous (e.g. Sopena et al., 1988; Salas et al., 2001). The collision between the Iberian and European plates from the Late Cretaceous to Miocene during the Alpine Orogeny caused the inversion of previous Variscan and Mesozoic structures (e.g. Casas-Sainz and Faccenna, 2001). This last compressive period originated the Ebro basin as a foreland basin (e.g. Arlegui and Simón, 2001).

9.1.3 Structures of the Iberian deformation front

In the proximity of the study area several structures mark the boundary of the Iberian Chain (see location in Figure 9-2a). They consist of north-verging folds and thrusts trending E-W to NW-SE (Guimerá and Álvaro, 1990). In this sector, the deformation shows a mechanical coupling between the Paleozoic basement and cover rocks (thick skinned deformation) or decoupling resulting from the presence of an Upper Triassic detachment level (thin skinned deformation) (Cortés and Casas, 1996; Soto et al. 2016). Most of these structures were formed from the Late Eocene to Early Miocene according to tectonic-sedimentary relationships (Cortés and Casas, 1999; Casas-Sainz and Faccenna, 2001).

Belchite anticline

The Belchite anticline is a NW-SE trending northeast verging fold located 17 km south of the area of interest. It is 12 km long and has an average width of 0.5 km. Its geometry could correspond to a detachment fold but also to a fault-propagation fold because neither the thrust fault nor the detachment level outcrops (Cortés and Casas, 1999). The fold affects Upper Triassic, Lower-Middle Jurassic and sin-orogenic Cenozoic materials. Lower-Middle Miocene materials of the Ebro basin lie unconformably above strata of previous units. The SW limb of this anticline dips between 30 - 70° to the southwest while the north limb is steep to overturned (Figure 9-4). Moreover, minor folds related to detachment levels develop in the Jurassic succession in the hinge zone (Cortés and Casas, 1999).

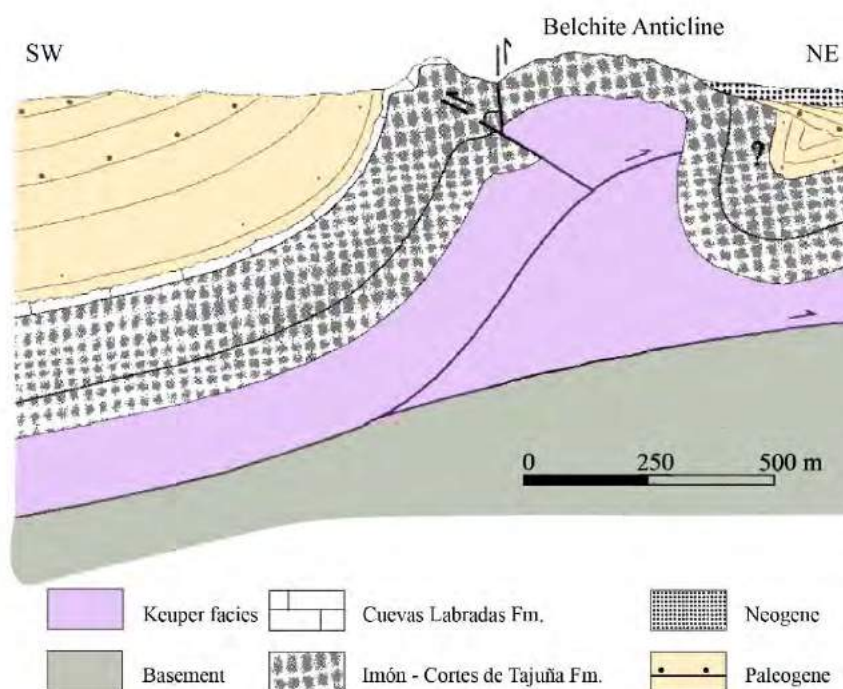


Figure 9-4 Geological cross-section of SE extreme of Belchite anticline (from Cortés and Casas, 1999). See figure 3.2 for the location.

Sierra de Arcos folds and thrusts

The Sierra de Arcos system of folds and thrusts is about 30 km away from the study area and its orientation varies from E-W, in the contact area between the Mesozoic and Cenozoic rocks of the Ebro basin, to NW-SE for the structures located immediately to the south. The thrusts of this

imbricated system emanate from a detachment level located in the Upper Triassic evaporites and nucleated on NW-SE trending basement extensional faults originated during the extensional Mesozoic period (Cortés et al., 1999, Cortés and Casas, 1999) (Figure 9-5).

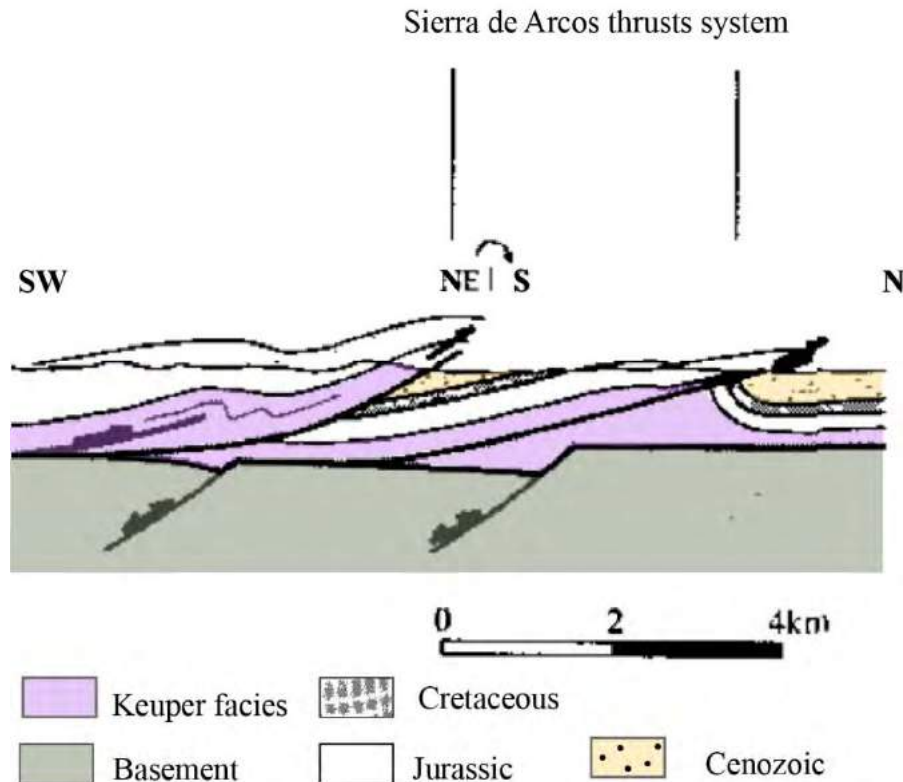


Figure 9-5 Geological cross-section of Sierra de Arcos folds and thrusts (modified from Cortés and Casas, 1999). See figure 3.2 for the location.

Puig Moreno anticline

The small Paleozoic outcrop of Puig Moreno is about 40 km southeast from the interest area and corresponds to an E-W trending anticlinal structure with north vergence that affects Paleozoic basement (Carboniferous rocks) (Villa et al., 1996) and Mesozoic cover (Lower Triassic rocks) (González, 1989; Villena et al., 1992). Its southern limb presents low dips while its north limb is upright (Cuevas-Martínez, 2022). Guimerá (2018) interpreted the Puig Moreno anticline as the superficial expression of the North-Iberian frontal thrust, which is highly attenuated in this area. (Figure 9-6).

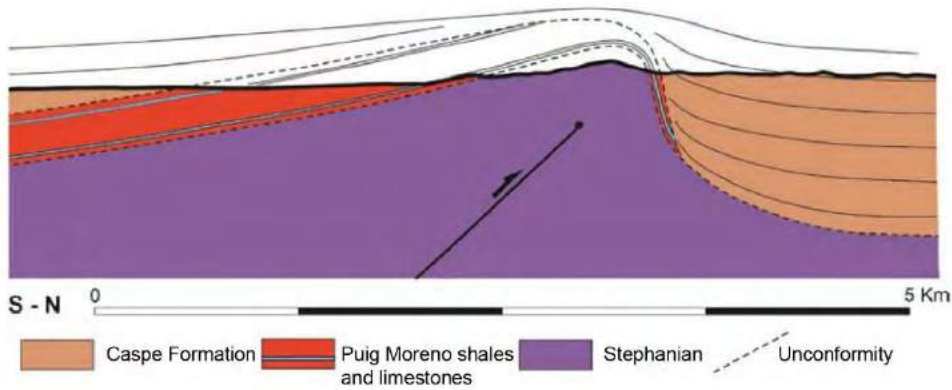


Figure 9-6 Cross-section of Puig Moreno anticline (from Cuevas-Martínez, 2022). See figure 3.2 for location.

Caspé geological structure

The Caspé geological structure corresponds to an anticline identified from surface and mainly subsurface data. It is located about 58 km to the ESE of the Lopín area and to the north of the denominated Linking Zone, where the Aragonese branch of Iberian chain and the Catalan Coastal range meet. This anticline was originated by the Alpine compression of both ranges whose main directions are NW-SE and NE-SW, respectively. The interpretation of seismic profiles allowed identify an anticline structure bounded by ENE-WSW trending thrusts with northward and southward vergence that involved Variscan basement (Mediato et al., 2017). (Figure 9-7).

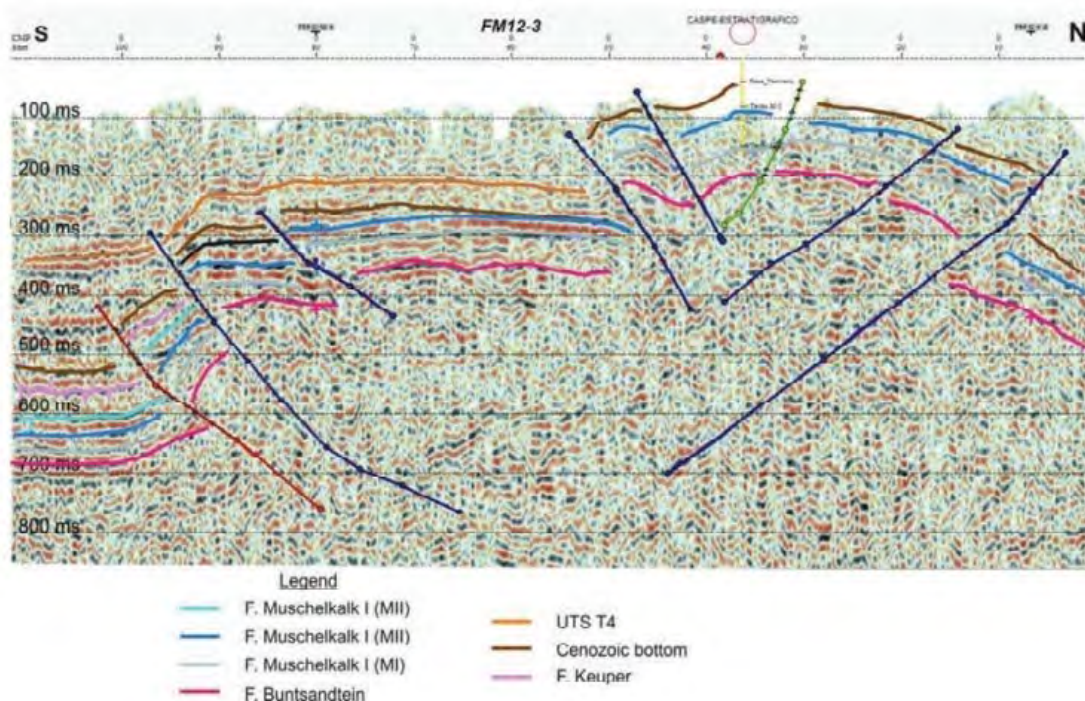


Figure 9-7 Seismic line across the Caspé structure with the interpreted horizons (from Mediato et al., 2017). See Figure 9-2 for location.

9.2 Faults interpretation in the area of interest.

9.2.1 Structural interpretation

The analysis of seismic reflection data, information from the Lopín-1 well and geological maps (Colomer i Guilera et al. 1994; Ramírez-Merino et al., 1991; Ruiz and Lendinez, 1986; Hernández-Samaniego and Ramírez-Merino, 1993) enables the structural interpretation of the study area. Legacy seismic sections were acquired using forty-eight 10 Hz geophones. The geophone and shot spacing range from 40-80 m and 80-160 m, respectively, depending on the profile. Sampling rate was 2 ms. The processing included standard steps such as filtering, deconvolution, static correction and velocity analysis. The sections are not migrated.

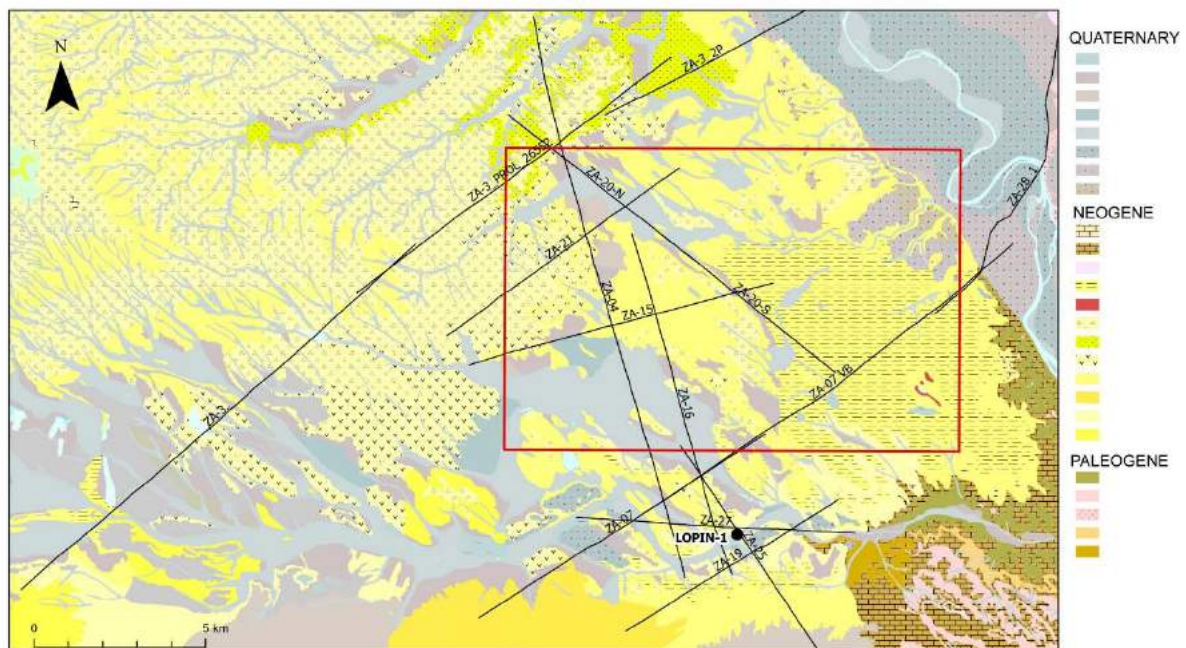


Figure 9-8 Geological map of the interest area with location of seismic lines.

A total of 9 seismic lines were analysed. They are approximately oriented in both SW-NE and NW-SE directions covering about 400 km in total length. The quality and the processing of the seismic sections is low-medium. They are SEG-Y format files vectorised from a TIFF file during the first ALGECO2 phase (García-Lobón et al., 2010). Interpretation of seismic horizons across the studied reflection seismic profiles was possible using the data from Lopín-1 well (see Figure 9-8). This well is located south of the line ZA-27. The description of the lithologies of Lopín-1 well appears in Lanaja (1987), density and sonic logs are also available (info.igme.es/SIGEOF/). P-wave velocity (Vp) and density logs are characterized by an alternating sequence of high and low velocity/density layers corresponding to Upper/Middle Jurassic and a first sector of Lower Jurassic down to 670 m. This sequence overlies a more homogeneous layer characterized by high velocity and density values corresponding to the Lower Jurassic anhydrites. Velocity and density of Triassic strata depict high values for M1 and M3 and lower values for Keuper and M2 facies. Time to depth conversion was carried out using Skua-Gocad (former Emerson, now Aspentech) based on the average velocities from the seismic processing for each line.

Several geological horizons were interpreted according to different reflectivity patterns and seismic facies (Figure 9-9). From Lopín-1 borehole data and their correlation through the reflection seismic lines, seven main seismic units are differentiated. From top to bottom, these seismic units are: (1) Cenozoic deposits, (2) Jurassic (-Cretaceous) deposits, (3) Hettangian limestones (Imón Fm), (4) Upper Triassic evaporites and lutites (Keuper facies), (5) Middle Triassic rocks (Muschelkalk facies) comprising M3, M2 and M1, (6) Lower Triassic rocks (Buntsandstein facies), and (7) Paleozoic basement rocks. The Paleozoic basement is represented by chaotic reflectors with scarce lateral continuity. The Buntsandstein facies present a medium-to-highly disrupted reflector. The overlying unit represents the Muschelkalk facies, it is divided into 3 sub-units: A high-reflectivity package of two reflectors with relative strong continuity represents the M1 dolostones. The Middle Triassic evaporites (M2) are represented by a poorly-reflective to transparent package, and the M3 dolostones are represented again by two reflectors with relatively high continuity. The overlying Upper Triassic evaporites (Keuper facies) are characterised by a poorly reflective package and above these strata, a characteristic two high-to-medium reflectors represent the Imón Formation dolostones. The marls, gypsums and anhydrites of the Lower Jurassic present as a thick transparent package while the Middle and Upper Jurassic is denoted by a highly reflective package of continuous reflectors. The top most unit is a medium to high reflectivity package with continuous and parallel reflectors that correlates with the Cenozoic deposits.

In the studied reflection seismic lines, the parallel reflectors that correspond to the Buntsandstein facies and the M1 dolostones appear disrupted by faults. However, these Triassic rocks located below the M2 evaporitic level are not well constrained by interpretation of the seismic reflection profile; they represent medium to high disrupted reflectors of low-medium quality (Figure 9-10, Figure 9-11).

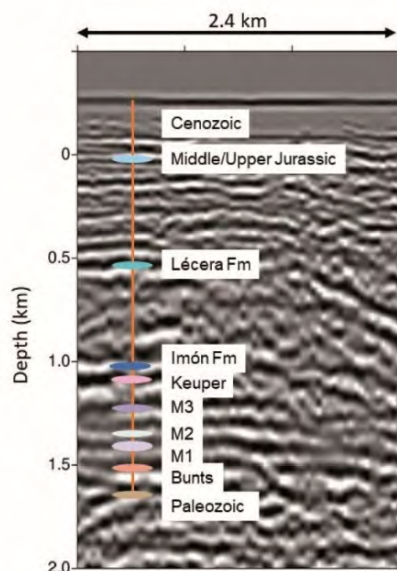


Figure 9-9 Seismic facies from Lopín-1 well (modified from Ayala et al., 2022).

Above the horizon corresponding to M1, the seismic facies that correspond to the Middle Triassic evaporites (M2) show strong lateral variations in thickness. In general, reflectors corresponding to the M3 dolostones, Upper Triassic evaporites (Keuper facies), dolostones of the Imón Fm and Jurassic strata show parallel reflectors with scarce disruptions and slight folding. The Cenozoic rocks of the uppermost unit are represented by parallel reflectors, which are almost horizontal and show

only slight lateral thickness variations. The geometry interpreted from the seismic reflection profile ZA-07 is depicted in Fig. 3-10. This section has a basal succession of Paleozoic basement rocks, Buntsandstein facies and M1 dolostones affected by a series of normal faults forming several horsts and grabens. Above this, the Middle Triassic evaporites (M2) show lateral thickness variations and act as a decoupling level above which the normal faulting is not observed. The M2 is overlain by the M3 and Keuper facies together with the Jurassic-(Cretaceous) rocks which show a series of gentle box folds accommodating deformation occurred below M2 (Figure 9-10); the gentle anticlines coincide with the horsts and synclines with grabens. At the top of the profile, Cenozoic strata overlap a roughly horizontal unconformity eroding the underlying Mesozoic rocks. The SW part of both ZA-7 and ZA-3 seismic profiles are characterized by reverse faults detached on the M2 evaporitic facies affecting the overlying Mesozoic deposits (Figure 9-10, Figure 9-11). These reverse faults are nucleated on the higher points of previous normal fault. They appeared as couples of two reverse faults with opposite vergence and an associated anticline. Along the seismic profile ZA-03 these last structures caused the outcrop of Jurassic rocks. These Jurassic rocks delimit three anticlines at surface oriented NW-SE (Colomer i Guilera et al., 1994) (Figure 9-11).

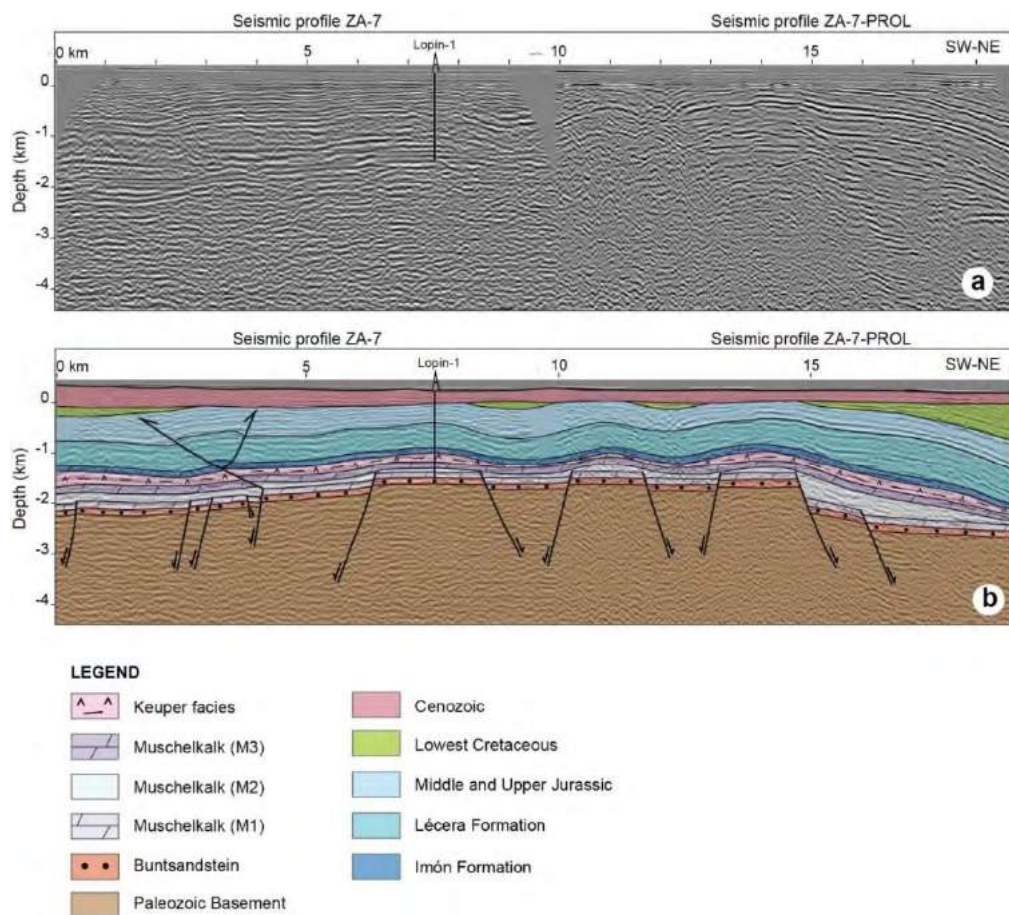


Figure 9-10 a. Depth-converted seismic profiles ZA-7 and ZA-7-PROL (no vertical exaggeration) showing the projection of Lopin-1 borehole. b. Geological and structural interpretation. Modified from Ayala et al. (2022).

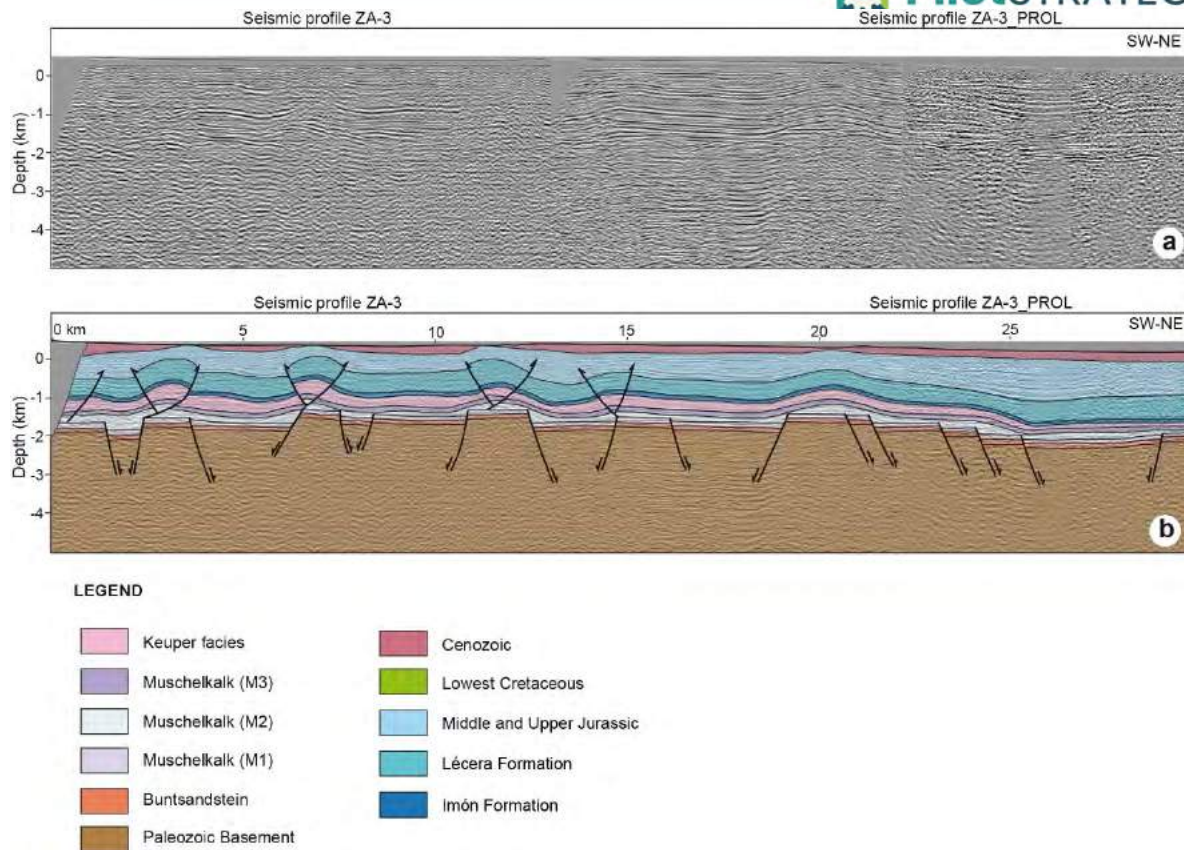


Figure 9-11 a. Depth-converted seismic profiles ZA-3 and ZA-3-PROL (no vertical exaggeration). b. Geological and structural interpretation.

Figure 9-12 shows the orientation of the normal faults interpreted from the analysis of all seismic lines. The fault pattern shows a set of normal faults oriented NW-SE, which delineate a series of three horsts and four grabens with the same orientation. These faults are not continuous through the study area and display segments between approximately 2000 and 5000 meters long (Figure 9-12). However, this discontinuous pattern could be a misinterpretation due to the poor quality of the reflectors below the M2 horizon. The stretching direction compatible with the orientation of the faults of the study area is parallel with the NE-SW Triassic extension deduced in other sectors of the eastern half of Iberia, which is probably related with the westward spreading of the Tethys during the Late Permian-Triassic (Soto et al., 2019).

The throw of the faults varies between few tens of meters and about 200 meters except for the second-to-last fault at the northern end of ZA-07 profile that presents a throw about 500 m. The distance between them is usually around 2 km and does not exceed 2.5 km in a NE-SW trending.

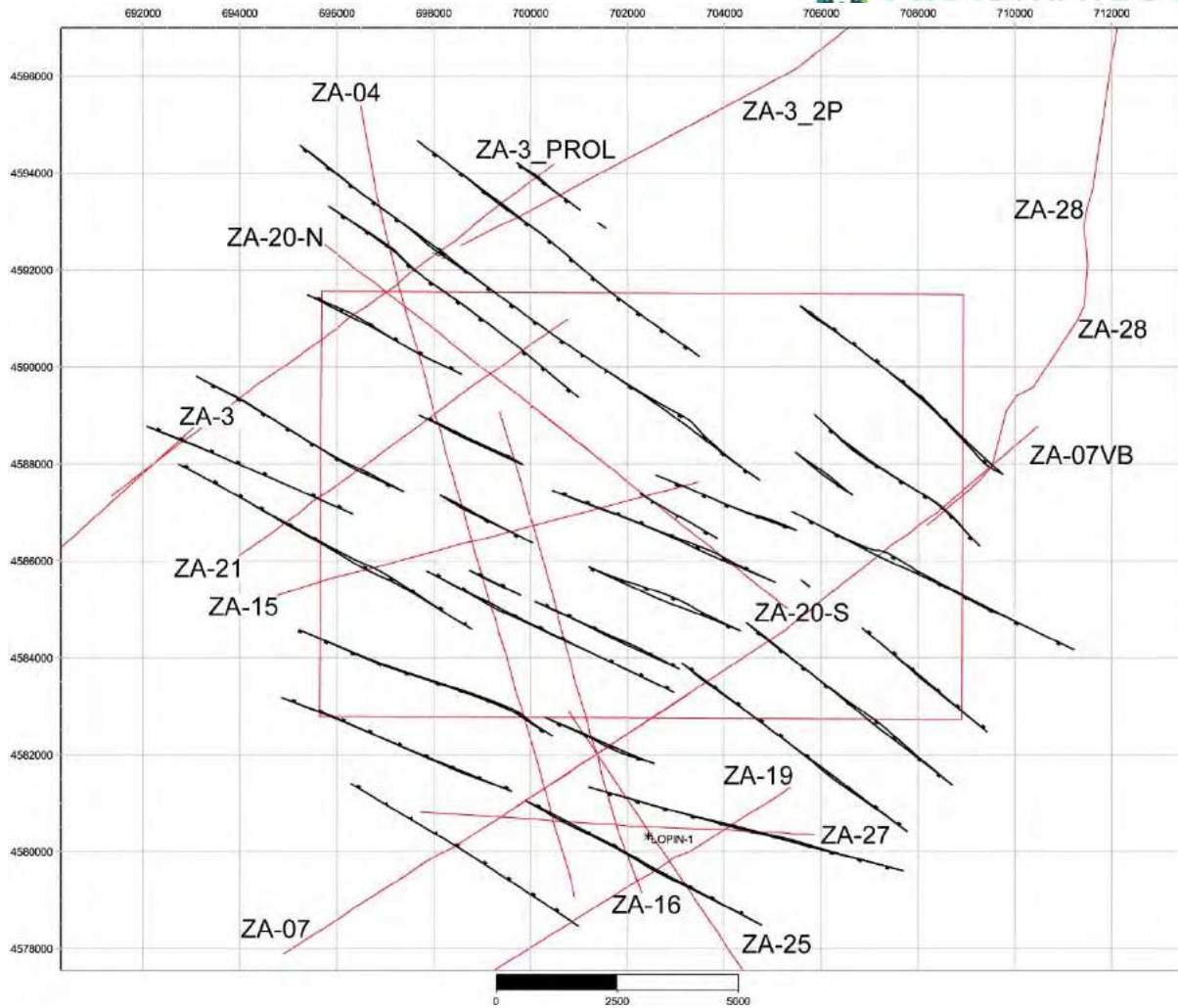


Figure 9-12 Map showing the orientation of the interpreted normal faults (black lines) and location of interpreted seismic lines (red lines). Red box shows the study area.

9.2.2 Tectonic evolution of the study area

The tectonic evolution of the Lopín area is marked by the evolution of northeast Iberia during the Mesozoic extension and the later Alpine compression. The generalized Mesozoic extension in Iberia took place in two rifting stages; a first rifting stage during the Permian and Triassic and a second one during the Late Jurassic and Early Cretaceous. In NE Iberia The first Permo-Triassic rifting has been related with a lithospheric stretching trending NE-SW (López-Gómez et al., 2019), likely related with the westward spreading of the Tethys (Soto et al., 2019). In the study area, this rifting stage has been interpreted to form a series of NW-SE normal faults affecting Paleozoic basement, Buntsandstein and Lower-Middle Muschelkalk facies (M1 and M2) and the development of horst and grabens (Figure 9-13).

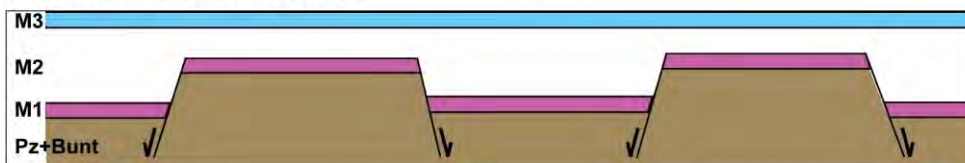
The second rifting stage, Late Jurassic-Early Cretaceous stage, was characterized by a more intense extensional tectonic activity compared with the previous stage, and the formation of major depocenters as the Cameros and Maestrazgo basins (both in the Iberian Chain) which reach more than 7000 meters-thick of syn-rift materials (e.g. Salas et al., 2001). In the study area, located in the so-called Mesozoic Ebro block (e.g. Tugend et al., 2014; Angrand et al., 2020; King et al., 2023), a major depocenter like the Cameros or Maestrazgo basins did not occur. However, the interpretation

of available seismic data has allowed us to infer extensional activity that favoured ideal conditions for salt flow. Thus, we interpret in the study area reactivation of previous normal faults also as normal faults related with this second Late Jurassic-Early Cretaceous rifting stage. This phenomenon would favour the mobilization of M2 Triassic evaporites enlarging thickness variations of this M2 horizon and formation of gentle symmetrical folds in the overlying lithostratigraphic units (M3, Keuper, and Jurassic-Cretaceous) above previous horsts and grabens (Fig. 3-13). At the same time, this evaporitic horizon (i.e. M2 evaporites) would act decoupling deformation since normal faulting is not observed above it. A similar tectonic evolution, where the M2 evaporites inhibited the upward propagation of structures, is described in neighbour sectors in the Ebro basin (Butillé et al., 2012). The role of evaporitic horizons decoupling deformation has also been analysed in analogue modelling (e.g. Soto et al., 2007) (Figure 9-14).

Finally, the last deformation stage occurred during Late Cretaceous and Miocene Alpine compression. This tectonic stage produced a partial tectonic inversion characterized by the new formation of high-angle reverse faults detached on the M2 Muschelkalk facies and nucleated on previous discontinuities provided by older normal faults (Figure 9-13). These types of structures have been interpreted in the western sector of the interest area, close to the Iberian Chain.

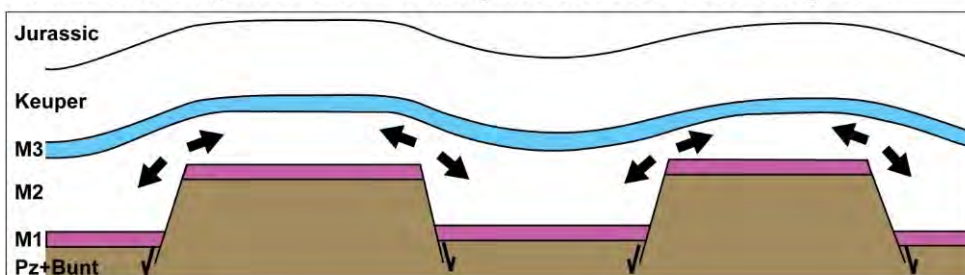
1. Permo-Triassic rifting (1st rifting stage)

Formation of horsts and grabens



2. Jurassic-Cretaceous rifting (2nd rifting stage)

Mobilization of evaporites and formation of gentle folds above horsts and grabens



3. Alpine compression

Partial reactivation of normal faults and folds and formation of new thrusts

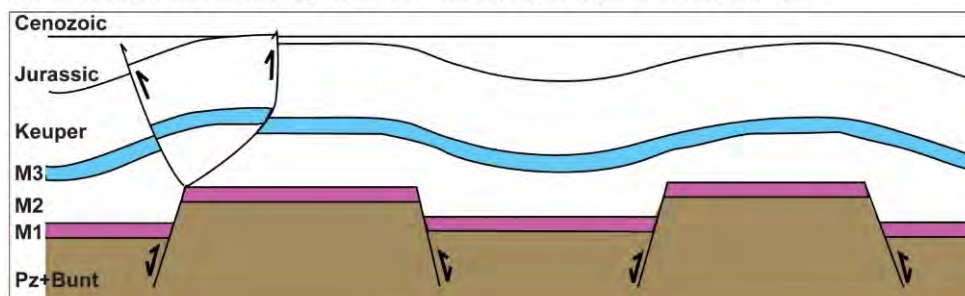


Figure 9-13 Sketch showing the tectonic evolution interpreted for the study area.

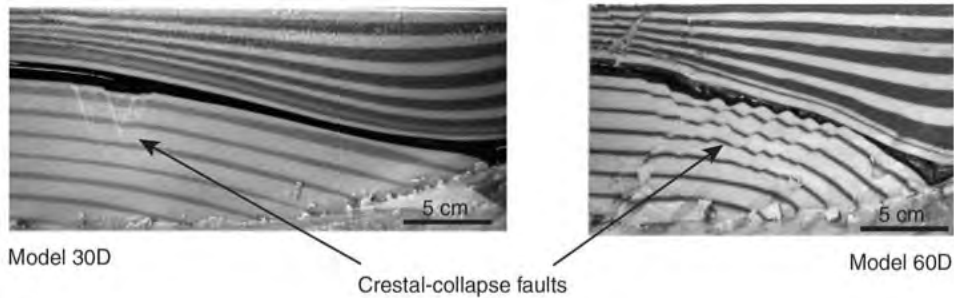


Figure 9-14 Photographs of analogue models showing a ductile horizon (transparent layer) simulating evaporites inhibiting the upward propagation of normal faults and decoupling deformation (taken from Soto et al., 2007).

9.2.3 Partial reactivation in the study area during the Alpine compression

The compressional stage in the study area has been interpreted to cause partial reactivation of previous normal faults and formation of new reverse faults. These reverse faults nucleated at the higher points of previous normal faults affecting the basement, Buntsandstein and Muschelkalk M1 facies (Figure 9-13) and has been interpreted to form due to the partial reactivation of the previous normal faults. The interpreted style of reactivation is similar to the resulted geometries observed in the Tucumán basin (Argentina) (Iaffa et al., 2011) (Figure 9-15). In the Tucumán basin, a normal fault branches at its higher point into two reverse faults of opposite vergence that have an associated anticline it has been interpreted in the study area (see Figure 9-10, Figure 9-11). In both, the study area and the Tucumán basin, the kinematic connection of the reverse faults and the normal fault suggests that the latter has been slightly inverted.

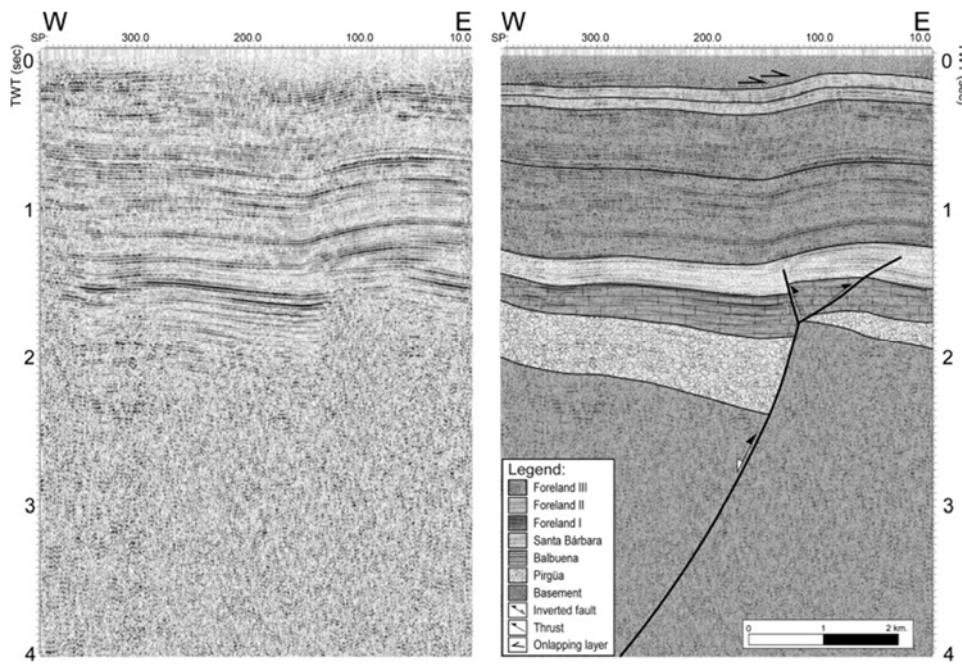


Figure 9-15 Seismic line and its interpretation from the Tucumán basin (Argentina) (taken from Iaffa et al., 2011) showing the partial reactivation of a normal fault and the formation of new reverse faults at its higher point.

This partial reactivation only occurred in the SW parts of seismic lines ZA-7 and ZA-03 (Figure 9-10, Figure 9-11) and therefore, close to the Iberian Chain and its deformation front. It produces reverse faults and associated anticlines oriented NW-SE, parallel to the Iberian deformation front. The structural style of the study area contrasts with that interpreted in the Caspe structure (Figure 9-7) which consists of an anticline structure bounded by ENE-WSW trending thrusts that involved

Variscan basement (Mediato et al., 2017) and probably related to the total reactivation of previous normal faults. This difference could be due to the different orientation of the previous normal faults regarding the roughly N-S Alpine compression direction; structures oriented NW-SE in the studied area versus structures oriented ENE-WSW in the Caspe sector. Structures oriented NW-SE in the study area are oblique to the N-S Alpine compression, whereas the Caspe structures are perpendicular to the N-S Alpine compression (Figure 9-16). This difference in orientation could explain the partial reactivation of previous structures in the study area against the total reactivation of Caspe structure. Previous works highlights that strongly inverted grabens are those whose orientation is perpendicular to the regional compression (e.g. Letouzey et al., 1990).

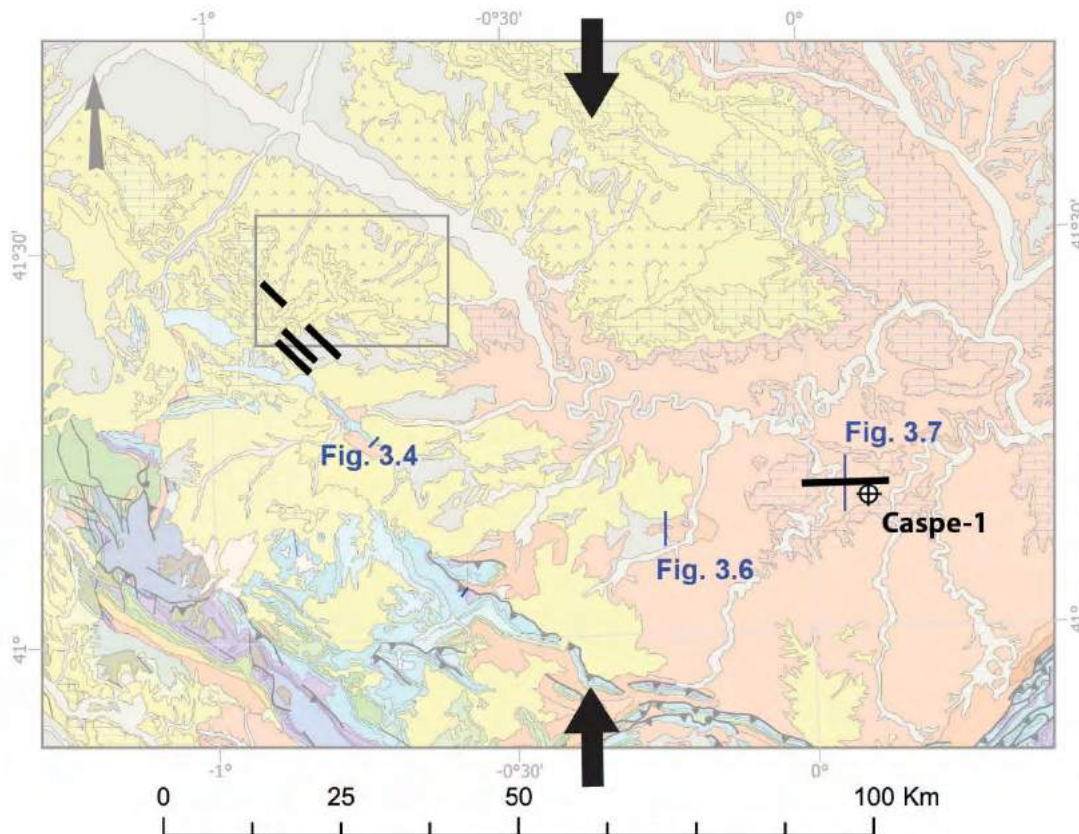


Figure 9-16 Geological map showing the NW-SE orientation of structures in the study area and the ENE-WSW orientation of structures in Caspe (in black lines) with respect to the N-S Alpine compression orientation (in black arrows).

9.3 Geophysical Models Implementation

9.3.1 Methodology used in implementation of the Geophysical models

9.3.1.1 Passive Seismic Method

Passive seismic method is commonly known as the record and analysis of natural or induced seismicity with borehole or surface sensors (seismic monitoring) but also includes the acquisition of ambient vibrations or seismic noise, without using any active energy sources. The analysis of seismic noise is a valuable tool for subsurface characterization. Noise is related to ambient vibrations of the ground caused by different sources: tides, wind, anthropogenic noise sources such as cars, trains, industry, etc. (Bonney-Claudet, et al., 2006). As part of the geophysical methodology, we have included the acquisition and processing of ambient noise vibrations (Figure 9-17). The objective of

this survey is to provide additional subsurface information in a cost-effective way adding constraints for the seismic interpretation of the legacy active seismic sections and for the gravimetric modelling.

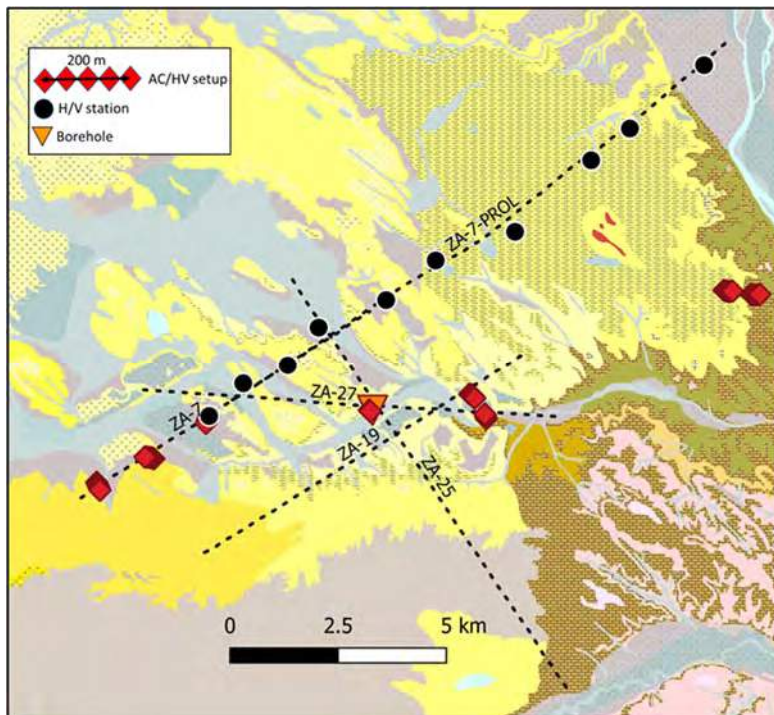


Figure 9-17 Geological map of the study area with the location of the Lopín-BH (orange triangle), seismic stations of the first survey in summer 2021 (red diamonds) and seismic stations for the second survey in December 2021 (black dots).

The passive seismic study included the application of two different methods: H/V microtremor and autocorrelation techniques.

The **H/V method** (Horizontal-to-Vertical spectral ratio of ambient noise method) has increasingly been used in several fields such as seismology, geotechnics or geology. This method is based on the recording of ambient noise in a 3-component sensor and computation of the ratio between the Fourier amplitude spectra of the horizontal and vertical components of seismic noise. The resulting spectral ratio is called H/V curve whose amplitude peaks can be related with the presence of seismic impedance contrasts. The physical basis of this method is controversial (Bonney-Claudet, et al., 2006). Some authors established a direct link between the shape of H/V curves and the S-wave resonance in the subsurface (Nakamura, 2000) whereas other authors suggested that the shape of the H/V curves is controlled by the polarization of surface waves (e.g. Konno & Ohmachi, 1998). The standard way of obtaining the H/V curves is to select stationary windows from a long record of ambient noise in a 3C sensor. Then, the Fourier amplitude spectra of the three components are computed and smoothed. Average of horizontal components is obtained and then, the horizontal-to-vertical spectral ratio is calculated for each window. Finally, the average H/V curve (and its standard deviation) is computed from the H/V curves calculated for all windows (Figure 9-18).

Since the 1990s, several authors have introduced the H/V method as suitable for exploration studies (e.g., Ibs-von Seht and Wohlenberg, 1999; Benjumea et al., 2011). These studies benefit from the relationship between the frequency corresponding to amplitude peaks of the H/V curve ($f_{H/V}$) and the depth (h) of a contact with a significant impedance contrast (Gabàs et al., 2016). A relationship

between these two quantities ($f_{H/V}$ and h) includes the average shear-wave velocity of the sediments (V_s):

$$f_{H/V} = \frac{\overline{V_s}}{4h} \quad (1)$$

Since shear-wave velocity information is not always available, another way of obtaining h is based on using an empirical relationship between h and $f_{H/V}$ (Ibs-von Seht and Wohlenberg 1999):

$$h = a f_{H/V}^b \quad (2)$$

where a and b are empirical parameters. This relationship is supported by the observations that the shear-wave velocity of unconsolidated overburden commonly exhibits a velocity gradient with depth. In this study area, we used the velocity gradient obtained from sonic logging at Lopín-1 borehole.

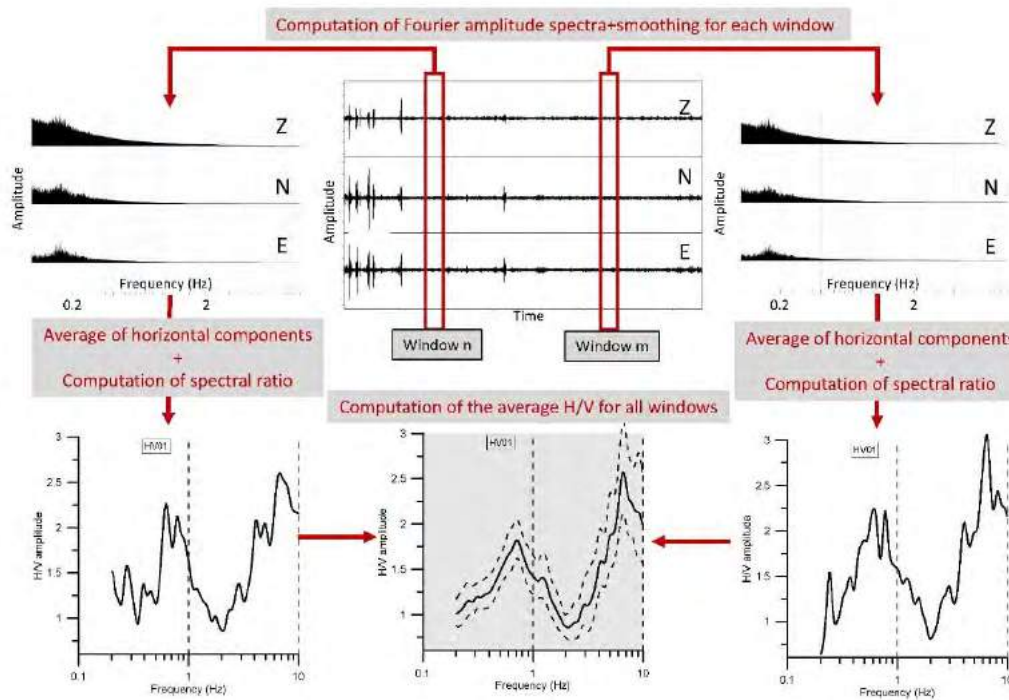


Figure 9-18. Schematic of the procedure for obtaining H/V curves from ambient noise records.

The aim of the **autocorrelation** technique is to retrieve the reflectivity response of the subsurface or empirical Green function (Romero and Schimmel, 2018). The workflow included the extraction of time windows and the autocorrelation of each of them. The last step is to stack all the autocorrelations to obtain the reflectivity response (Figure 9-19).

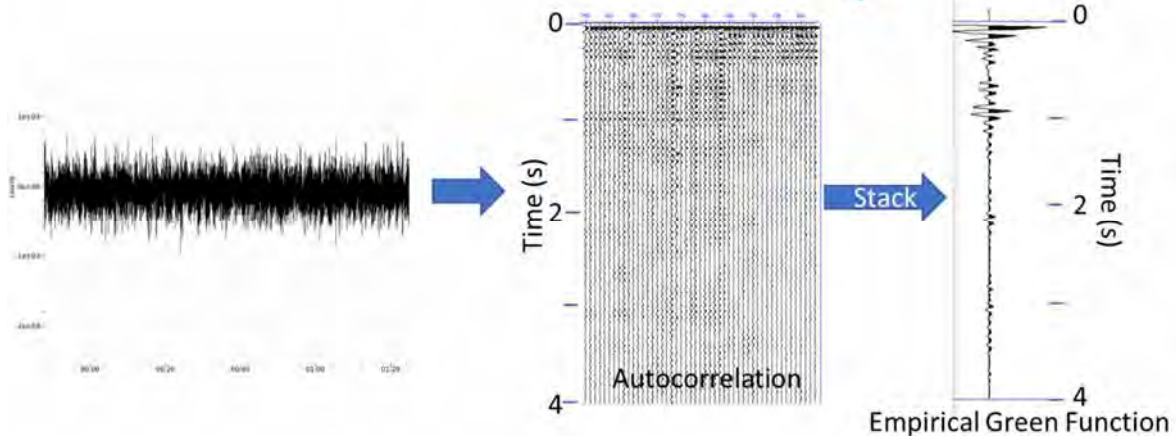


Figure 9-19. Schematic of the procedure for obtaining reflectivity response of the subsurface (Empirical Green function) from ambient noise records.

9.3.1.1.1 Field surveys

A first passive seismic survey was carried out during two weeks of the 2021 summer using seismic equipment owned by Geociencias Barcelona (GEO3BCN - CSIC). Ten seismic stations consisted of 120 s 3-component Trillium Compact sensors and Spyder digitizers. This first survey was focused on acquired ambient noise during long records to study the suitability of the autocorrelation method to obtain reflectivity response in this area. A group of 3-4 stations spaced 50 m were installed at different locations for 2 days record length and a sampling rate of 0.004 s (Figure 9-17). The locations (red diamonds in Figure 9-17) were selected close to the legacy seismic profiles to allow comparison among active and passive seismic datasets. An additional group of 5 stations were placed in an eastern sector lacking previous seismic information. Two stations were also located by Lopín-1 borehole for ground-truthing. The sensors, digitizers and batteries were buried in a pit (Figure 9-20). In total 32 stations were installed. This passive dataset is also valid to apply the H/V technique.

A second survey focused only on H/V technique was carried out along the ZA27 profile at 12 locations spaced between 1 and 2.3 km (black circles in Figure 9-17). Data was acquired with a 5 s 3-component sensor (Tellus by Lunitek) and Centaur Nanometric digitizer (courtesy of Instituto Geográfico Nacional). For this dataset, record length was 2 hours suitable for H/V method. Quality control was done in the field to check that the record length was enough to retrieve H/V curves.

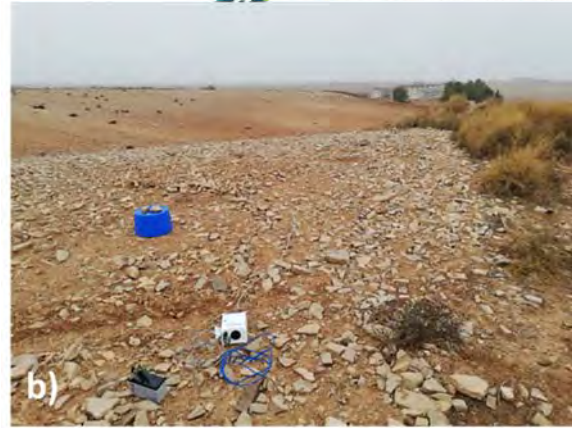


Figure 9-20. a) Installation of seismic station during the first survey with two days of recording. Station is composed by 120 s Trillium Compact sensor (green casing) and Spyder digitizer. b) Installation of seismic station during the second survey focused on H/V method. Instrumentation consisted of 5 s Lennartz sensor (covered by blue box) and Polaris digitizer (white casing).

9.3.1.1.2 Processing and analysis

H/V method

The H/V curves were calculated using Geopsy software (<http://www.geopsy.org>; Wathelet et al., 2020). The complete record was cut in time windows length of 250 s. H/V curves were obtained for each window after Fourier transform of each component, smoothing and horizontal components averaging. The final H/V curves are the average of the horizontal-to-vertical spectral ratio of each window.

In order to transform the frequencies corresponding to H/V amplitude peaks into depth and constrain the interpretation of these main peaks, we obtained an empirical relationship (Eq. 2) using the velocity information from the geophysical well logs from Lopín-1 borehole. Beforehand, we had to correct erroneous values of slowness within the first 400 m due to an incorrect scale being used during the digitization process. We then calculated the compressional-wave velocity (V_p) log in m/s, obtaining 10 m interval velocity to downscale the geophysical logging to favor the comparison with H/V curves. Since the $f_{H/V}$ -h empirical relationship is based on V_s , we have obtained an interval V_s profile from interval V_p following different V_p to V_s relationships. In particular, we compared results from two V_s estimation models based only on V_p (Brocher, 2005 and Greenberg and Castagna, 1992). Brocher (2005) relationship was retrieved from V_p and V_s measurements compiled from boreholes logs, VSP, laboratory measurements and seismic refraction tomography studies from California. This relation is:

$$V_s = 0.7858 - 1.2344 V_p + 0.7949 V_p^2 - 0.1238 V_p^3 + 0.0064 V_p^4$$

On the other hand, Greenberg and Castagna (1992) proposed the following relationship to obtain V_p from V_s from coupling empirical relationships between shear- and compressional wave velocities with Gassmann's equations:

$$V_s = -0.85588 + 0.80416 V_p \quad (4)$$

For both equations (3) and (4) V_p and V_s are in km/s.

Since differences between these values fell within a range of 72 and 252 m/s, we decided to use Brocher (2005) as this is the most recent reference. The V_p to V_s transformation is one source of

uncertainty that should be considered coming from different factors such as the intrinsic limitation of the Brocher relationship obtained from a limited set of data information. Another issue when using well log velocity information is the lack of data from the shallow part of the well. Lopín-1 borehole has velocity information from 53 m depth down to the bottom of the well. We have assumed a V_p range for the shallow part (0 - 53 m depth) of 2200 to 2550 m/s based on velocity information for Tertiary sediments in the Ebro basin. We calculated the average V_s -depth function using this V_p range for the shallower sector and two different frequency-depth relationship using Eq. 2 for an average V_p of 2200 m/s. The resulting a and b parameters of Eq. 2 are 394.2 and 1.5, whereas for an average V_p of 2550 m/s the values for a and b are 474.2 and 1.4. The plots for both $f_{H/V}$ - h relationships are included in Figure 9-21. In this figure, another $f_{H/V}$ - h relationship obtained for the Neogene basins in Northeast of the Iberian Peninsula (Gabàs et al., 2016) has been also included to highlight the importance of estimating local $f_{H/V}$ - h relationships.

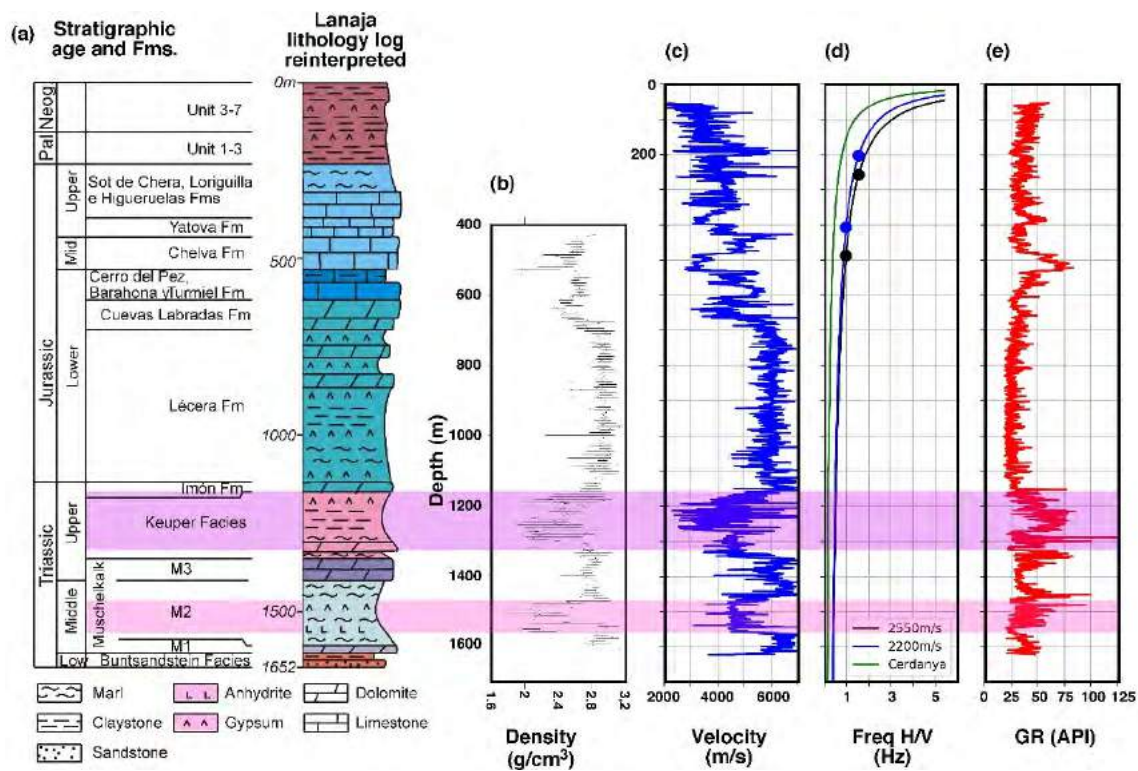


Figure 9-21. (a) Stratigraphic column of Lopín-1 borehole. (b) Average density and standard deviation values calculated at 2.75 m intervals. (c) P-wave Velocity (V_p). (d) Relationships depth versus H/V frequency. Cerdanya relationship (green line) was based on geophysical measurements in the area (see Gabàs et al., 2016). The blue and black lines are two local $f_{H/V}$ - h relationships obtained for this study from Lopín V_p log and two average V_p values for the section from 0 to 53 m depth (2200 m/s-blue line and 2550 m/s- black line). The V_s estimation model used was Brocher (2005). Dots display depths obtained from each relationship and the frequencies of two peaks observed at the H/V curve at Lopín-1. (e) Gamma-Ray (GR) log.

Autocorrelation

The calculation of autocorrelation has been done for 300 s time windows after filtering the signal between 10 to 50 Hz. The maximum lag was 10 s. The algorithm for autocorrelation was introduced by Schimmel (1999). We have performed the final step, i.e. stacking of the autocorrelations, using the time-frequency domain phase weighted stack (tf-PWS) (Schimmel and Gallart, 2007).

Data quality of this first survey dataset can be considered as good/fair (western sector) to poor (eastern sector). Figure 9-22 a and c) shows a 4 minutes record and corresponding spectrogram as example of data quality of the eastern sector. The spectrogram is characterized by the presence of strong monochromatic noise at several frequencies (e.g. 28 Hz) as depicted by horizontal lines of large amplitude. This coherent noise significantly affects the applicability of the autocorrelation method since we focus on the 10-50 Hz range. A frequency debursting filter based on L1 IRLS approach (Iteratively Reduced Least-Squares) in the uncorrelated domain has been carried out to reduce the amplitude of this coherent noise following the workflow proposed by Girard and Shragge (2020). Figure 9-22d shows the spectrogram obtained after applying the debursting filter where coherent noise amplitude is significantly reduced.

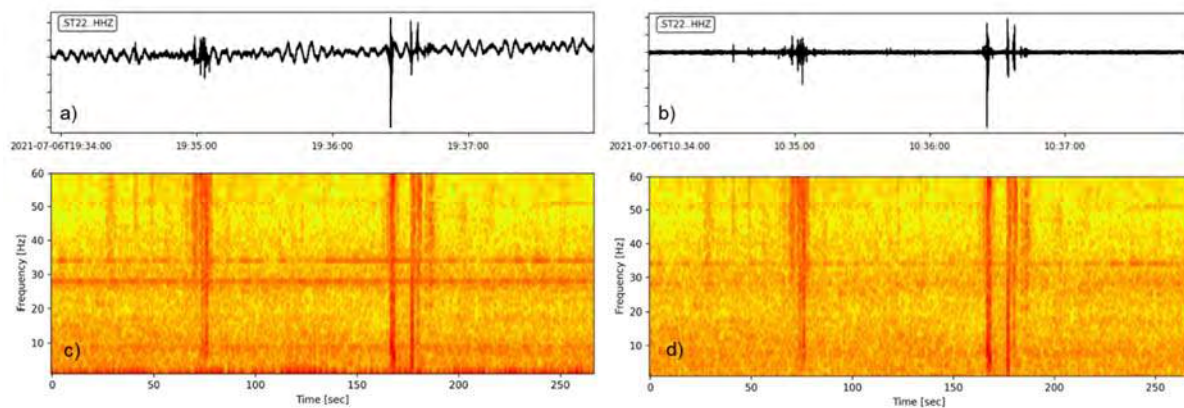


Figure 9-22. a) Example of a 4 minutes time window from a recording at a western station and spectrogram c). b) Same time window as a) after filtering and corresponding spectrogram d).

9.3.1.2 2D Gravity modelling

The aim of the gravity method is to determine the density distribution of the subsurface structures by measuring variations in the gravitational field resulting from lateral variations in rock density. This goal is attained by gravity modelling, whose objective is to help to understand the subsurface structure of the geological bodies by means of their geometry and density.

The modelling consists of building up and visualizing the lithostratigraphic units in order to determine its internal structure, its extension and geometry (especially the ones that does not crop out) and its petrophysical properties.

The geological model must be consistent with the available geophysical, geological and petrophysical data which, in turn, are used as a constraint in the modelling process in order to reduce the uncertainties associated to the interpretation of each method alone.

The level of detail in the model obtained, namely geometry and density distribution, depends on several factors. These include the spatial distribution of the measured data, the size of the study area, and the petrophysical, geological, and geophysical information available to be used as *a priori* knowledge to limit the number of equivalent solutions that arise in gravimetric modelling (as well as any geophysical method). It is crucial to understand that the level of detail should not be confused with uncertainty, which is a parameter associated with the results of the modelling that characterizes the range of values that could reasonably be attributed to the calculations using the measured data. The detail refers to the dimensionality of the structures that can be resolved, generally ranging from meters to kilometers.

Gravity modeling is particularly valuable when seismic data has low resolution or it is scarce. Starting with an initial geological model (preferably balanced cross sections, but not essential), gravity modeling helps to refine the geometry and densities of the geological structures at depth. By combining gravity data with other geophysical data (e.g., passive seismic), wellbore data, and petrophysical data, the number of potential solutions is reduced.

The density contrast between the lithologies of the structure makes the gravimetric method suitable to improve the characterization of the geometry through 2D forward gravity modelling.

The purpose of using this technique in this project is to supplement the lack of reliable seismic data at depth, so it can be a useful tool to help delineate the upper part of the basement and the distribution of the fault blocks.

Previous data in Lopín area

In order to constraint the gravity models, we have used the available geophysical information. A feedback has been established between the gravity, seismic and H/V interpretation in order to obtain a final model consistent with these observables and geologically sound:

Seismic lines: The initial cross sections are based on the interpretation of the reprocessed reflection seismic lines and this interpretation has been improved through the gravity modelling.

Gravity data. During 2021 a new gravity survey was held. The resulting report (D2.2 Gravimetric survey, ID number 101022664, <https://pilotstrategy.eu/about-the-project/work-packages/geo-characterisation>) provides the Bouguer anomaly and the residual anomaly maps. Since our target is to model the structures of the upper crust, we will use the residual Bouguer anomaly.

Petrophysical data. For the petrophysical data, we have combined the information from boreholes, petrophysical data from the Linking Zone (Izquierdo-LLaval et al., 2015) and new petrophysical data from the analysis of rock samples of the study area. The densities for each layer have been assigned by a combination of different sources: gamma-gamma (formation density) logs obtained from the Lopín-1 borehole (Lanaja, 1987), which provided over 7,700 readings from depths ranging from 425 to 1610 meters. Additionally, densities from 17 sites in the study area (consisting primarily of Cenozoic, Triassic, and Permian rocks) measured at the Tres Cantos Laboratories and information from previous studies in areas with similar lithologies (e. g. Pueyo et al., 2016, Izquierdo-Llavall et al., 2019, and references therein). A histogram of the density data of the outcrop hand samples and the ones from the Iberia Range is depicted in Figure 9-23. Furthermore, since there are no Cretaceous outcrops or data from the Lopín-1 borehole, for the Purbeck facies we have used the density data from the same lithologies found in the Hontomín 1, 2 and 3 boreholes (Ayala et al., 2011).

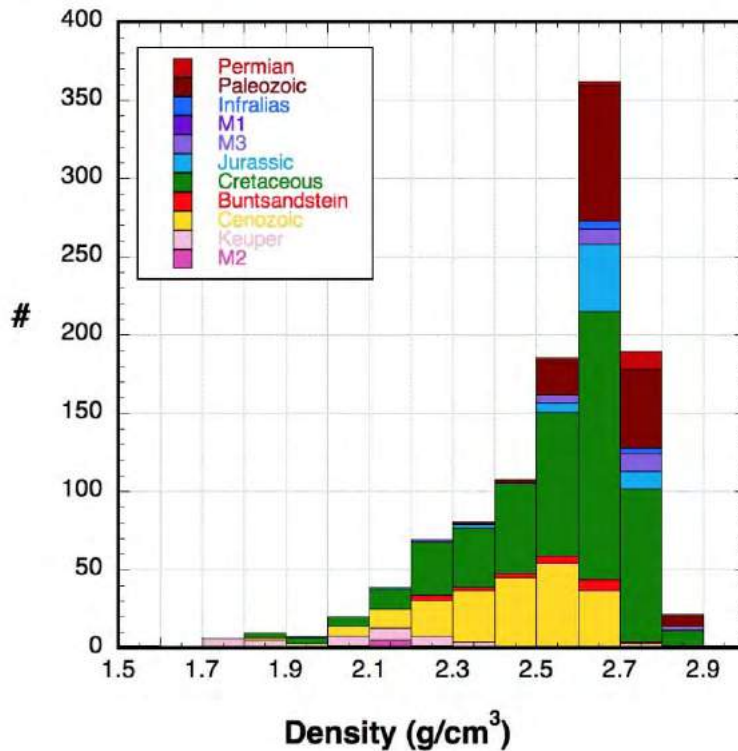


Figure 9-23 Histogram of density data from outcrop hand samples of the Iberian Range database (including the data acquired in this project). Figure from Ayala et al., 2022.

9.3.1.2.1 Methodology and 2D modelling process

The software used for the 2D forward gravity modelling is Oasis Montaj GM-SYS from Seequent (former Geosoft). The input data is the residual Bouguer anomaly, the information from Lopín-1 borehole that has been projected onto one of the cross sections and the results from H/V. The H/V information has been imported in GM-SYS as pseudo wells with the depth of the Tertiary and Purbeck, and this information has helped to constraint these layers of the model.

In GM-SYS, the gravimetric response of the model is calculated using the algorithms described in Talwani et al. (1959), Talwani and Heirtzler (1964), and Won and Bevis (1987). We have carried out the calculations using forward modelling.

We have assumed that the modelled structures, horsts and grabens, have a lateral continuity that extends far enough to consider that the hypothesis for 2D modelling are valid along the reinterpreted seismic sections.

We have modelled 10 geological cross sections derived from the reinterpretation of vintage seismic sections, converted to depth as explained in section 9.2, and 3 more cross-sections created specifically to constrain the SE end of the model, see the map with their location on *Figure 9-24*.

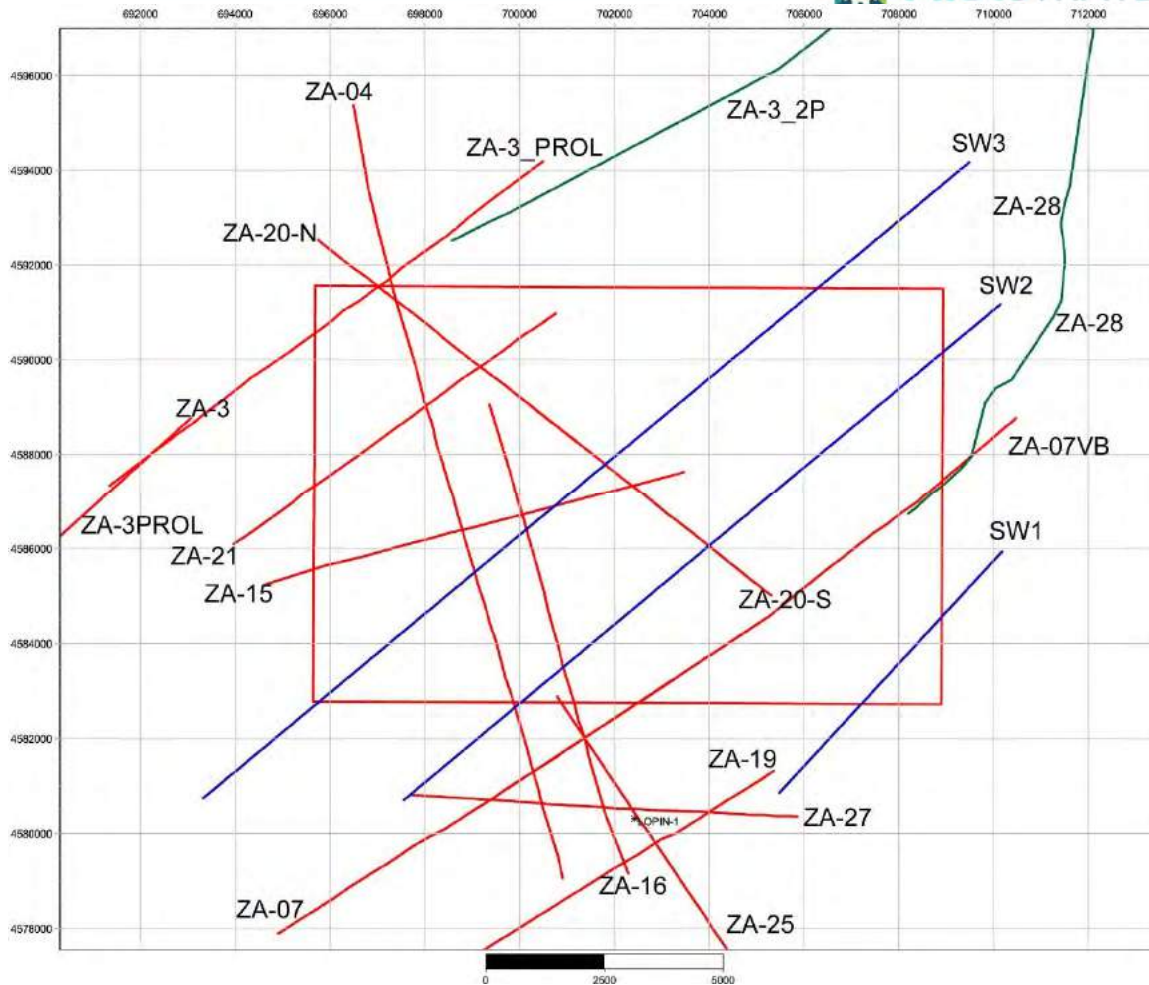


Figure 9-24 Map of the study area (in red rectangle) showing the cross sections derived from the reinterpretation of vintage seismic sections (in red) and cross-sections created specifically to constrain the SE end of the model (in blue). In green vintage seismic sections, not interpreted because they are located outside the area of interest.

The geometry of each model is created by digitizing a georeferenced image. The image has been georeferenced in Oasis Montaj prior importing in GM-SYS.

The depth of the profiles is set at 5 km BSL (below sea level).

After digitizing the cross-section, we assign the petrophysical properties and start improving the model through a feedback process by means of discussing the origin of the misfits with the geologists and modifying either the geology or the density where needed. The feedback ends when we obtain a model whose calculated anomaly fits the observations, is consistent with the other geophysical data and keeps its geological meaning.

After evaluation of the available petrophysical data, the densities chosen for the model are:

Formation	Density (g/cm ³)
Cenozoic	2.45
Cretaceous (Purbeck facies)	2.44
Jurassic and Infra-Liassic (Imón Fm)	2.62
Anhydritic Jurassic	3.0
Keuper	2.25
M3 (dolomites)	2.80

M2 (evaporites)	2.25
M1 (anhydrite and dolomites)	2.90
Buntsandstein	2.58
Paleozoic basement rocks	2.68

To avoid edge effects, we have extended all models twice its size at both ends of the profile.

The uncertainties of the final model are estimated by means of sensitivity tests, varying the horizons within the bounds set by the seismic data or densities within the range obtained in the petrophysical data while ensuring that the calculated anomaly remains adjusted (e.g. Ayala et al., 2003). These uncertainties vary from profile to profile but in general are of the order of 20 m or less.

We exported each of the modelled horizons as ASCII files in UTM coordinates (x, y and z).

The workflow used in this work is shown on Figure 9-44.

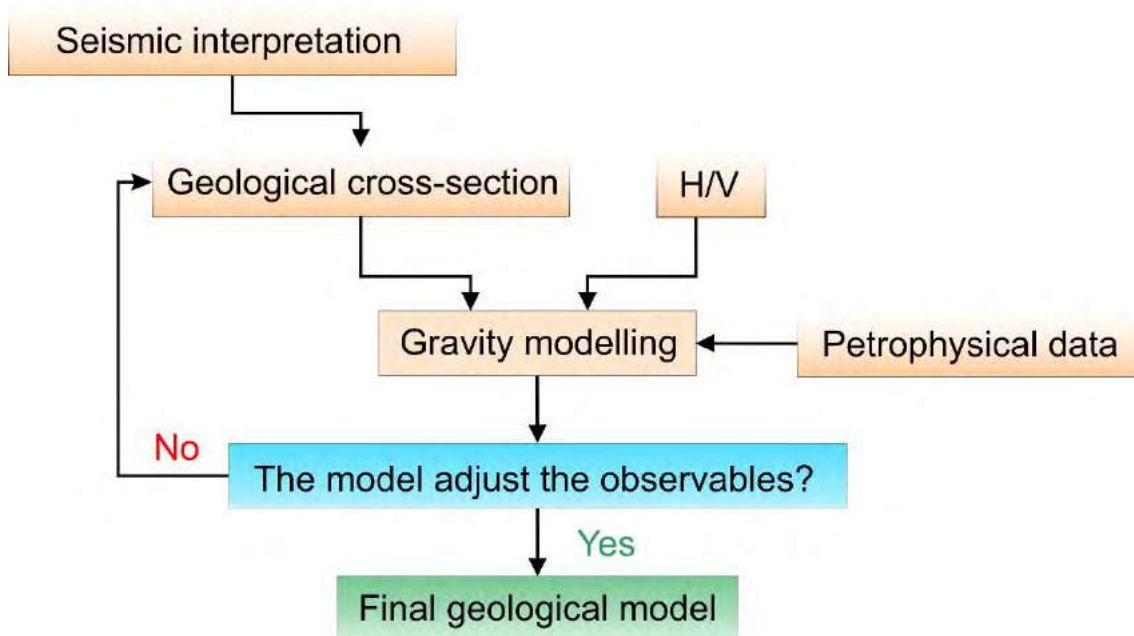


Figure 9-25 Workflow of the methodology applied in this work for the 2D gravity modelling (from Ayala et al., 2022).

9.3.2 Interpretation

In this chapter, we describe the results and conclusions of the passive seismic surveys and 2D gravimetric modelling, after the processes described in the previous sections, utilized the seismic interpretation as constrain. The final objective is to get a structural model from the gravimetric modelling of the profiles constrained with the passive seismic results.

9.3.2.1 Results of the passive seismic survey

H/V method

Figure 9-26 shows the results obtained at two stations located near the Lopín-1 borehole. The H/V curves along the profile are displayed in Figure 9-27. All the curves are characterized by peaks with low H/V amplitude values for frequencies below 5 Hz. At higher frequencies, high amplitude peaks are observed for stations HV34 at 7.5 Hz, HV35 at 9.4 Hz and HV39 with a maximum at 5.1 Hz. The three stations were located over Holocene sediments and these maxima are probably related to the

Quaternary/Neogene contact. Maximum thickness of the quaternary deposits is found at HV39 station, located on the Ebro River terraces. The high amplitude of these peaks is a result of low velocity sediments at surface. Regarding the low amplitude peaks at frequencies lower than 5 Hz, the H/V curves obtained close to the well (Figure 9-26) were used to select peaks in the rest of the profile. Two peaks that are consistent in both curves were interpreted using well information. As explained before, two different average V_p velocities (2200 and 2550 m/s) were used for the shallow part of the well to obtain the frequency-depth relationship from Lopín-1 borehole and Brocher (2005) V_s estimation model. For simplicity, we will refer to these two relationships as 2200 $f_{H/V}$ -h (blue line in Figure 9-21) and 2550 $f_{H/V}$ -h (black line in Figure 9-21). The lower frequency maxima for both stations (Figure 9-26) lies at 0.98 Hz. Using the two obtained $f_{H/V}$ -depth relationships, the corresponding depth would be 406 m using 2200 $f_{H/V}$ -h and 488 m using 2500 $f_{H/V}$ -h. These depths can be considered as bounds for seismic impedance contrast interpreted as a lithological change. The Lopín velocity log (Figure 9-21) shows a sharp increment around 420 m depth described as the contact between Upper and Mid Jurassic strata. Hence, the low frequency maxima could reasonably be interpreted as a significant velocity contrast within the Jurassic deposits. The other maximum identified in Figure 9-26 corresponds to a frequency of 1.55 Hz. This can be related to a depth of 203 m or 258 m using 2200 $f_{H/V}$ -h or 2550 $f_{H/V}$ -h relationships, respectively. The contact that produces this maximum can be interpreted as the transition from Cenozoic to Mesozoic strata. The interpretation of these two peaks at Lopín-1 borehole was used to identify geologically meaningful H/V peaks along the profile and calculate a depth range for these two seismic impedance contrasts. The separation of these two peaks varies along the profile and, in particular, at stations HV36 and HV37 only one wide peak is observed with a maximum around 1.2 Hz. This can be related with an approximation in depth of both contacts at this zone that cannot be resolved with the H/V method as discussed below.

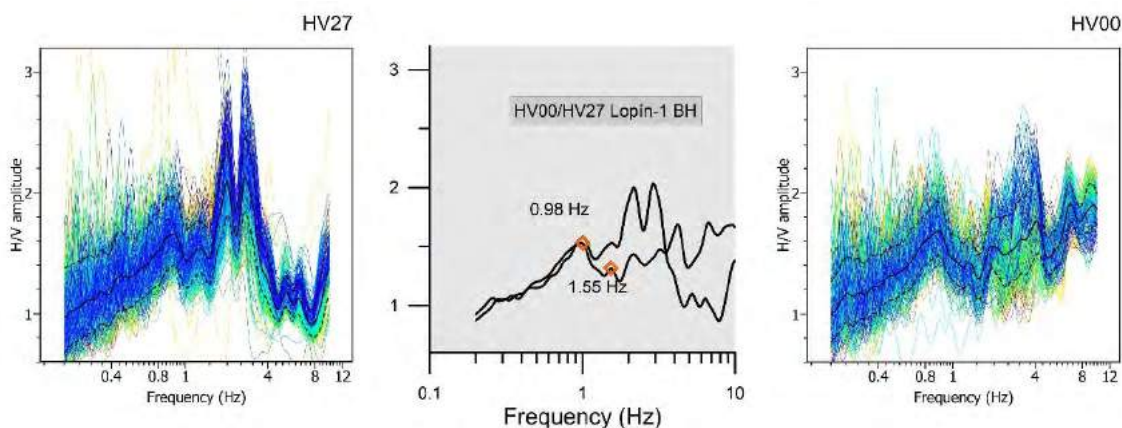


Figure 9-26. H/V curves (color lines) obtained for all the time windows at stations 27 and 00 located at the vicinity of the Lopín borehole. Black and dashed lines represent the H/V average curve and standard deviation. The H/V average curves for both stations (HV00 and HV27) have been jointly plot in the center figure to compare consistent maxima at the two stations.

The H/V method provides information on the presence of significant seismic impedance contrasts in the top 500 - 600 m depth. This method requires geological and velocity data that in this study has been provided by the Lopín-1 borehole. A detailed analysis of relationship between H/V frequency, velocity and depth has been included to obtain a local $f_{H/V}$ -depth relationship suitable for this area. To our knowledge, this is the first time sonic logging has been used to estimate depths of impedance contrasts identified using H/V. The application of a local frequency-depth relationship is critical to

obtaining reliable depths using the H/V method. However, depth uncertainty is also intrinsic to this method; in this study uncertainty is generated by: (1) estimation of shear-wave velocity from compressional-wave velocity (2) lack of velocity information of the shallow part at Lopín-1 borehole which is common in exploration boreholes. It should also be noted that, in this geological context, H/V peak amplitudes are low due to the relatively high velocity of Cenozoic sediments, and that plausible interpretation of the corresponding geological contacts requires appropriate geological borehole information. Two main peaks have been analysed. Based on data from the Lopín-1 borehole, the highest frequency peak has been interpreted to be the base of the Cenozoic strata. The estimated depth for the lower frequency peak correlates with an intra-Jurassic velocity change in Lopín-1 borehole. Nonetheless, at the northern end of the profile, this peak could also potentially be associated with the base of the Cretaceous strata.

The limits and uncertainty of the estimated depth for these two geophysical features (shown as two segments at each H/V location in Figure 9-36) were obtained from the two frequency-depth empirical relationships ($2200 f_{H/V-h}$ and $2550 f_{H/V-h}$). The depth ranges at each H/V station for the base of the Cenozoic along the profile and for the deeper seismic impedance contrast has been used as constraint for gravity modelling, reducing uncertainties in the shallow section. These results have helped to constrain the gravimetric model (Figure 9-36).

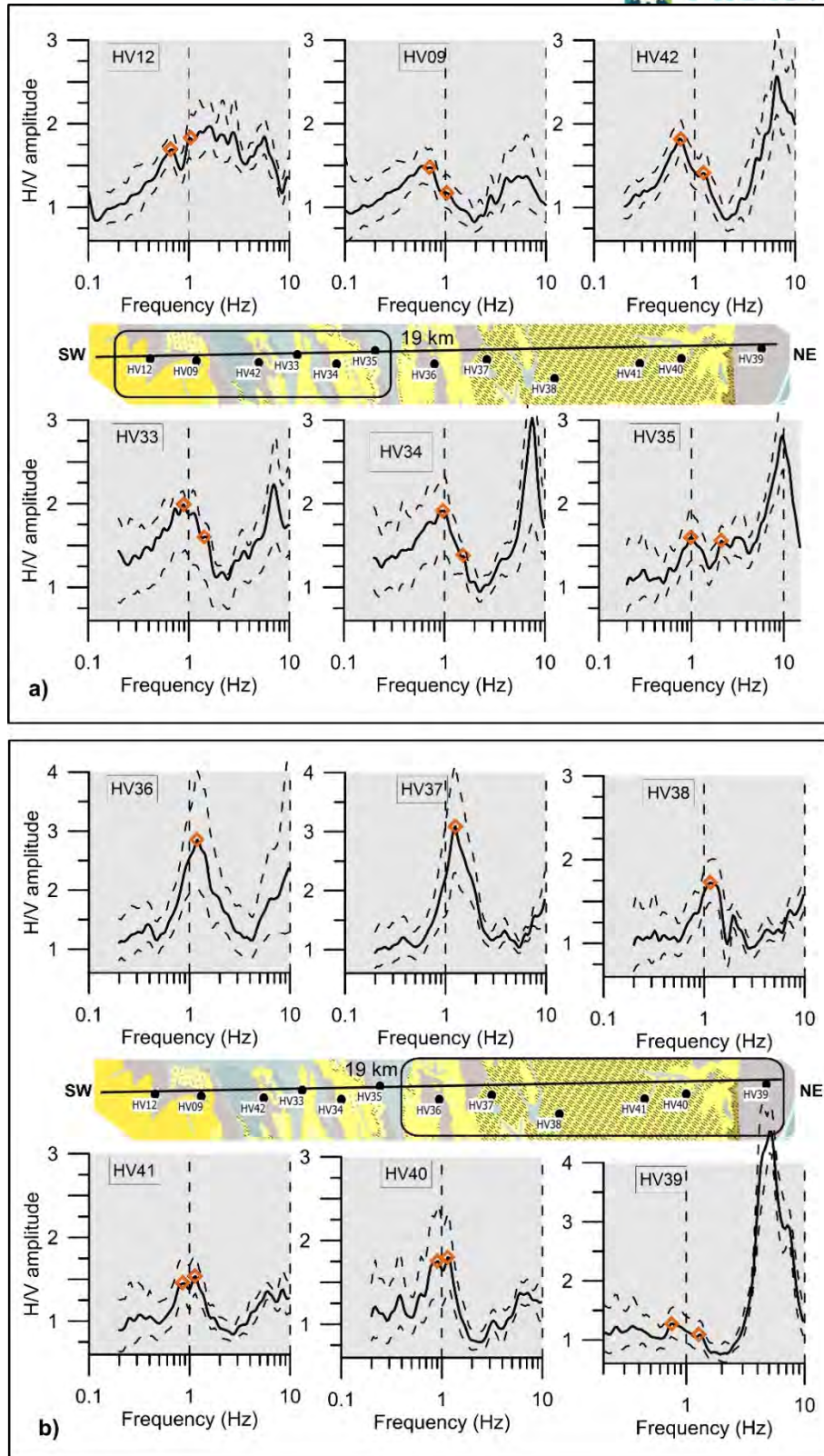


Figure 9-27. H/V curves (average: continuous lines and standard deviation: dashed lines) corresponding to the six stations at the SW sector of the profile (a) and at the NE sector (b) H/V amplitude scale has been adjusted to improve clarity at each curve. Orange diamonds mark the peaks considered a result of geological features based on interpretation of the H/V curves acquired at the Lopín-1 borehole (Figure 9-26).

Autocorrelation

Figure 9-28b and d displays the autocorrelation results for a group of five stations located close to the SW sector of ZA-07 profile and for another group of four stations set up in the vicinity of ZA-19 profile. For comparison, we have included the sectors of active seismic reflection sections located close to the seismic stations (Figure 9-28c and e). There is a correspondence between the amplitude maxima of the autocorrelation and some of the reflections observed in the active seismic datasets. In this case, autocorrelation helps to confirm the interpretation of bedrock top, which is one of the limitations of the legacy seismic sections.

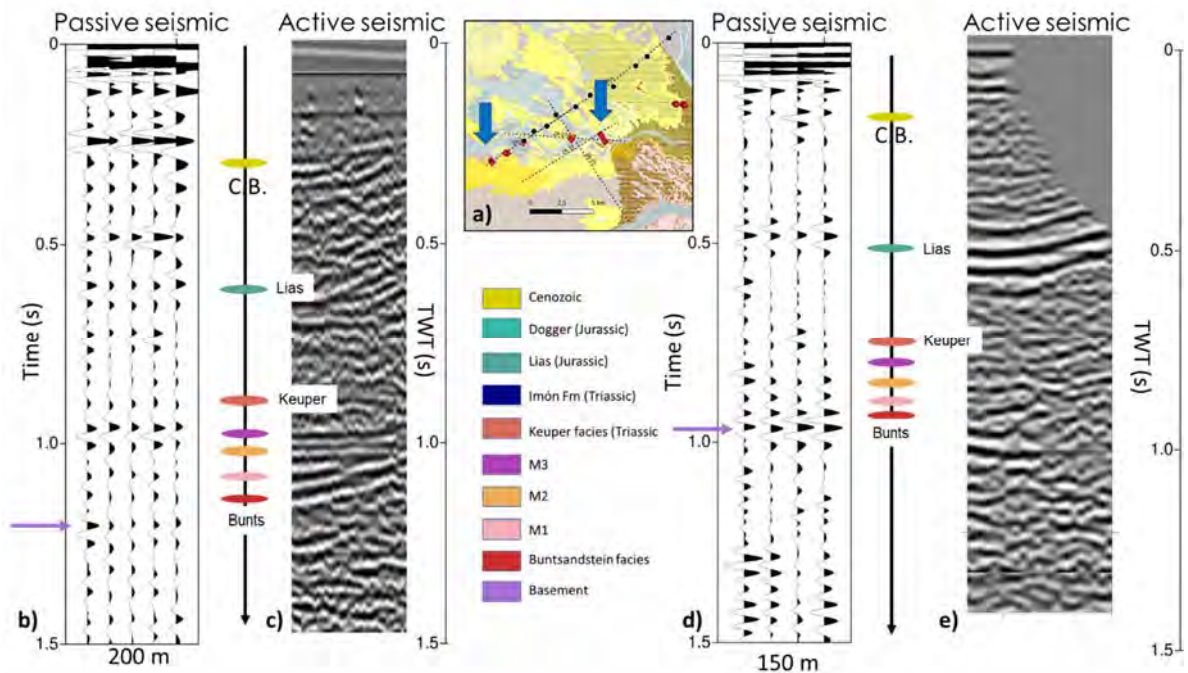


Figure 9-28.a) Sector of the map with the location of the seismic stations used to obtain the autocorrelation results (subsurface reflectivity) shown in b) and d). Purple arrows indicate the basement interpretation based on autocorrelation. c) and e): Zoom of the active seismic reflection section located in the vicinity of the seismic sections used in the application of the passive seismic method. The interpretation of the main contacts is also included.

9.3.2.2 Conclusions of the passive seismic

H/V method provided information about the Cenozoic base and an impedance contrast within the Jurassic sequence. The autocorrelation results have imaged the main impedance contrasts and help to constrain the bedrock top depth. Passive seismic methods have provided constraints for the interpretation of seismic reflection sections and gravimetric models. These results confirm the suitability of this cost-effective methodology for subsurface characterization in CCS site investigations. In addition, the application of these methods at the Spanish onshore site has led to collaboration with the Portuguese PilotStrategy project group. The Portuguese and Spanish teams are collaborating in the application of passive seismic methods in the Monte Real area (Lusitania Basin).

9.3.2.3 Results of the gravity modelling

A summary of the results of the gravity modelling along the re-interpreted seven seismic profiles and the three auxiliary profiles is shown on Table 9-1

Name	Direction to the strike	Anomalies range (mGal)	Total	
			amplitude (mGal)	RMS (mGal)
SW01	Perpendicular	-0.6 a 1.17	2.27	0.115
SW02	Perpendicular	-0.33 a 1.56	1.89	0.123
SW03	Perpendicular	-1.96 a 2.33	4.29	0.263
ZA-03	Perpendicular	-1.22 a 1.26	2.48	0.12
ZA-04	Parallel	-0.84 a 2.28	3.12	0.1
ZA-07	Perpendicular	-2.33 a 1.15	3.48	0.136
ZA-15	Oblique	-0.98 a 2.30	3.28	0.363
ZA-16	Parallel	-0.32 A 2.48	2.80	0.09
ZA-20	Oblique	0.04 a 1.85	1.95	0.09
ZA-21	Perpendicular	-1.13 a 1.62	2.75	0.09

Table 9-1 Summary of the gravity modelling results along the 10 profiles. In red, the worse adjusted profile, see explanation on the text.

As an example, prior to briefly summarize the main results of the gravity modelling, we describe in more detailed the modelling workflow of the preliminary interpretation along seismic profiles ZA-07 and ZA-07-P. The first interpretation of the seismic profile shows the Jurassic as an undifferentiated layer. Moreover, the model ends in a graben that has a flat top of the basement at c. 3 km depth (Figure 9-29).

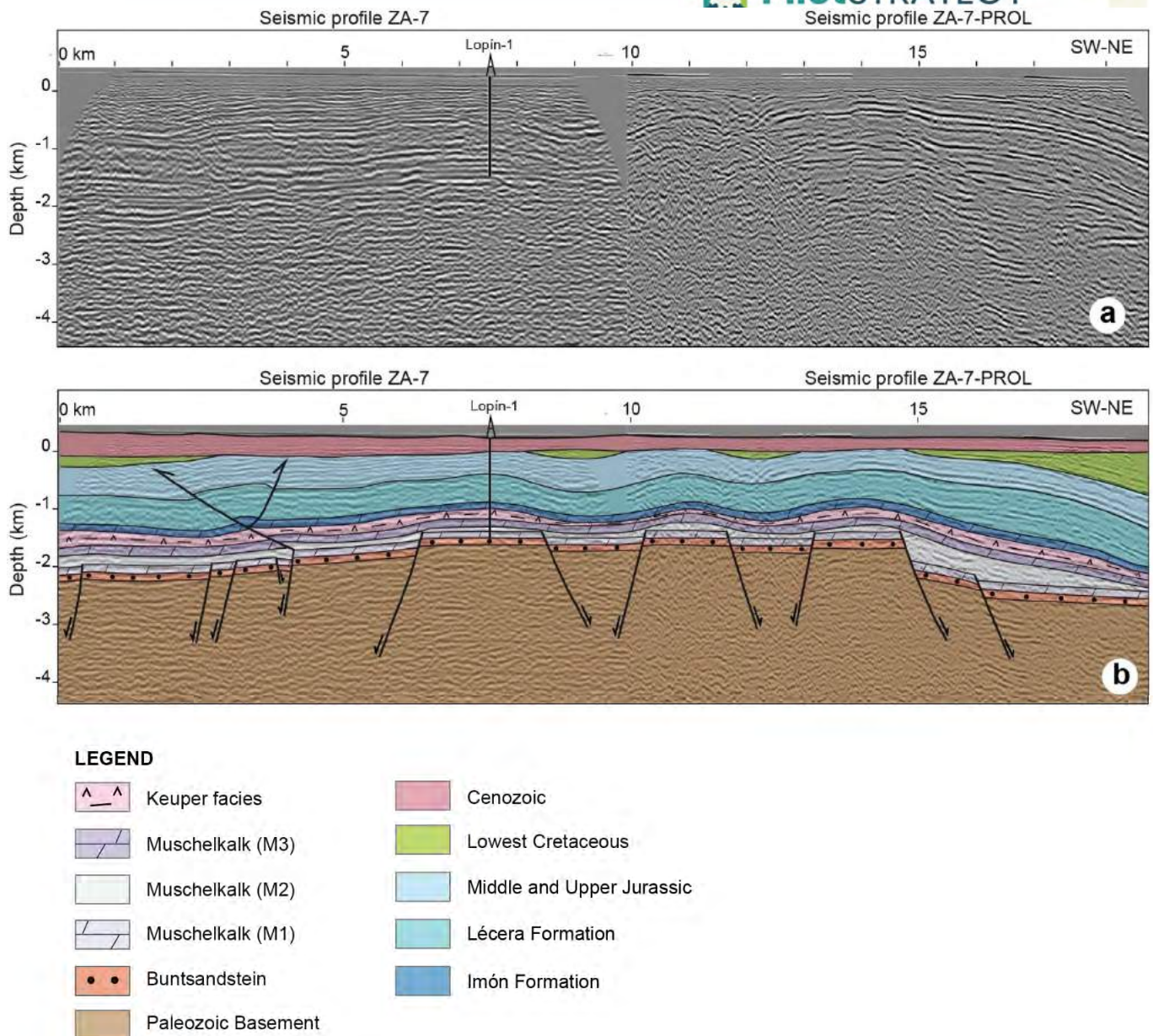


Figure 9-29 Initial geological cross section obtained from the interpretation of the seismic profile ZA-07.

Based on this first geological interpretation of profiles ZA-07 and ZA-07-P (Figure 3-29), when digitizing them into GM-SYS and calculating its gravimetric response, the gravity anomaly is adjusted only on the SW part of the profile (Figure 3-30). A revision of the density data log from the Lopín-1 borehole shows an important change in the density within the Jurassic rocks that allows dividing it in two distinct layers; an upper layer of Middle and Upper Jurassic, more calcareous, and a lower layer (namely Lécera Fm), containing anhydrites, with a higher density. In addition, the uncertainties associated to the seismic interpretation allow changes in the geometry of the top of the basement and Buntsandstein, M1 and M2 facies. In order to adjust the observed anomaly, we have thinned the M2 layer and tilted slightly the top of the basement together with the Buntsandstein and M1 layers. The models before and after the modifications are shown on Figure 9-30.

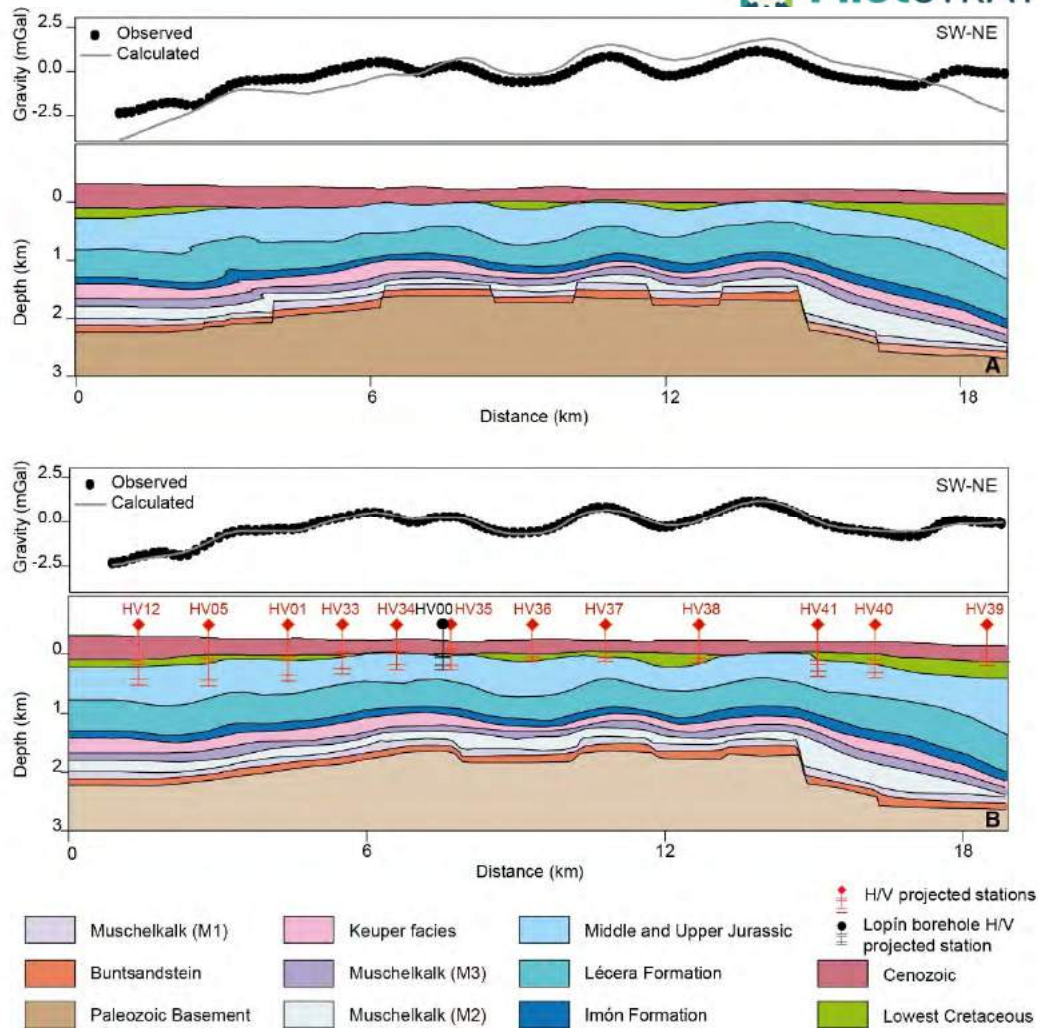


Figure 9-30 (A) Initial geological cross section based on the interpretation of the depth-converted seismic profiles ZA-7 and ZA-7-PROL. Please note that the corresponding observed and calculated gravity anomalies do not match. (B) Gravity-consistent geological cross section taking into account the H/V data and petrophysical data (density data used in the model is displayed in the units' boxes).

Figures 3-31 to 3-43 show the modelled cross sections in this work. In almost all modelled profiles, the adjustment between the observed and calculated gravity anomalies is very good, with the RMS (Root Mean Square of the difference between calculated and observed anomalies) is less than 5% of the total amplitude of the anomaly (Table 9-1). The only exception is Section ZA-15, where the RMS is c. 10% of the total amplitude of the anomaly. We will discuss the origin of this mismatch later on.

Along the SW01, Figure 9-31, the main modification was to decrease the thickness of the Purbeck by c. 100 m towards the end of the profile, with the anhydrites, Imón, M3 and M2 deepen towards the SW end and made these layers flatten out towards the NE end.

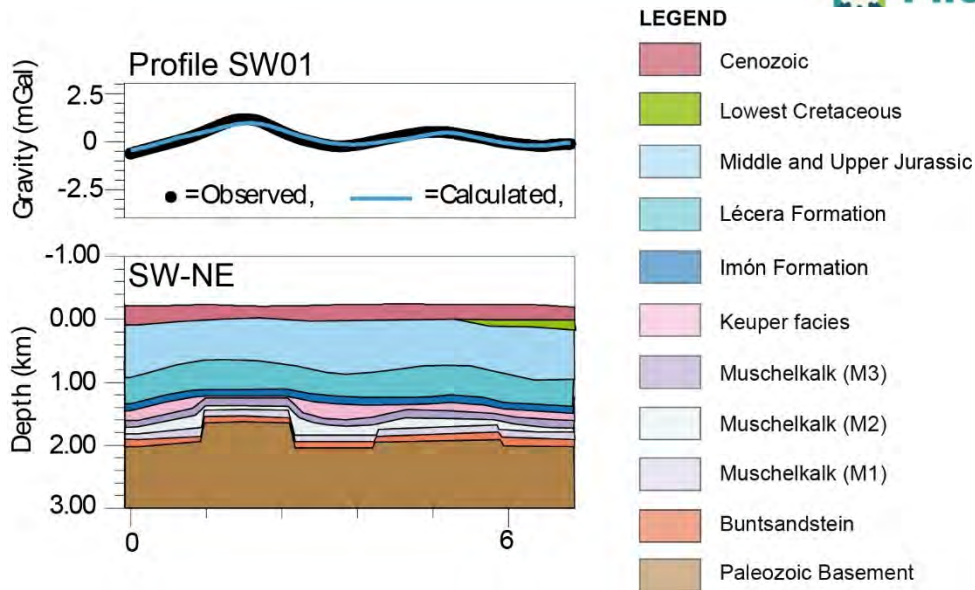


Figure 9-31 Gravity-consistent geological cross section SW01 based on geological information only. Distance in km, 1:1 scale. Next to the profile, legend used in all models.

The main modifications along SW2, Figure 9-32, have been to create a small cretaceous basin on top of the graben at the central part of the profile to fit the relative minimum. In addition, flatten out all the layers at the NE end of the profile from c. km 14 to make them parallel to the base of the Tertiary and made the layers deepen from c. km 14 to the end of the profile to fit the decrease on the observed anomaly.

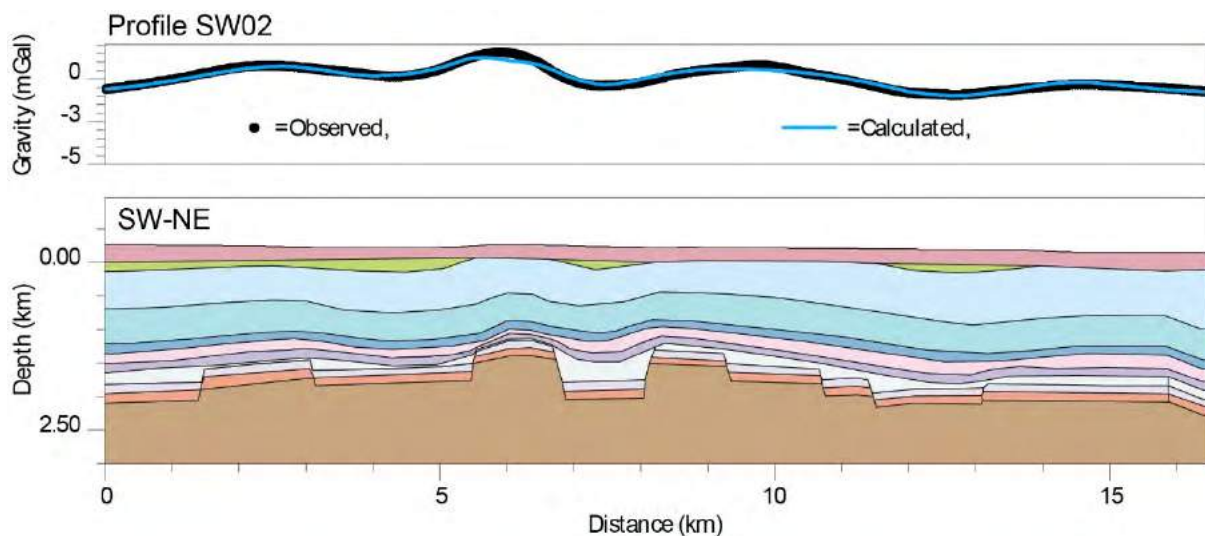


Figure 9-32 Gravity-consistent geological cross section. SW02 based on geological information only. 1:1 scale.

In SW03, Figure 9-33, the main changes regarding the geological model have also been to flatten out all the layers at the NE from km 16 to make them parallel to the Tertiary and to enlarge (5 km) and deepen (up to 500 m) the Purbeck basin. As this section intersects ZA-04, ZA-16 and ZA-15. Its central part is constrained by the interpretation of these seismic sections. The mismatches between the observed and calculated anomalies can be attributed to lateral density changes.

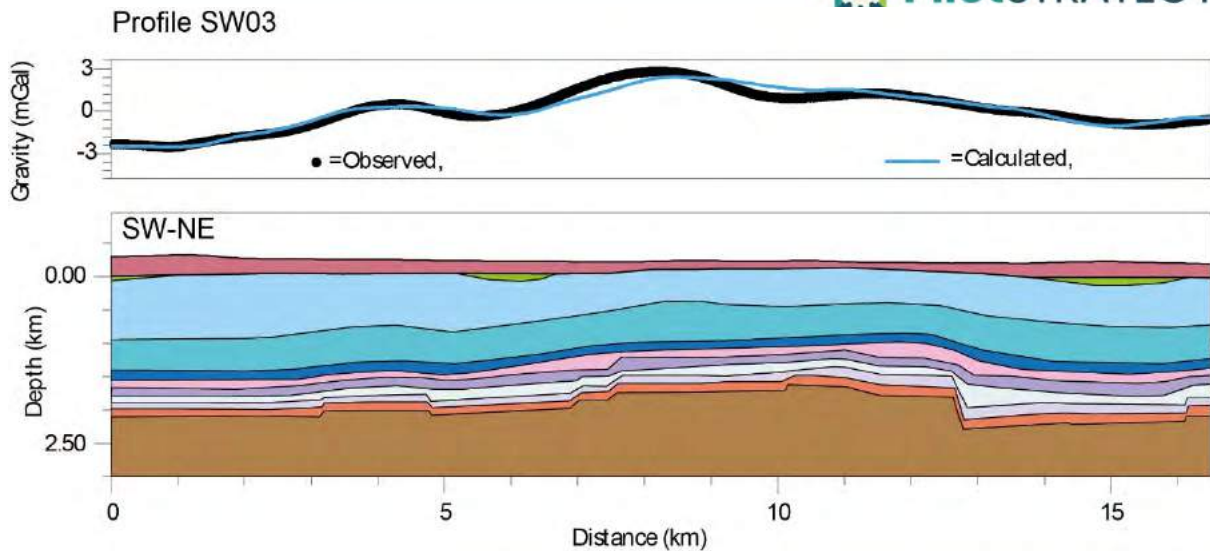


Figure 9-33 Gravity-consistent geological cross section SW03 based on geological information only. 1:1 scale.

Along profile ZA-03, Figure 9-34, we reshape the basement shallower by c. 100 m and made the layers flat towards the NE end of the profile, from c. km 11. We have also made slightly thicker the anhydritic layer (about 100 m) in order to fit the relative maximum whose centre is located at c. km 7.

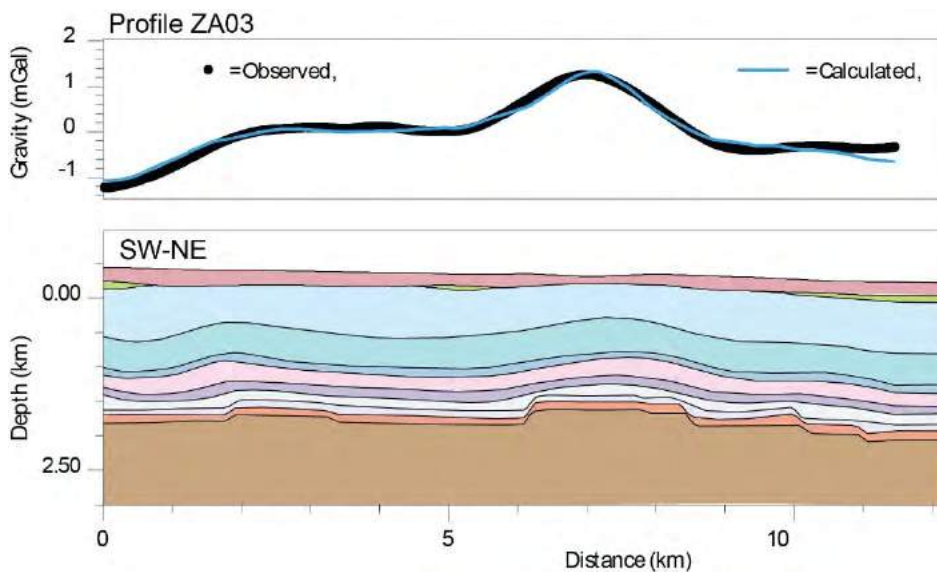


Figure 9-34 Gravity-consistent geological cross section. Modelled from interpretation of seismic line ZA03. 1:1 scale.

In ZA-04, Figure 9-35, we have made about 200 m shallower the top of the basement and the layers above from 0 to km 2 and change the thickness of the anhydritic layer (c. 100 m) to adjust the maximum and minimum centred on c. km 7 and c. km 9.5 respectively.

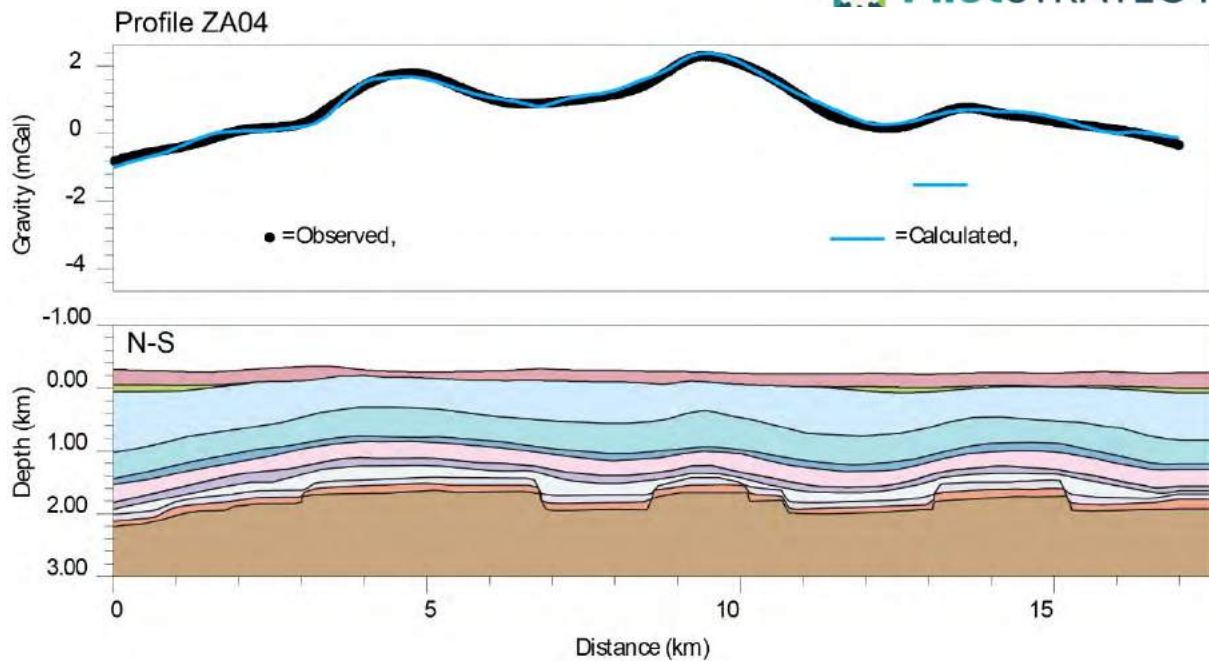


Figure 9-35 Gravity-consistent geological cross section. Modelled from interpretation of seismic line ZA04.

As indicated in the previous section, Profile ZA-07, Figure 9-36, was revised after its publication on GSL (Ayala et al., 2023) and an important change was made: a change on the orientation of the last fault at the NE end of the profile. This feature is more consistent with the geology and did not require considerable changes on the model.

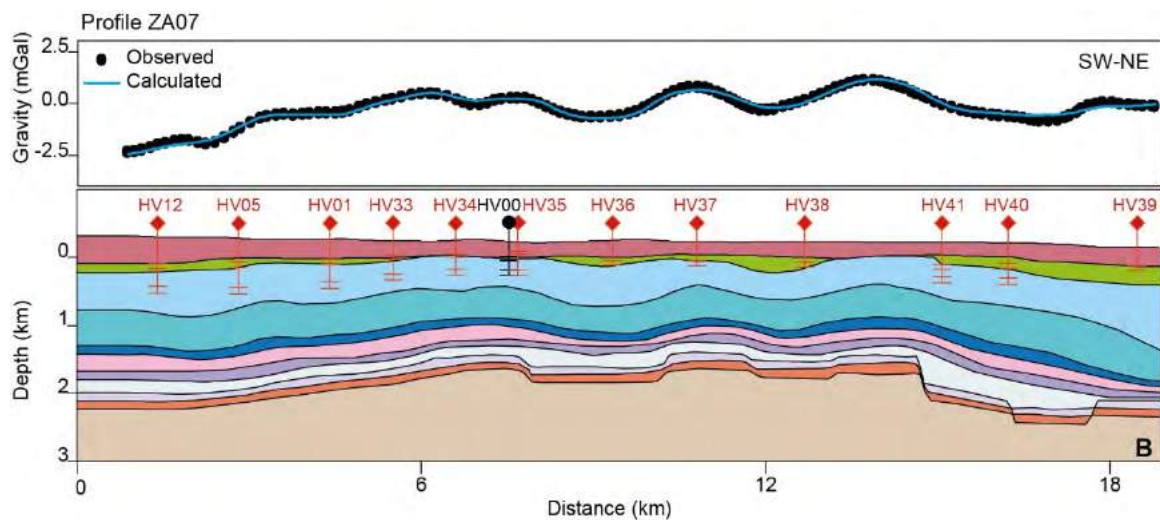


Figure 9-36 Gravity-consistent geological cross section taking into account the H/V data. Modelled from interpretation of seismic line ZA07.

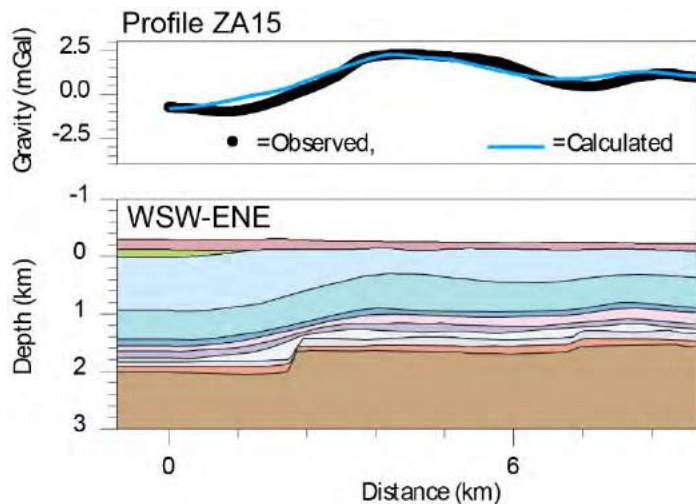


Figure 9-37 Gravity-consistent geological cross section. Modelled from interpretation of seismic line ZA15.

Along ZA-15 the interpretation of the seismic profile had a small uncertainty so it was only possible to slightly modify the base of the Jurassic by less than 80 m, Figure 9-37. Therefore, it has only been possible to adjust the general trend of the anomalies. Being the orientation of this profile oblique to the strike there are edge effects that cannot be considered due to the limitations of the software. In addition, the differences between the observed and calculated anomalies can be adjusted considering lateral changes of the density.

To adjust the ZA-16, Figure 9-38, profile it was only necessary to deepen progressively the base of the Jurassic between km c. 3.5 and c. 6 up to 100 m in the central part of this section.

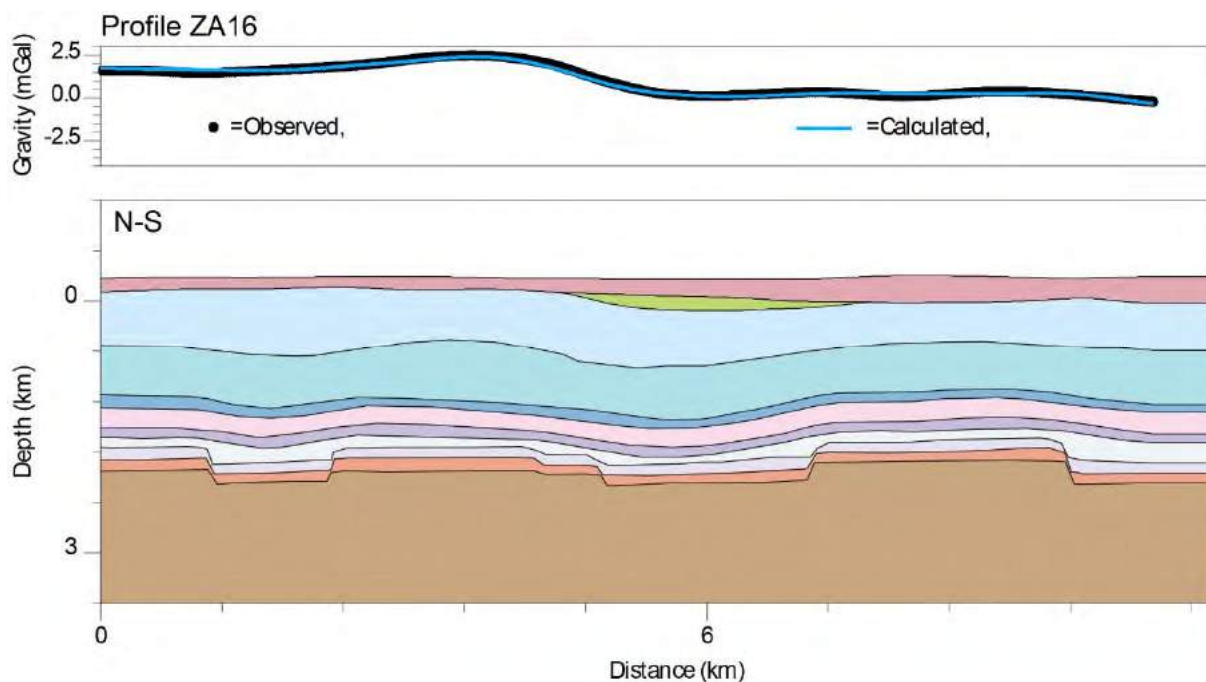


Figure 9-38 Gravity-consistent geological cross section. Modelled from interpretation of seismic line ZA16.

In ZA-19, Figure 9-39, the only modification necessary to adjust the observed anomaly has been to increase about 50 to 70 m the thickness of the Jurassic from the beginning of the profile up to km 2.26.

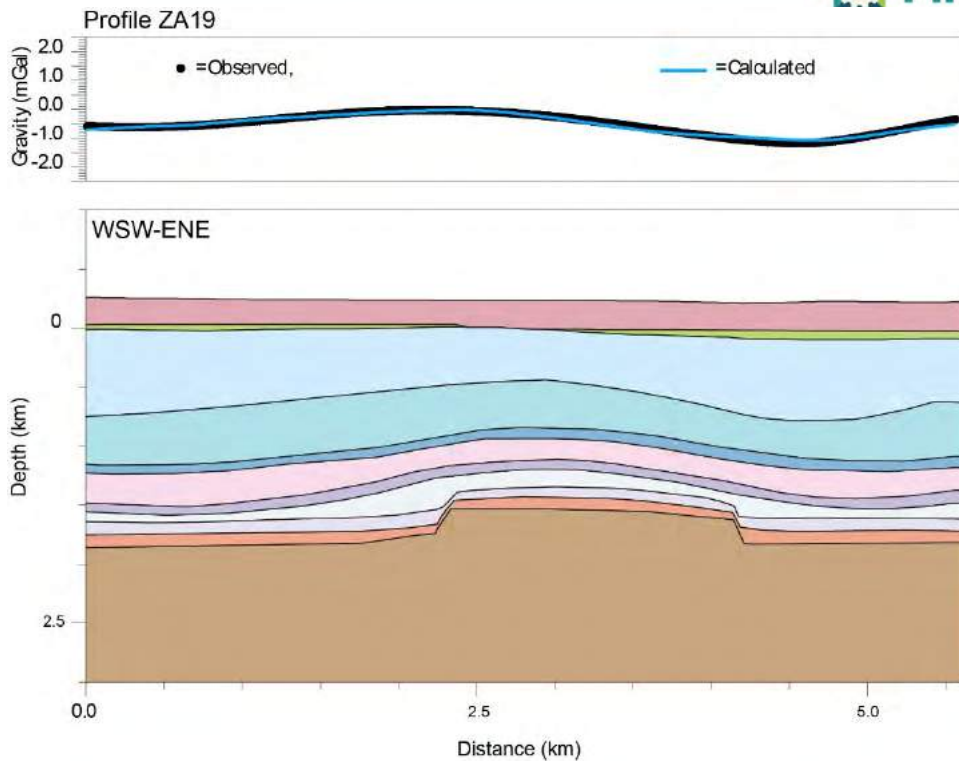


Figure 9-39 Gravity-consistent geological cross section. Modelled from interpretation of seismic line ZA19.

In ZA-20, Figure 9-40, it has been necessary to deepen up to 100 m the base of the anhydrites for the first c. 7 km to adjust the observed anomalies.

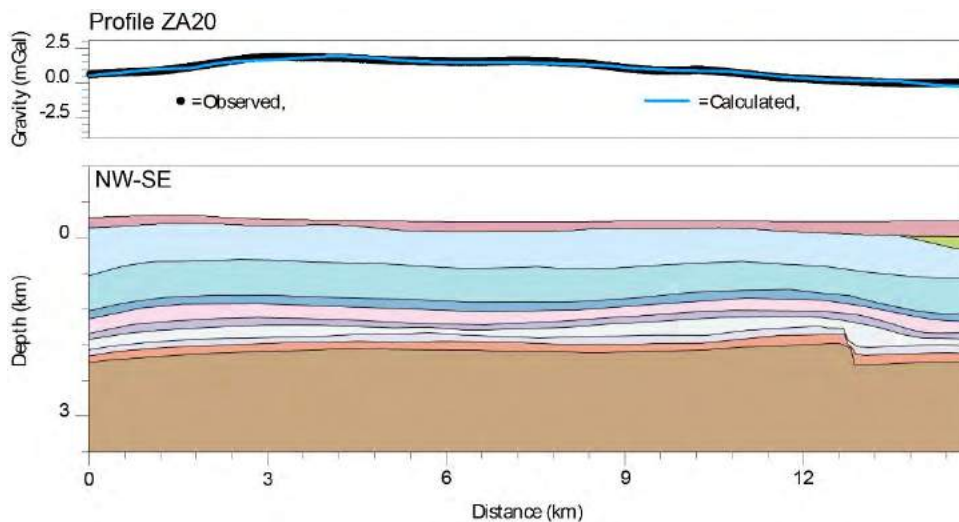


Figure 9-40 Gravity-consistent geological cross section. Modelled from interpretation of seismic line ZA20.

We have adjusted ZA-21, Figure 9-41, by making small changes on the geometry of the base of the anhydrites between 10 and 80 m, modifying the anhydritic layer to make its thickness approximately constant along the profile.

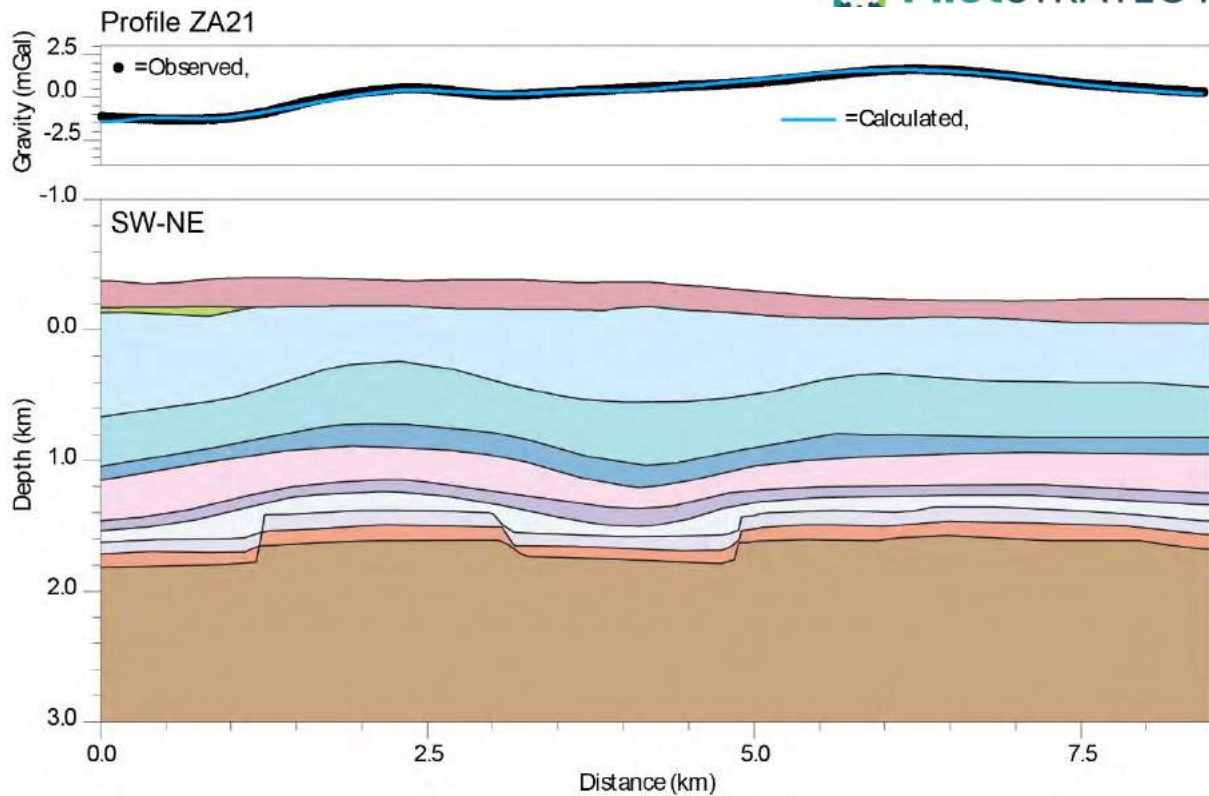


Figure 9-41 Gravity-consistent geological cross section. Modelled from interpretation of seismic line ZA21.

In profile ZA25 (Figure 9-42), the reinterpretation of the seismic profile indicates that the thickness of the anhydrites increase about 100 m at the southern part of the profile and the layers beneath deepen as a block from the beginning of the profile up to km 1.7. Moreover, the initial interpretation depicted a structure of horst-graben-horst-graben whereas the reinterpreted profile depicts a longer central horst with a low throw fault approximately in the middle and two and two grabens at both sides.

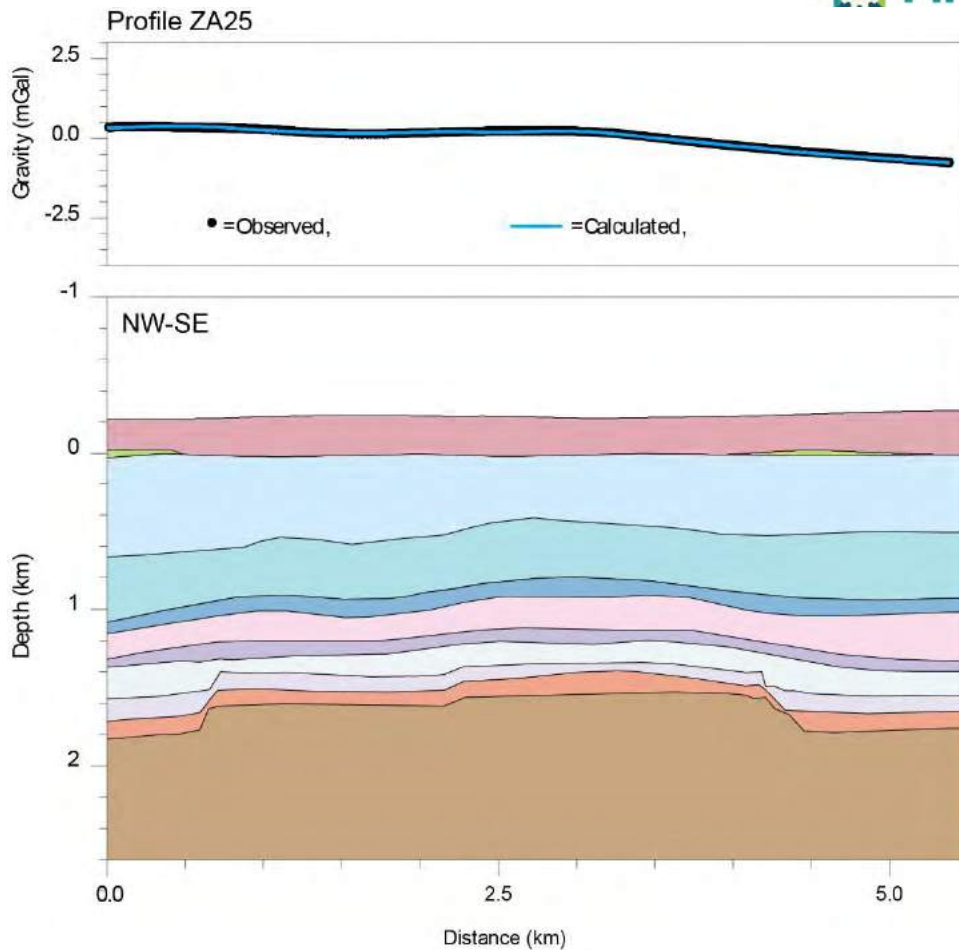


Figure 9-42 Gravity-consistent geological cross section. Modelled from seismic line ZA25.

Along the ZA27 profile, Figure 9-66, the only change that has been made was to modify the depth of the anhydrites up to 150 m in some places. These modifications have been necessary to preserve the seismic interpretation as much as possible, where the Imón and M3 Fms have important changes in thickness. The modifications on the anhydrites could have been less dramatic if the thickness of Imón and M3 could have been maintained (these two layers show different thickness along the profile).

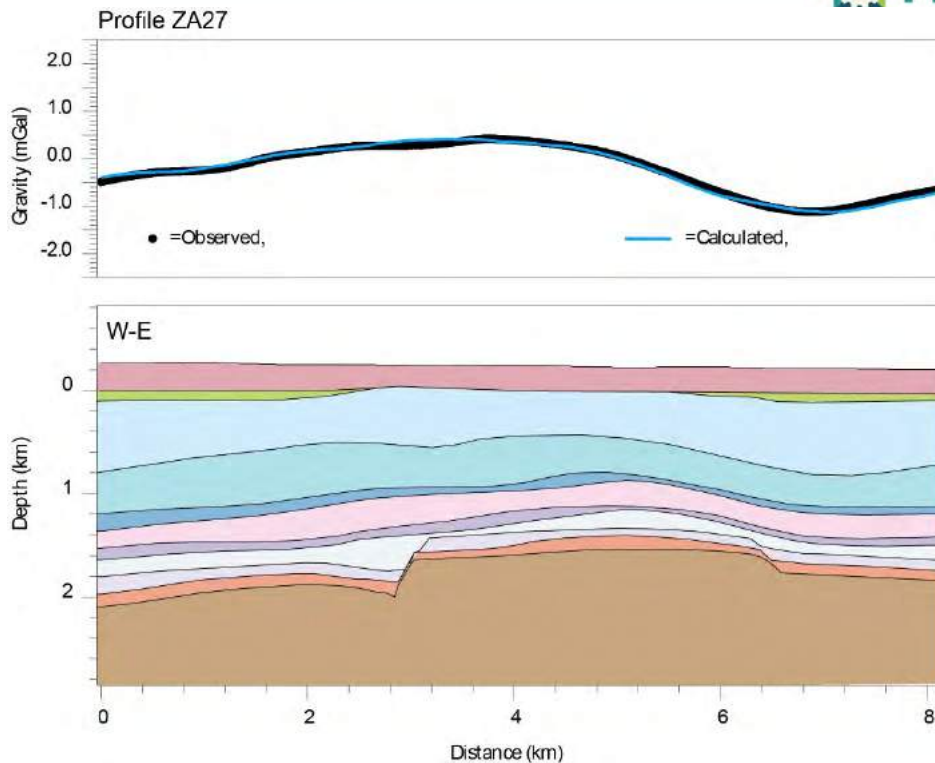


Figure 9-43 Gravity-consistent geological cross section. Modelled from seismic line ZA27.

9.3.2.4 Conclusions of the gravity modelling

The gravimetric modelling of the geological cross-sections derived from the interpretation of the seismic lines and the three new auxiliary geological cross-sections done (SW01, SW02 and SW03) has helped to better define the geometry and depth of the structures in those places where the reflectors of the seismic profiles were not well defined. In some parts of the seismic profiles, the reflector continuity was not clear enough to associate them to a particular interface or they did not displayed reflectors that could be associated to a given lithology. Moreover, the three new geological sections that have been modelled only with the gravity data have been very useful to constrain the lateral extension of the structures in the areas where the lack of seismic information made it difficult to model. On the overall, gravity modelling supports the interpretation of the Lopín structure as a succession of horsts and grabens where the faults that limit those structures only affect the basement, Buntsandstein and M1. Using 2D gravity alone it is not possible to define the exact dip and orientation of the faults but it is possible to conclude that all the faults have a high dip and not very big throw (in

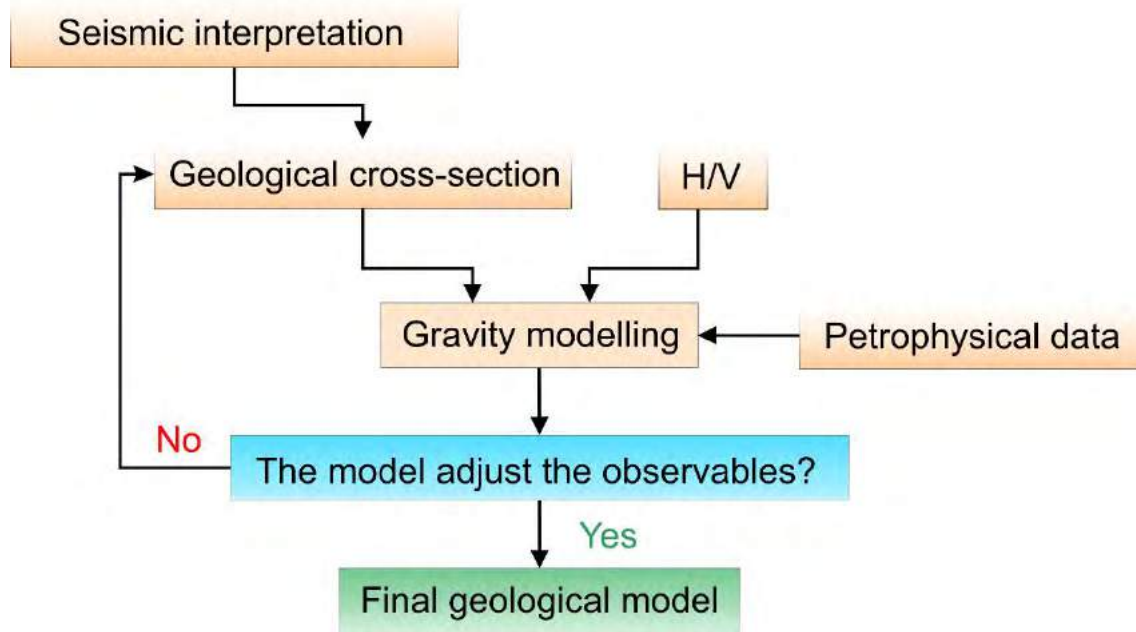


Figure 9-44 Workflow of the methodology applied in this work for the 2D gravity modelling (from Ayala et al., 2022).

9.4 Logs and well data analysis

9.4.1 Methodology Introduction

The methodology used in this study is based in a well know oil and gas industry methods for facies and petrophysics analysis. However, the quality of the data available is poor and scarce. The wells in the area were drilled on the 70's-80's of the past century, the LAS files used came from old logging hard copies scanned and digitalized. The information annexed to these logs is not as good as it is in the present logging operations, there is a lack of information in the headers and the log suites run on these wells are not as comprehensive as we would like to be. That is, commonly used logs, like the electrical resistivity, spontaneous potential (SP), Gamma Ray (GR), Sonic (DT) or Caliper, were not always run. The tool that was usually run is the Sonic (Slowness) curve DTC-compressional wave slowness (there are not DTS curves-shear wave slowness). The Temperature data mostly consist of just one temperature recorded in the first log run of every logging operation. Pressures were evaluated using Composite logs data, Mud densities used, mud gains or losses reported, Gas peaks while drilling and, in a very few cases, Production Test data in different formations. Needless to say that for more accurate temperature estimation, using Horner Plot method, we need more than 2 temperature records in each logging operation. The Ebro-1 and Ebro-2 have the most comprehensive data sets and therefore they have been used to better define the petrophysics and e-facies, these wells had also a Neutron Porosity and Bulk Density logs (NPHI/RHOB), which are very helpful to define not only the lithological information but the petrophysical characteristics of each formation.

About porosity evaluation, luckily there are some SWC (Side Wall Cores) porosity analyses in EBRO-2 well and, moreover, we had calculated porosity from core samples in the Chipriana-1 well. Notably the EBRO-2 reported porosities on their SWC are much higher than the calculated based on the logs. On the other hand, the porosities that we calculated in the Chipriana-1 well (Buntsandstein very top facies) are consistent with the Sonic-DT porosities estimation. Since the porosity data from EBRO-2

well report seem very rough and we have better controlled the sampling and analysis in the Chipriana-1 core, decision was made to use this last one to compare laboratory data against logs porosity assessment.

The volume of shales (Vsh) has not been analysed in these samples, so we have compared Vsh in Chiprana-1 core Spectral Gamma (using Thorium isotope volume) with the Vsh calculated with the standard GR from the well log. Both data seems to be coincident.

On top of that, the wells examined are far away from the area of interest, unfortunately the Lopín-1 well has almost no data from the reservoir. The majority of these wells are located to the North-East or South-East, so there are no data to the West of the area of interest (Figure 9-45).

The following table lists the distances between Lopín-1 and the other wells.

Well	YUTM (m)	XUTM (m)	Z (m) KB	Distance from LOPÍN-1 (Km)
LOPÍN-1	4580522	702543	227.45	0
LA_ZAIDA_1	4578553	716464	165	14.06
MONEGRILLO-1	4611180	714284	378	32.83
CHIPRANA-1	4584099.7	736141	315	33.79
EBRO-1	4585150	736510	332.7	34.28
EBRO-2	4614391.1	740962.6	471	51.22
ZUERA-1	4633160	678138	354	58.02
CANDASNOS-1	4599395.6	758735.7	282.4	59.28
CASPE-1	4562906.7	760904.7	284.4	60.96
SARIÑENA-1	4630812.9	741839.3	354.15	63.82
BALLOBAR-1	4605165.6	762843.7	281	65.14
FRAGA-1	4598244	769125	301	68.9
MAYALS-1	4582376.5	796257.2	359.7	93.73

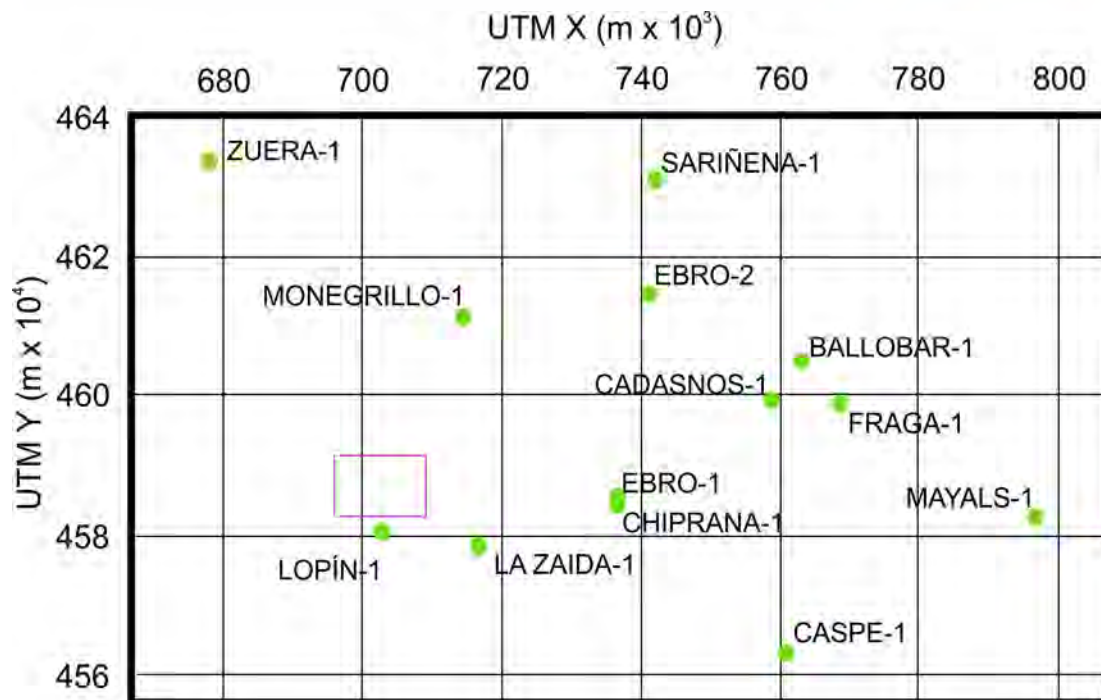


Figure 9-45 Wells location map in Ebro Basin. Area of interest = purple box (Coordinates UTM ETRS89).

9.4.2 Reservoir Pressure and Temperature Assessment

To estimate these two aspects, essential for the project, we had used former wells reports and log header data. Unfortunately, the data are not complete, so an effort was made to estimate the likelihood of these values.

Temperature

In terms of temperature the data come from the reported maximum reached temperature of the logs and from production data. Since these temperatures are lower than the likely reservoir temperature Horner (1951) established a method that tried to compensate the cooling effect of the flowing mud during the drilling operation. It consists in the relationship between the recorded temperature and the heating up after well circulation. Usually, when a number of log runs are performed, first log run will record lower temperature than later logs. So, in a cross-plot of recorded temperature versus time from last circulation we could see how the temperature will be closer to the original reservoir data. The only well that has this set of data is the Ebro-2, and only 2 points (three are recommended). Other feature needed is the last circulation lasting, which has been considered to be around 4 hours as a very common figure in this kind of operations (Figure 9-46).

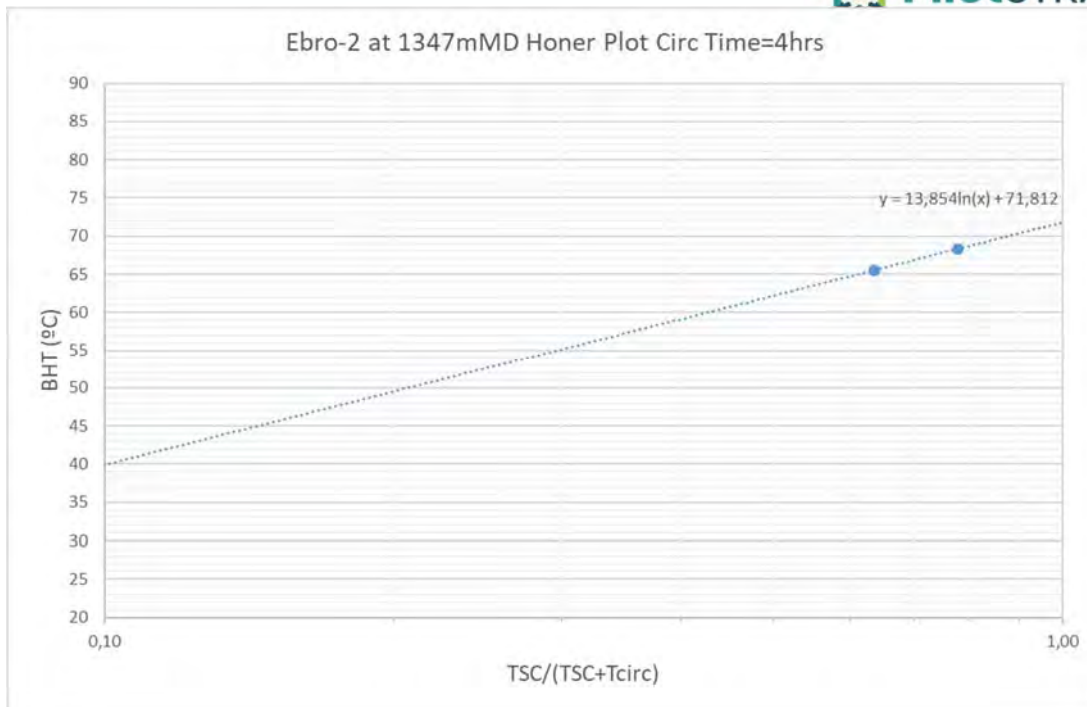


Figure 9-46 Horner plot for well temperature correction. In Ebro-2 just two points were available.

Where:

- BHT= Bottom Hole Temperature,
- TSC= time since last circulation
- Tcirc= Time of last circulation.

The variation of the Tcirc has little effect in the final outcome, i.e. Tcirc=1hrs will make the estimated temperature to be 71.03°C. Since the rest of the wells have only one BHT recorded and rarely mention the time after last circulation we have assumed a correction similar to the Ebro-2, luckily there are Temperature data from DST's (Drill Stem Test) that help us to support these data.

Pressures

As a first approach, to evaluate the reservoir pressure, well reports have been studied to extract data that may indicate the pressure variation with depth. The DST's are very useful since they usually report reservoir temperatures and pressures. Other data used are the mud weights used during drilling operations and the reported mud losses or gains while drilling as well as gas peaks. But these last ones give just a threshold of pressures in the drilled zone, very high mud weight will result in mud losses meanwhile very low mud weight will produce large gas bubbles or influx of formation fluids into the wellbore. The common practice in the drilling operations is to have a hydrostatic pressure into the well just slightly above the maximum expected formation pressure.

9.4.3 Log analysis methodology

The well logs used are old hard copies scanned and digitalized. The main exploration campaigns in this area were done in the 70's – 80's of the pass century. As said above, no all wells have a complete suite of logs, so it was necessary to select what curves could be used to characterize the petrophysics in order to have a homogeneous method that could be easily compared between wells. The most common log suite used in these old wells consist in Resistivity (LLD-LLS), Gamma Ray (GR),

Caliper (CAL) and Sonic (DT, only DTC). Other logs like Neutron porosity (NPHI) / Bulk Density (RHOB), Spontaneous Potential (SP) and Microresistivity (MLL) were rarely run. Nevertheless, we have used EBRO-1 and EBRO-2 logs to better characterize the formations since they have a comprehensive set of logs.

Volume of Shales

To calculate the volume of shales a standard equation has been used. It is based on the assumption that the GR readings respond mainly to the quantity of shale in the formation, so the ratio is as follows:

$$GR_{index} = \frac{GR_{log} - GR_{sand}}{GR_{shale} - GR_{sand}}$$

GR values used for sandstone or shale were “cleaned” of anomalies to avoid very long interval with anomalous values, to do so we select a GR Percentile 95 for the GR_Shale and percentile 5 for the GR_Sandstones, all of this considering only the investigated formation.

These values have been matched with the Vsh calculation in the Chipriana-1 core, in this well we have two different set of data (mainly in Buntsandstein B2 formation). Spectral Gamma Ray was run over core and it is compared with the well GR log data. The equation to evaluate Vsh on the core use the Thorium content (measured in ppm, it is reckoned to be related to the shales content) in the same way the GR-index:

$$Vsh(Th) = \frac{Th(log) - Th(min)}{Th(max) - Th(min)}$$

Chipriana-1 well	Vsh (GR index)	Vsh (Th) core
Average	56.92%	60.11%
Median	61.44%	60.95%
Standard Deviation	23.13%	22.52%
P10	26.56%	28.16%
P50	61.44%	60.95%
P90	84.18%	89.65%

Evaluation of porosities with Sonic (DTC)

To estimate porosity from the sonic logs, two alternatives were considered, the so called Wyllie’s equation and the RHG simplified equation (Raymer et al. 1980).

Wyllie equation (Wyllie et al. 1958):

$$\phi = \frac{DTp - DTmatrix}{DTfluid - DTmatrix}$$

Simplified RHG equation:

$$\phi = 0.625 * \frac{DTp-56}{DTp}$$

Where $56 \mu\text{s/ft}$ is the DTC of rock matrix (Sandstone) and $189 \mu\text{s/ft}$ is the DTC of the fluid (fresh water), $D\text{T}_p$ is the value of DTC curve at certain depth and ϕ is the calculated porosity. In the Chipriana-1 well there was a chance to compare the DTC curves with the porosity data taken from the core samples. The Wyllie equation is the Sonic equation that better match the laboratory data. The constant used to adjust the porosities (0.625 for RHG) is considered like an averaged correction for a quick evaluation.

	Porosity Wyllie Sonic	Porosity RHG simplified Sonic	Porosity-cores
Average	10,03%	12.78%	9.32%
Median	8,59%	10.79%	9.11%
Standard Deviation	5,70%	9.10%	4.00%
P10	5,76%	8.21%	
P50	8,59%	10.79%	9.11%
P90	15,97%	17.37%	

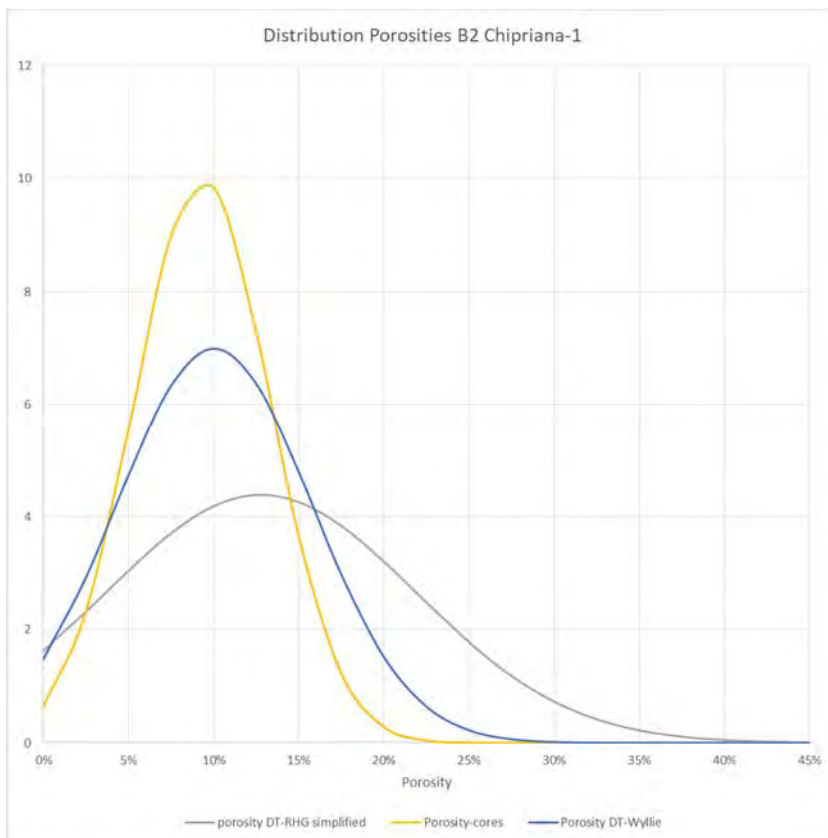


Figure 9-47 The Normal Distribution of porosities in Chipriana-1 well, Buntsandstein B2 formation. Wyllie seems to better fit the core porosity data.

Therefore, Wyllie equation is used to estimate the porosity in this study. This equation is used as well to estimate the porosity in the Muschelkalk Dolomies, but the DTC for dolomitic matrix is 44 $\mu\text{s}/\text{ft}$.

Evaluation with Resistivity curves

These logs have been widely used to calculate porosities in the oil industry. It is not intended here to explain the whole methodology to do so, but let's just say that there are some data needed in order to have a better porosity evaluation:

- Formations Temperature
- At least shallow and deep resistivities curves.
- Resistivity of the mud filtrate at laboratory temperature (R_{mf}).

Unfortunately, there is little consistency in the former wells logs. The set of data needed is not always there. Therefore, in order to have an equivalent porosity evaluation for the basin, the resistivity method is secondary, it is preferred to use the SONIC and NPHI/RHOB method instead.

However, when it is feasible, the porosity evaluation method used is Archie's Method (Archie, 1942).

All wells in this area give no Oil or Gas significant saturations, i.e. water saturation is assumed to be 1.

Formation Water resistivity is calculated by this equation at the cleanest sandstone in the formation:

$$R_w = R_{mf} \frac{\text{Resistivity Deep}}{\text{Resistivity Shallow}}$$

R_{mf} at that depth and temperature (Celsius).

$$R_{mf} = R_{mf \text{ at test }} \left(\frac{\text{Temperature MF test} + 21.5}{\text{Temperature at depth} + 21.5} \right)$$

Porosity with resistivity Equations:

Archie's equation (Archie, 1942):

$$S_w = \left(\frac{a * R_w}{\phi^m * R_t} \right)^{1/n}$$

- $a = 0.81$ (Porosity & Tortuosity Factor)
- $m = 2.00$ (Cementation Factor)
- $n = 1.80$ (Saturation Exponent)
- R_w = formation water resistivity at formation temperature
- R_t = true resistivity of the formation
- S_w = water saturation of the uninvaded zone
- Φ = Porosity

Neutron Porosity / Bulk Density

These logging tools have proved to be very useful to analyse reservoirs. The method is not as straight forward as the others since they need to cross-plot both data like the in Figure 9-48:

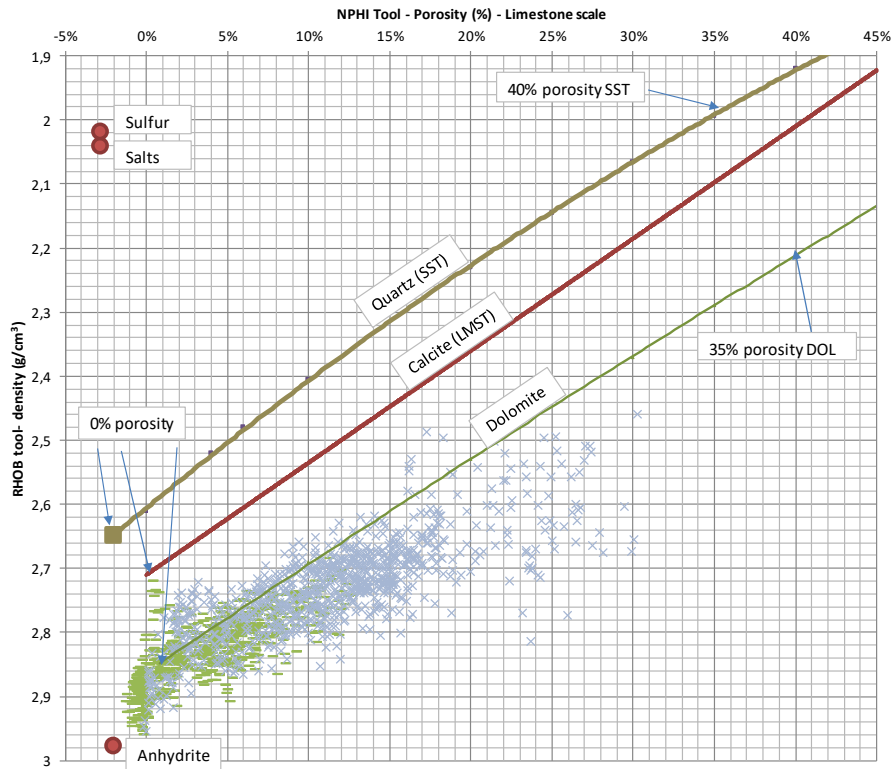


Figure 9-48 NPHI in Limestone scale needs no correction for True Porosity in Limestones (red straight line). But in Sandstones and Dolomites the NPHI needs to be recalculated (see Figure 3-57). Modified from Schlumberger log charts (2009).

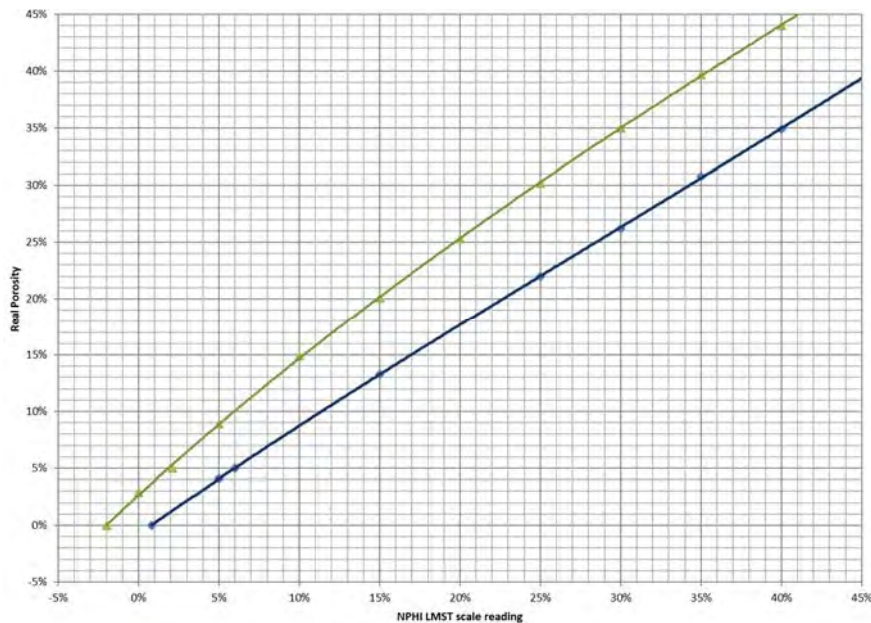


Figure 9-49 Correction of porosities from NPHI in Limestone Scale to Sandstone (green line) or Dolomites (blue) for non-saline formation water. Modified from Schlumberger log charts (2009).

With these charts we can calculate true porosity of the sandstones (Buntsandstein reservoir) and Vsh. For Vsh calculations, however, we need to build in a triangle in the Figure 9-48 in which one corner is the shale point (we select the shaly formations and plot it in the chart) and 0% shale will be a line (let's called it 0%Vsh) from sandstone with 0% porosity to a point that marks 100% porosity at

fluid density (for instance 1 g/cm³). When we plot NPHI-RHOB data, each point has a certain distance to the 0%Vsh line. Vsh is determined by the ratio of this distance to the shortest distance between the shale point (100% Vsh) and the 0%Vsh line.

We could use the RHOB curve (density) as well to evaluate the porosities:

$$\phi = \frac{\rho_{ma} * \rho_{bulk}}{\rho_{ma} * \rho_f}$$

Where:

- ρ_{ma} = density matrix
- ρ_{bulk} = density bulk
- ρ_f = density drilling fluid (salt fluid \approx 1.1 g/cc)

Compared different Porosity calculations methods

After a quick appraisal of all these previous methods in wells where all these curves were present we could finally evaluate the differences between them in the Buntsandstein formation. EBRO-1 is used here, since is the closest and more detailed well.

As in the Chiprana-1, the Sonic-RHG method gives much more porosity that the other methods (Figure 9-50):

Ebro-1 Buntsandstein B1 Formation Porosity evaluation					
	Archie-Res	RHG-Sonic	Wyllie-Sonic	RHOB PHIE	PHIE NPHI/RHOB
median	11.29%	13.39%	11.47%	10.90%	11.05%
Average	11.75%	13.23%	11.35%	10.37%	10.77%
Stan Dev	0.02	0.02	0.03	0.04	0.03
P10	8.81%	10.98%	8.83%	5.51%	6.21%
p50	11.65%	13.39%	11.47%	10.90%	11.05%
p90	14.94%	15.70%	14.13%	14.92%	15.12%

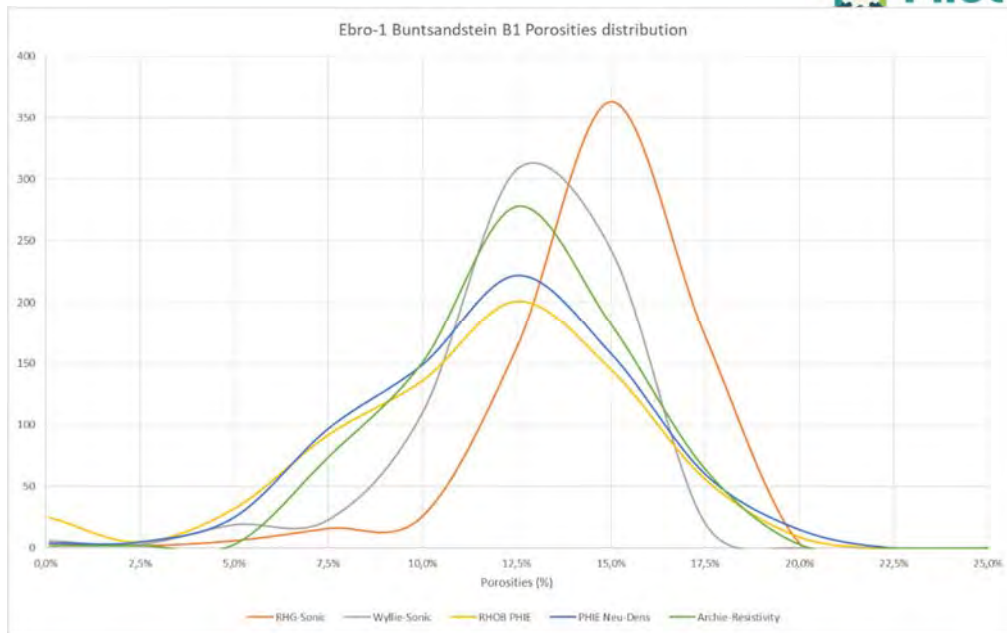


Figure 9-50 Distribution of porosities in the Buntsandstein B1 formation, Ebro-1 well.

9.4.4 Reservoir Pressure and Temperature Assessment

To estimate these two data, we had used former wells reports and log header data.

Temperature

The temperatures recorded in the wells and probable maximum temperatures are:

WELLS	Thermometer depth SS	Measured Temp.	Assumed HORNER-PLOT Temp	Geological Formation
Max rec temp Ebro02-DST01	793.00	92.22	92.22 (*)	Above Keuper
Max rec temp Ebro02-DST02	1623.00	72.22	72.22	M3
Max rec temp Ebro02-DST03	2400.00	85.00	85.00	M2
Max rec temp Ebro02-WL01	1343.00	65.55	71.81	KEUPER
Max rec temp Ebro02-WL02	1332.00	68.33	71.81	KEUPER
Max rec temp Ebro01-WL01	232.00	34.00	37.70	TERTIARY
Max rec temp Ebro01-WL02	1147.00	55.00	61.57	M3
Max rec temp Ebro01-WL03	1634.00	68.00	74.57	PALEOZOIC
Max rec temp Lopín01-WL01	1398.20	56.70	61.91	BUNT
Max rec temp CASPE01-WL01	1524.60	55.55	64.46	PALEOZOIC
Max rec temp MAYALS01-WL01	1041.30	58.33	64.90	??
Max rec temp MONEGRILLO01-WL01	762.00	56.00	59.70	Above Keuper
Max rec temp CADASNOS1-DST1	970.60	59.00	59.00	Above Keuper
Max rec temp CADASNOS1-DST2	1240.60	70.00	70.00	Above Keuper
Max rec temp CADASNOS1-WL01	1277.60	63.00	69.57	KEUPER
Max rec temp SARIÑENA1-WL01	1695.85	70.00	76.57	KEUPER
temp CHIPRIANA-1 DST	566.00	60.00	60.00	Above Keuper
temp CHIPRIANA-1 DST	594.90	53.00	53.00	Above Keuper
temp CHIPRIANA-1 DST	1257.20	60.00	60.00	M2
temp CHIPRIANA-1 DST	1310.70	65.00	65.00	M1
temp CHIPRIANA-1 DST	1331.50	68.30	68.30	M1
temp CHIPRIANA-1 DST	1351.20	67.70	67.70	M1

temp CHIPRIANA-1 DST	1382.80	75.55	75.55	M1
temp CHIPRIANA-1 DST	1440.70	70.00	70.00	BUNT
temp CHIPRIANA-1 DST	1457.20	68.30	68.30	BUNT
temp CHIPRIANA-1 DST	1471.20	70.00	70.00	BUNT

(*) Most likely wrong data

Gradient EBRO-2	31.6	Celsius/km
Gradient EBRO-1	30.5	Celsius/km
Gradient LOPÍN-1	29.2	Celsius/km
Gradient CASPE-1	27.6	Celsius/km
Gradient MAYALS-1	36.0	Celsius/km
Gradient MONEGRILLO-1	40.4	Celsius/km
Gradient CADASNOS-1	36.5	Celsius/km
Gradient SARIÑENA-1	30.3	Celsius/km
Gradient CHIPRIANA-1	31.1	Celsius/km

Pressures

As a first approach to evaluate the reservoir pressure, well reports have been studied. The DST's have proven to be very useful since they provide reservoir fluid temperatures and, usually a reservoir pressure appraisal. Other data used are the mud weights used during drilling operations and the reported mud losses or gains while drilling as well as gas peaks. But these last ones give just a threshold of pressures. (example of pressure chart in Figure 9-51).

EBRO-2 Pressure - Depth Plot

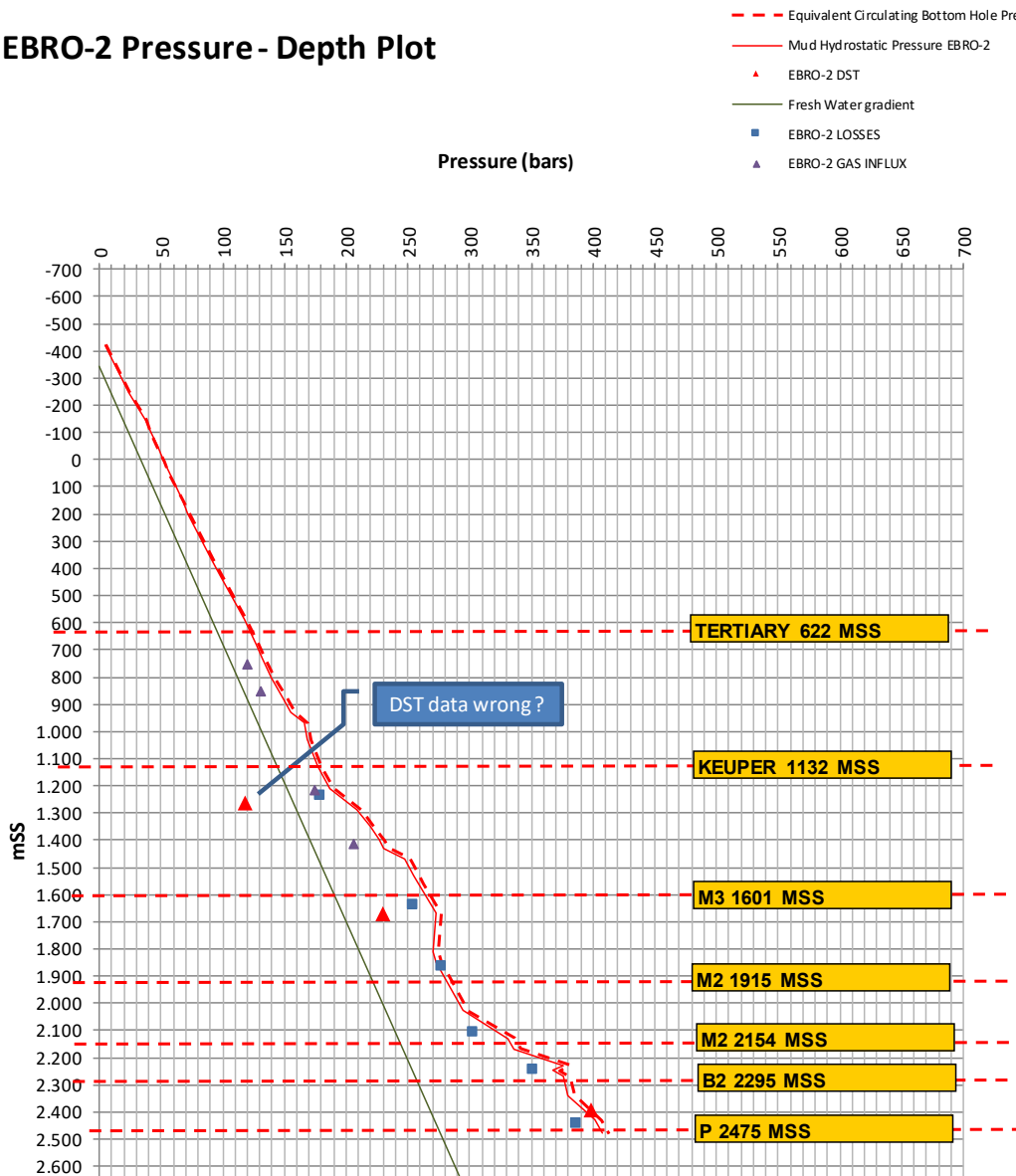


Figure 9-51 Ebro-2 pressure data versus depth (SS), red lines are the mud density data and the Equivalent Circulation Density (probable).

The pressures measured with DST in Cadasnos-1 (37Km E from Lopín) and Sariñena-1 (30Km NE from Lopín) are coherent with the fresh water hydrostatic pressure which could indicate a communication of the reservoir with surface water inputs. The rest of the studied wells show pressures well above the hydrostatic. Specifically, the closest wells are summarized at the following table.

Wells	Distance from Lopín	Equivalent fluid density gradient at Buntsandstein	Formation Pressure at Buntsandstein	Top Buntsandstein
MONEGRILLO-1	32.83 Km	1.26 g/cm ³	162 bar	909m SS
CHIPRANA-1	33.79 Km	1.25 g/cm ³	217 bar	1392m SS
EBRO-1	34.28 Km	1.22 g/cm ³ (1)	205 bar (1)	1341m SS

(1)- from mud density data.

9.4.5 Logs analysis

We had paid special attention to the facies that comprise the Reservoir. In addition, we studied roughly the overlying facies: Muschelkalk and Keuper, in order to characterize sealing capacities of these facies.

The Buntsandstein has been split in three parts: base conglomerates, middle mainly clean sandstone sequences (Aranda Formation) and shaly top formation (Carcalejos and Rané Formation) (Figure 9-68).

Buntsandstein Conglomeratic bottom.

This facies has been drilled in few wells throughout the basin, it mainly consists in conglomeratic channels interbedded with siltstones and sandstones (see stratigraphy section of this report). This formation is right on top of an erosive discordance over the Paleozoic rocks. In the well logs it is characterized by an increase in electrical resistivity, density and slowness (DT) logs. The gamma ray (GR) curves show a diverse shale volume (Vsh) between wells, most likely related to the distance to the source area (Figure 9-52).

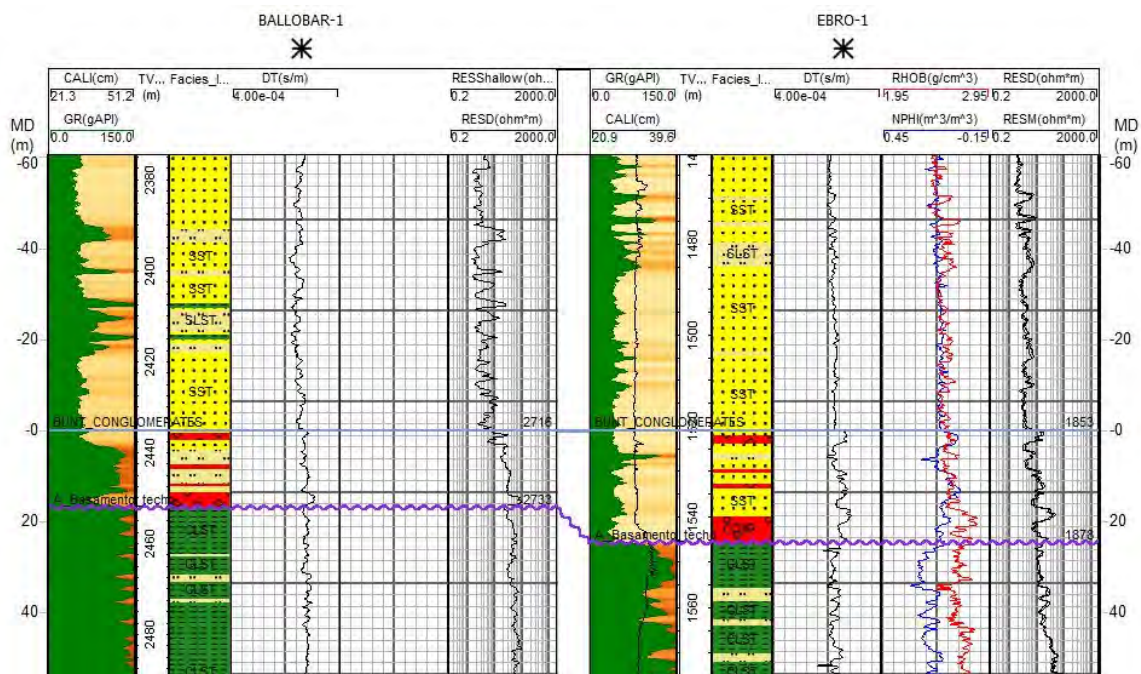


Figure 9-52 Example of logs response in the Buntsandstein conglomeratic bottom.

Different porosities calculated in Ebro-1 are shown in the Figure 9-53 left, middle graph is Vsh and right graph is GR-Caliper. At the bottom NPHI-RHOB (Porosity/Density) Vsh is bigger than Vsh from GR-Index. Caliper data shows some cake, note that in the figure the bit diameter is the dash line.

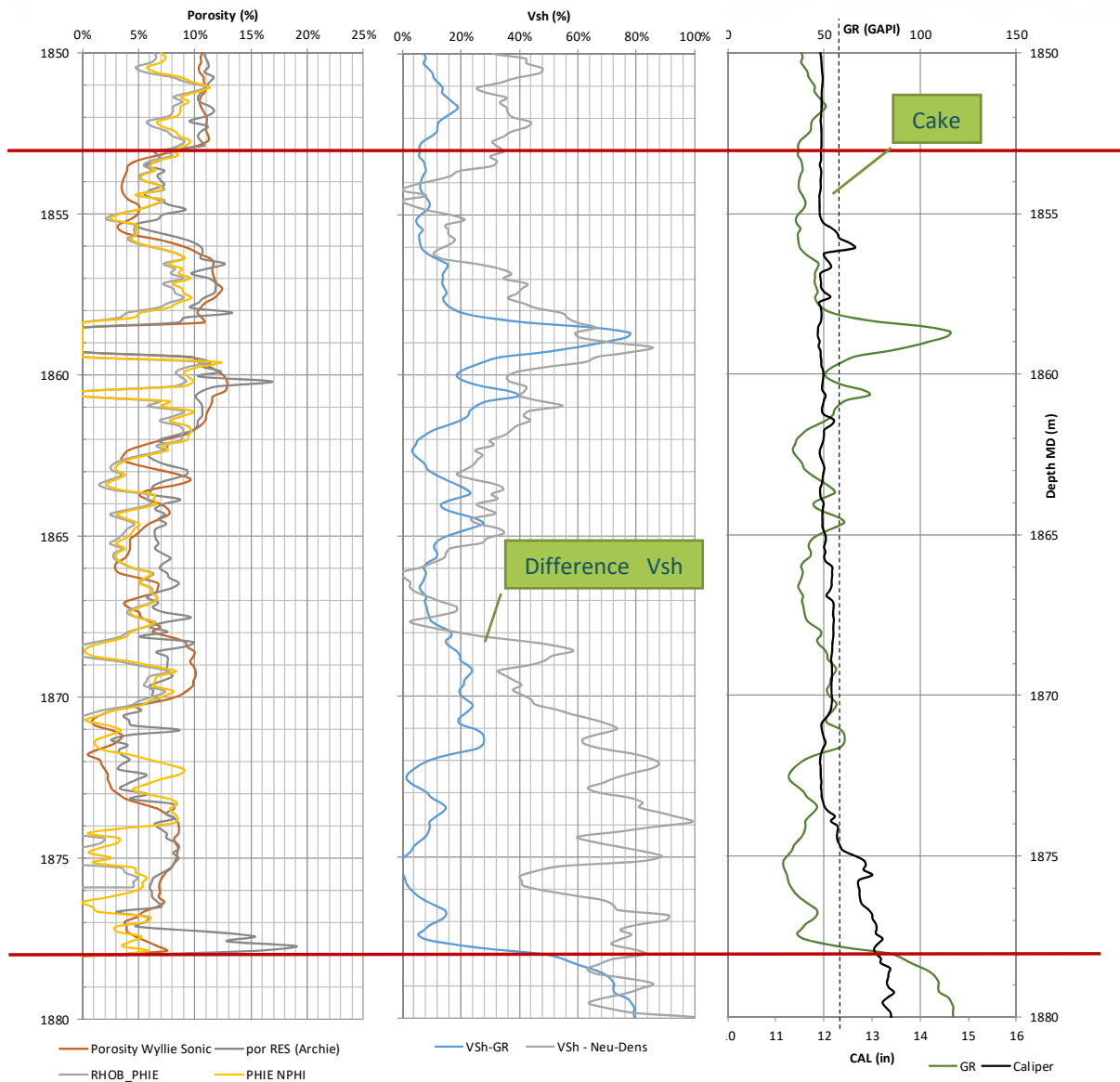


Figure 9-53 Ebro-1 data analysis versus depth, different Porosity curves on the left, the Vsh can be significant at the bottom of this formation although it is not recorded with the GR-Index. Caliper Data shows some cake, which may indicate porous formation (bit diameter = dash line).

The porosities calculated by different methods gives some discrepancies, as we have seen. Wyllie DT related equations gives slightly smaller porosities, in Ebro-2 this difference is remarkable (Sonic log settings?). RHOB (Density) and NPHI (Porosity) curves could be more reliable than other data, although are not always included in the set of logs run in these wells.

To summarized see the next table with the available calculated data:

Buntsandstein Conglomerates	PHIE-N/D Ebro-1	PHIE-N/D Ebro-2	Wyllie-DT Caspe-1	Wyllie-DT Fraga-1	Wyllie-DT Ballobar-1
median	5.23%	6.71%	9.41%	11.09%	2.98%
Average	5.35%	6.04%	10.18%	10.20%	2.67%
Standard Deviation	0.03	0.03	0.04	0.04	0.015

P10	1.35%	1.30%	6.04%	5.45%	0.00%
p50	5.23%	6.71%	9.41%	11.09%	2.98%
p90	9.09%	8.95%	15.80%	14.58%	4.40%

The next table summarize the Vsh values, Ebro-1 and Ebro-2 shows Vsh with two different methods.

Buntsandstein Conglomerates	Vsh-N/D Ebro-1	Vsh-GRI Ebro-1	Vsh-N/D Ebro-2	Vsh-GRI Ebro-2	Vsh-GRI Caspe-1	Vsh-GRI Fraga-1	Vsh-GRI Ballobar-1
median	41.26%	13.61%	18.87%	19.10%	3.31%	5.42%	61.46%
Average	44.58%	16.51%	24.81%	24.80%	4.90%	7.58%	50.15%
Standard Deviation	0.26	0.14	0.20	0.16	0.09	0.07	0.23
P10	10.52%	4.39%	5.14%	10.27%	0.00%	1.10%	14.60%
p50	41.26%	13.61%	18.87%	19.10%	3.31%	5.42%	61.46%
p90	80.97%	28.99%	60.80%	56.24%	7.15%	20.33%	73.55%

Buntsandstein sandstones (B1)

This formation presents a quite homogeneous logs signature; it could be defined as a large sequence of sandstones with rare shale intercalations. At the top the resistivity and Vsh increase and Slowness (DT) decrease. Slowness and density show some peaks that could indicate more cemented sandstones (Figure 9-54).

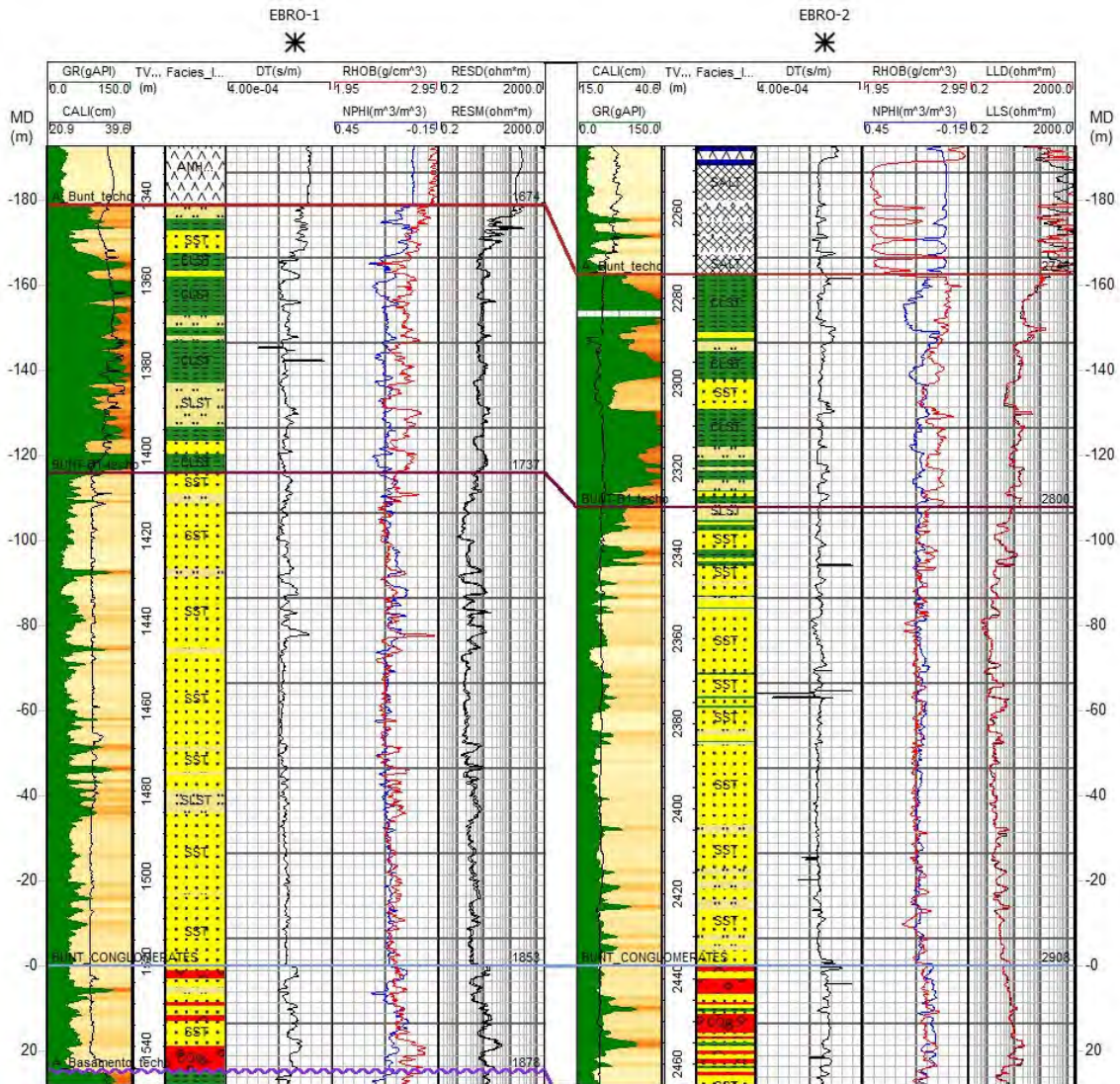


Figure 9-54 Ebro1 and Ebro-2 suite of wireline logs. Buntsandstein B1 formation appears to be fairly homogeneous. The top formation, B2, is much more argillaceous and presents some thick sandy intercalations.

At the time of writing we are awaiting permeability analysis on new samples. No permeabilities were analysed in this report.

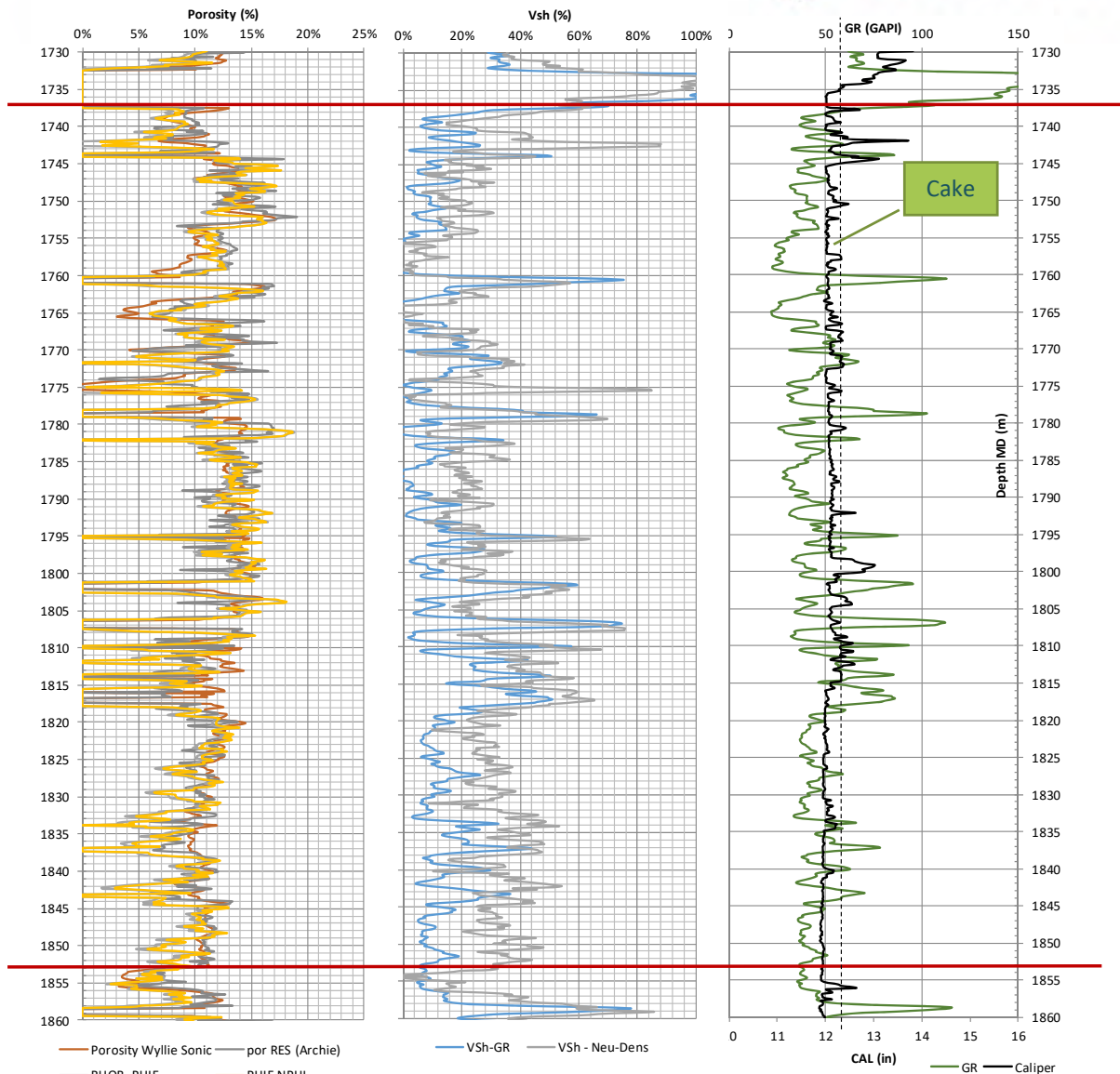


Figure 9-55 Ebro-1 B1 formation data analysis versus depth (MD in meters-vertical axis), porosities (in percentage, left), Vsh (in percentage, middle) and GR-Caliper (right, bit diameter = dash line).

In the Ebro-1 borehole, porosities seem to increase from bottom to top, on contrary Vsh values decrease (Figure 9-55). The bottom section shows a small discrepancy between Vsh values from GR-Index and Neutron-Density calculations. For some reason in the Ebro-2 porosity calculation from slowness continue giving smaller values than the other methods (difference in sonic tool settings?). Nevertheless, the Net to Gross ratio for this formation is very high (more than 0.88), considering only sandstones versus shales facies.

Below the available calculated porosity calculations from nearby wells.

Buntsandstein B1	PHIE-N/D Ebro-1	PHIE-N/D Ebro-2	Wyllie-DT Caspe-1	Wyllie-DT Fraga-1	Wyllie-DT Ballobar-1
median	10.93%	11.87%	22.75%	16.78%	10.22%
Average	10.69%	11.23%	22.37%	15.90%	9.76%

Standard Deviation	0.03	0.03	0.03	0.032	0.03
P10	6.08%	7.21%	18.73%	12.46%	5.15%
P50	10.93%	11.87%	22.75%	16.78%	10.22%
P90	14.90%	14.09%	25.74%	18.79%	13.52%

Next table shows Vsh values, NPHI/RHOB gives bigger Vsh values than GRindex in the lower section of this formation (Figure 9-55).

Buntsandstein B1	Vsh-N/D Ebro-1	Vsh GRi Ebro-1	Vsh-N/D Ebro-2	Vsh GRi Ebro-2	Vsh GRi Caspe-1	Vsh GRi Fraga-1	Vsh GRi Ballobar-1
median	26.51%	11.06%	24.76%	12.90%	5.01%	9.79%	6.38%
Average	28.72%	15.02%	26.52%	16.45%	7.19%	15.33%	11.71%
Standard Deviation	0.15	0.14	0.14	0.13	0.09	0.17	0.16
P10	10.21%	1.31%	11.06%	5.57%	0.00%	0.00%	0.00%
P50	26.51%	11.06%	24.76%	12.90%	5.01%	9.79%	6.38%
P90	48.51%	33.14%	43.57%	31.18%	15.82%	40.15%	32.77%

Buntsandstein Sandstones and Shales (B2)

This formation overlays the main reservoir. It consists of a very argillaceous formation with some sandstones interbedding.

In terms of logging data (Figure 9-56) this formation shows the usual high GR values in general with some low values corresponding to sandstone/siltstone lithologies. Compared with B1 formation it displays an increase in resistivities and density. Slowness logs show little to no change. There may be well washouts, due to the shaly levels collapse.

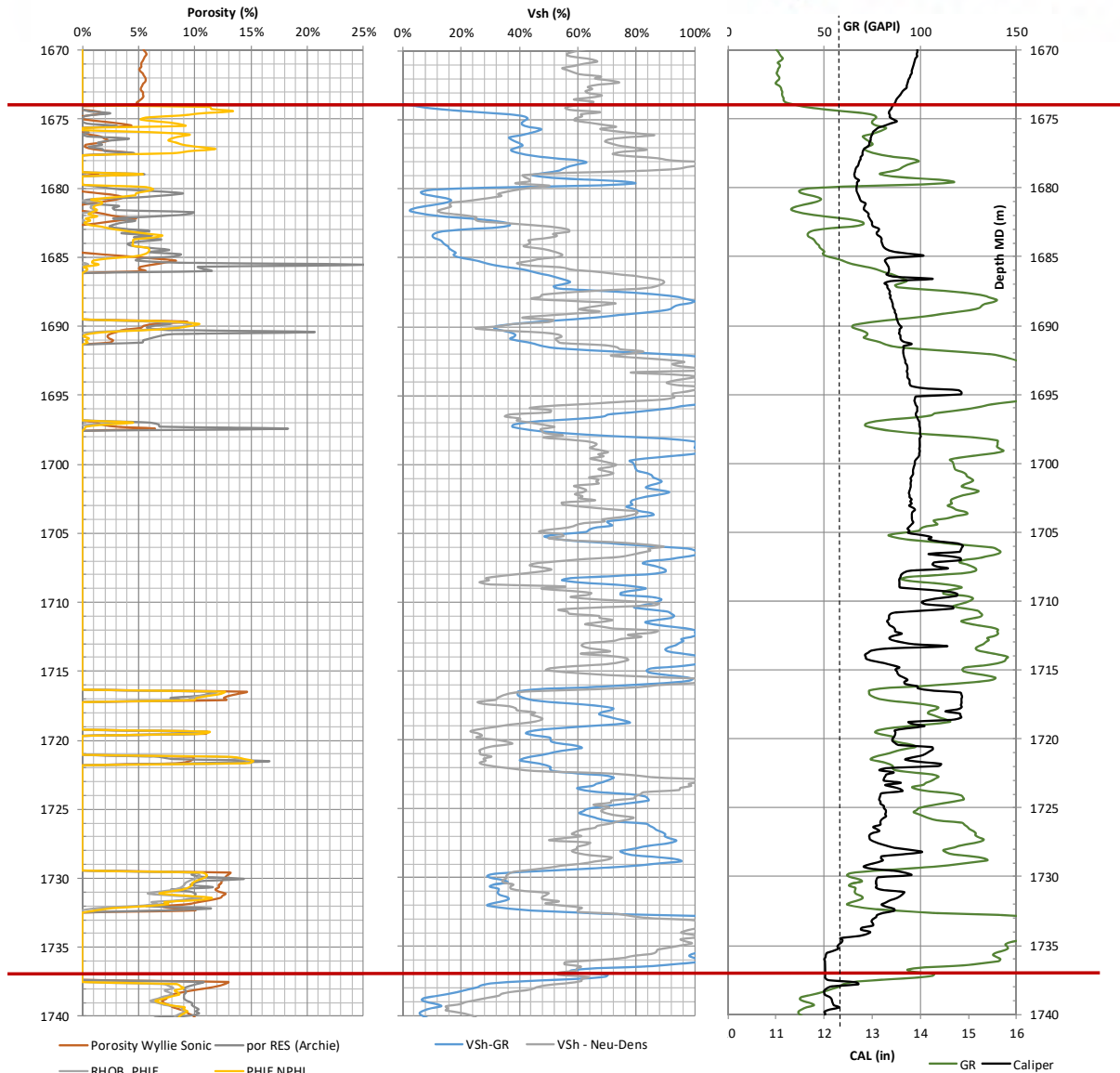


Figure 9-56 Ebro-1 data analysis versus depth, porosities (left), Vsh (middle) and GR-Caliper (right, bit diameter = dash line) for B2 formation.

The sandy levels could present certain porosity but the Net to Gross ratio of this formation is very low in general. The following table on shows calculated porosities in sandstones, very argillaceous though:

Buntsandstein B2	PHIE-N/D Ebro-1	PHIE-N/D Ebro-2	Wyllie-DT Caspe-1	Wyllie-DT Fraga-1	Wyllie-DT Ballobar-1
median	5.78%	7.08%	19.33%	9.28%	0.81%
Average	5.84%	6.24%	19.62%	10.24%	2.74%
Standard Deviation	0.04	0.03	0.06	0.06	0.04
P10	0.30%	1.19%	12.99%	2.23%	0.02%
p50	5.78%	7.08%	19.33%	9.28%	0.81%
p90	11.29%	9.71%	26.27%	19.36%	10.78%

Next table list the Vsh calculations for B2 formation, it is clearly a very argillaceous formation and the figures are very consistent.

Buntsandstein B2	Vsh N/D Ebro-1	Vsh GRi Ebro-1	Vsh N/D Ebro-2	Vsh GRi Ebro-2	Vsh GRi Caspe-1	Vsh GRi Fraga-1	Vsh GRi Ballobar-1
median	61.23%	71.43%	73.20%	75.09%	69.09%	81.36%	92.04%
Average	61.44%	66.86%	69.79%	68.79%	60.33%	72.37%	81.87%
Standard Deviation	0.21	0.27	0.27	0.27	0.32	0.25	0.22
P10	33.31%	30.81%	32.78%	31.32%	11.56%	34.01%	47.66%
p50	61.23%	71.43%	73.20%	75.09%	69.09%	81.36%	92.04%
p90	92.38%	100.00%	100.00%	100.00%	89.30%	100.00%	100.00%

Muschelkalk M1 & M3

Since the target of this report was to study firstly the Buntsandstein reservoir facies, the Muschelkalk formation has been analysed in a quick fashion. The Muschelkalk in this area has been divided in three members in the bibliography, called M1, M2 and M3 (from bottom to top). M1 and M3 are thick dolomitic formations with some intercalations of anhydrites or salts, and/or marls/limestones (Figure 9-57).

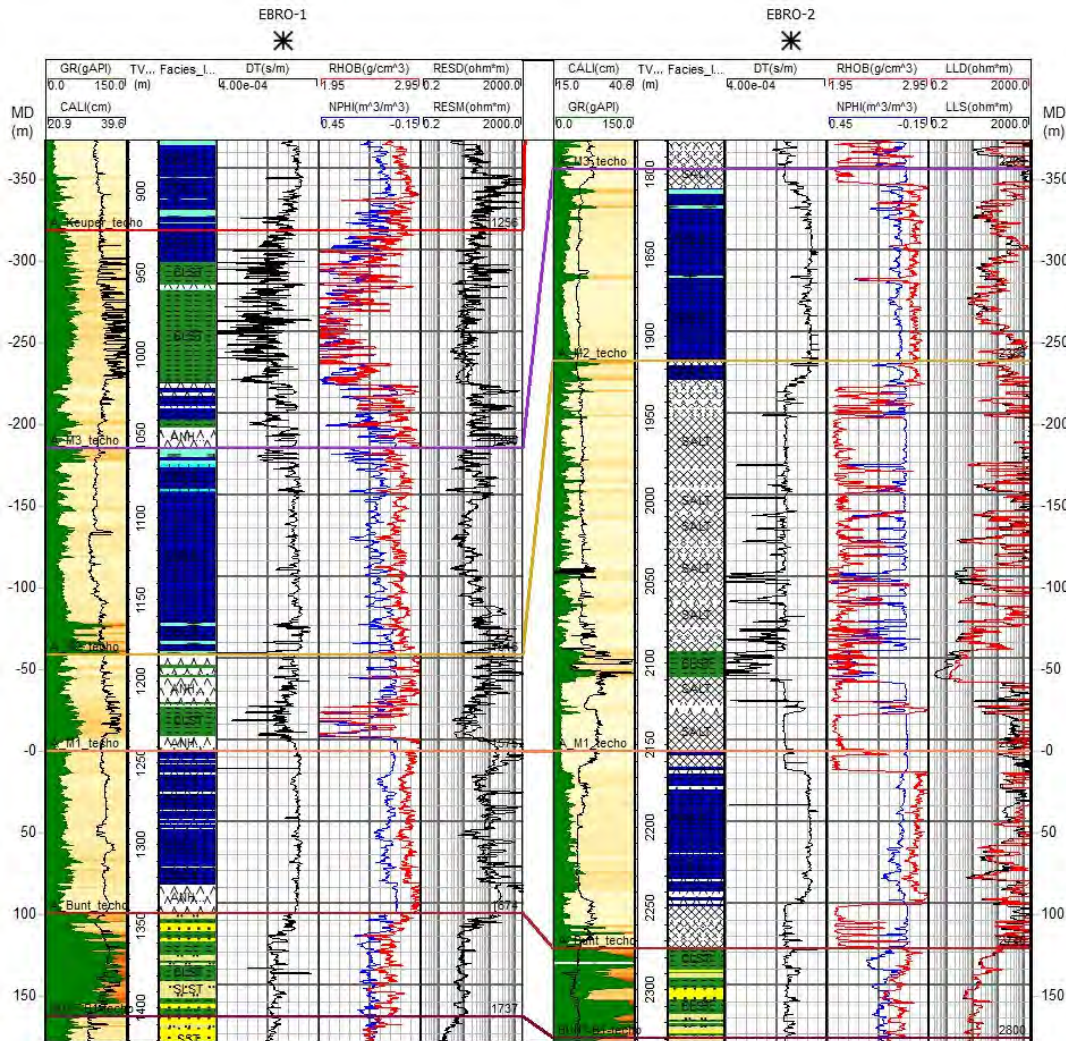


Figure 9-57 Ebro-1 and Ebro-2 wireline logs in Muschelkalk formation, M1 and M3 are dolomitic in general with some caved zones, M2 is clearly an evaporitic level that presents big thickness variations.

Mud losses are commonly reported at the base of the M3 formation during drilling, indicating that these formations have some effective porosity, most likely linked to fractures.

Plotting NPHI/RHOB (Neutron Porosity/Bulk Density) data it is apparent the presence of anhydrites, and in the case of Ebro-2 presence of salts (Figure 9-58).

The porosities on these formations vary depending on the petrophysical method applied. There are two factors that could interfere the calculations: presence of anhydrites (or even salts) and the enlarged well diameters that could affect logging tools readings (Figure 9-58 and Figure 9-59).

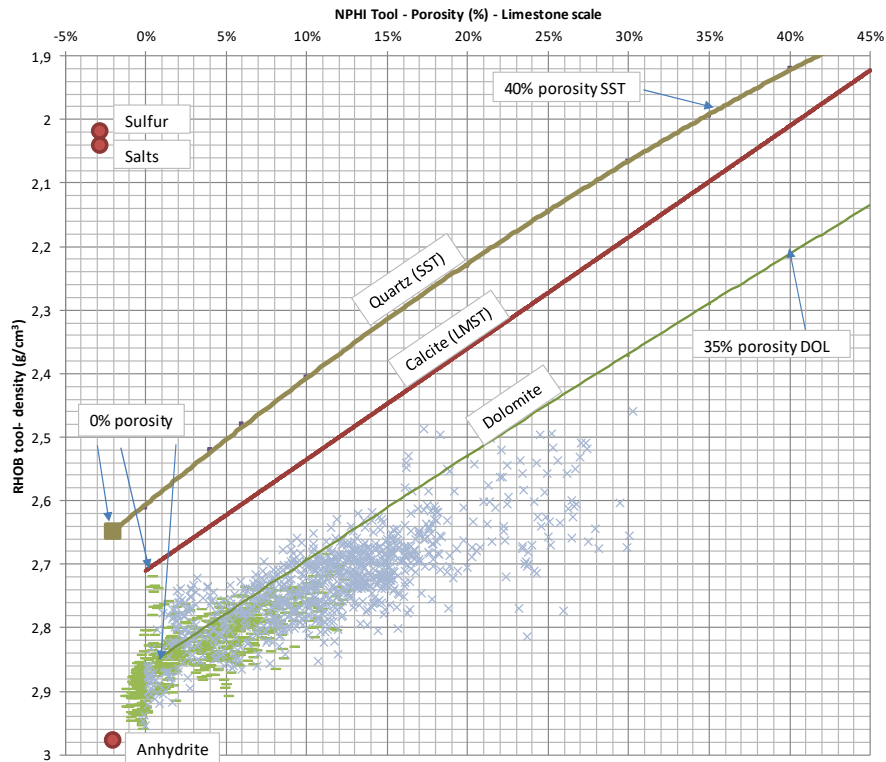


Figure 9-58 Ebro-1 Porosity-density cross-plot for M1 & M3 formations (M1 green dashes and M2 blue crosses). These two points-clouds are shifted to the lower left corner were anhydrites are usually plotted (modified from Schlumberger, 2009).

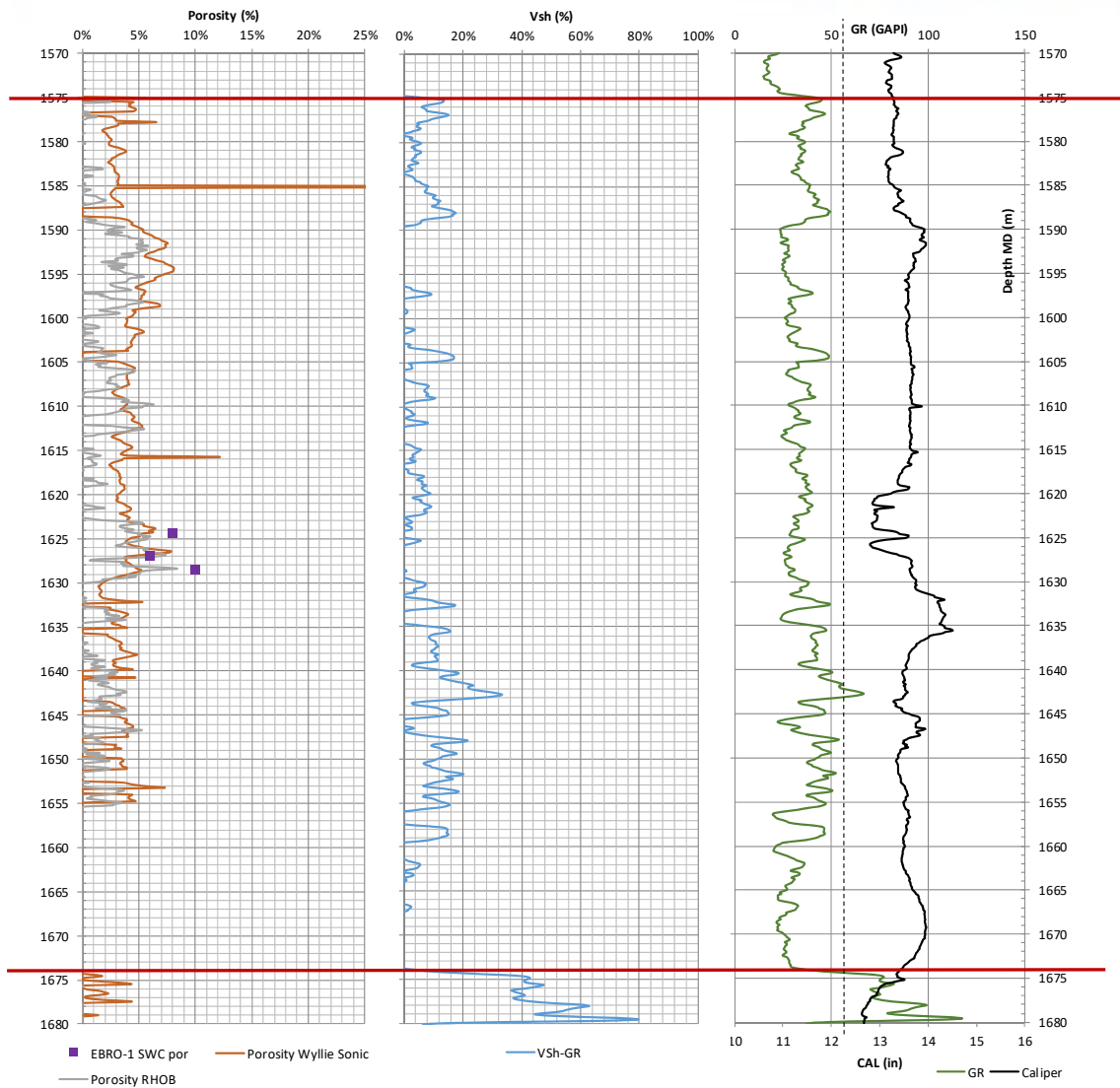


Figure 9-59 Left: Dolomites porosities versus depth in the Ebro-1 well obtained from Slowness and Bulk density logs. Middle Vsh calculated with GR-index. Right: GR and Caliper data, the bit diameter in this well section is 12 ¾ inches (dashed line). Three points in the chart mark the porosities of 3 side wall cores (SWC) samples that were reported in Ebro-1 Final Report. The next table synthetizes the porosity calculations for these two formations, but only in the Ebro-1 well, which is closer to the area of interest than Ebro-2:

	MUSCHELKALK M1 (Ebro-1)		MUSCHELKALK M3 (Ebro-1)	
	DT-Wyllie (Dolomite)	RHOB (Dolomite)	DT-Wyllie (Dolomite)	RHOB (Dolomite)
median	3.88%	2.21%	5.83%	5.91%
Average	4.12%	2.42%	6.21%	6.04%
S-Deviation	0.0295	0.0172	0.0310	0.0393
P10	2.52%	0.29%	3.14%	0.87%
p50	3.88%	2.21%	5.83%	5.91%
p90	6.02%	4.99%	9.76%	10.33%

Muschelkalk M2

This formation is located in between M1 and M3, it consists of anhydrites, salts and shales. It is considered to be a seal formation. The log data indicates that this formation tends to collapse and create large washouts (see caliper logs) which obviously affects the logging quality (Figure 9-57).

Keuper

This is the main seal formation of the area. The formation shows large washouts as well.

In the Lopin-1 well, from bottom to top, there are shales with some thick levels of salts, thick level of shales with some thin anhydrites and finally anhydrites with some dolomitic intercalations (Figure 9-60).

According to different studies M2 and Keuper play as detachment levels in the geodynamic models of the basin (see references cited in the geological introduction).

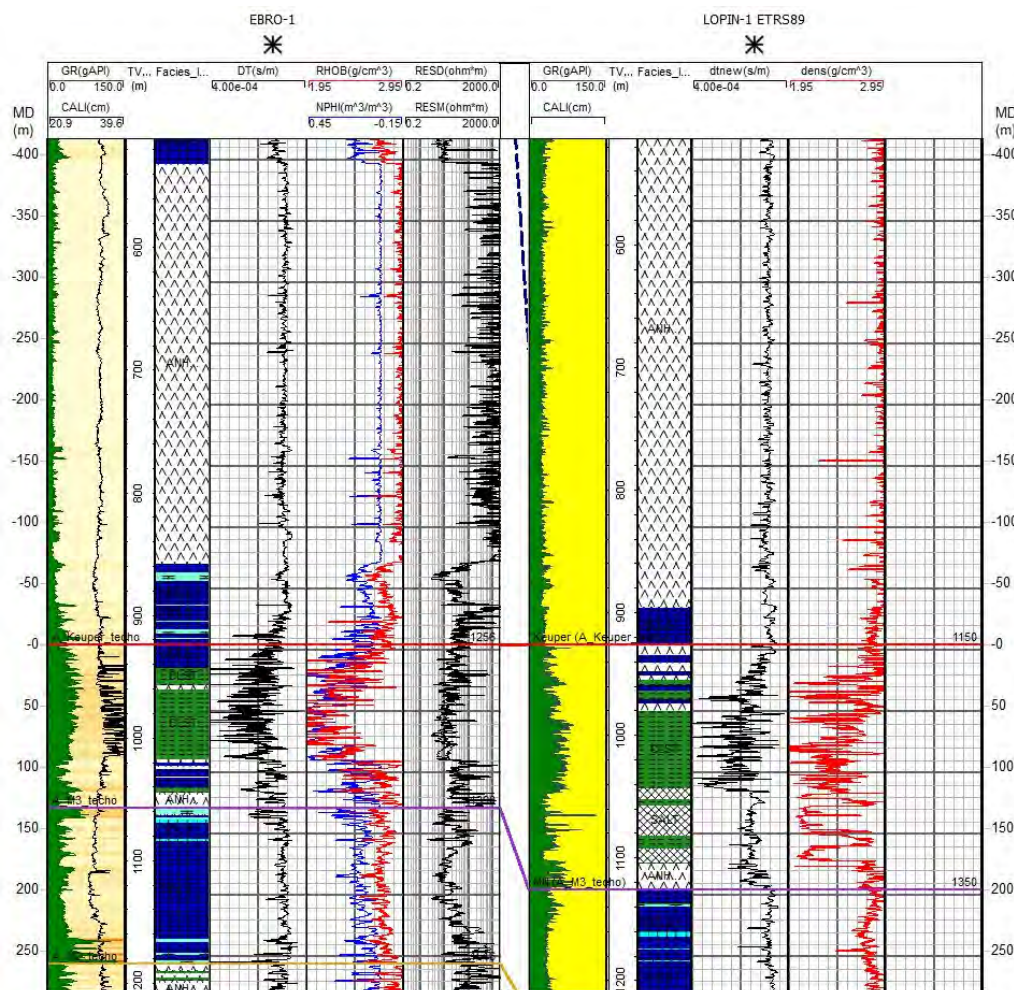


Figure 9-60 Keuper formation in Ebro-1 and Lopin-1.

9.5 Well-Seismic stratigraphic correlation

The former wells in the basin are in general outside the area of interest. However, the correlations point out to useful trends in the reservoir geology (Figure 9-61).

Thickness analysis of Buntsandstein formations suggests basin filling up trends which could change from bottom to top. The interpolation of the TVT (Total Vertical Thickness) of the Conglomeratic facies points to a source area located to the SW of the basin (Figure 9-61). The B1 formation (main reservoir) TVT increases eastward, notably Caspe-1 and Ballobar-1 have a much thicker B1 formations than other wells. Fraga-1, located between these two last wells shows thinner B1. This difference in thickness could be due to sinsedimentary faults that separated these three eastern wells from the western area (Figure 9-61).

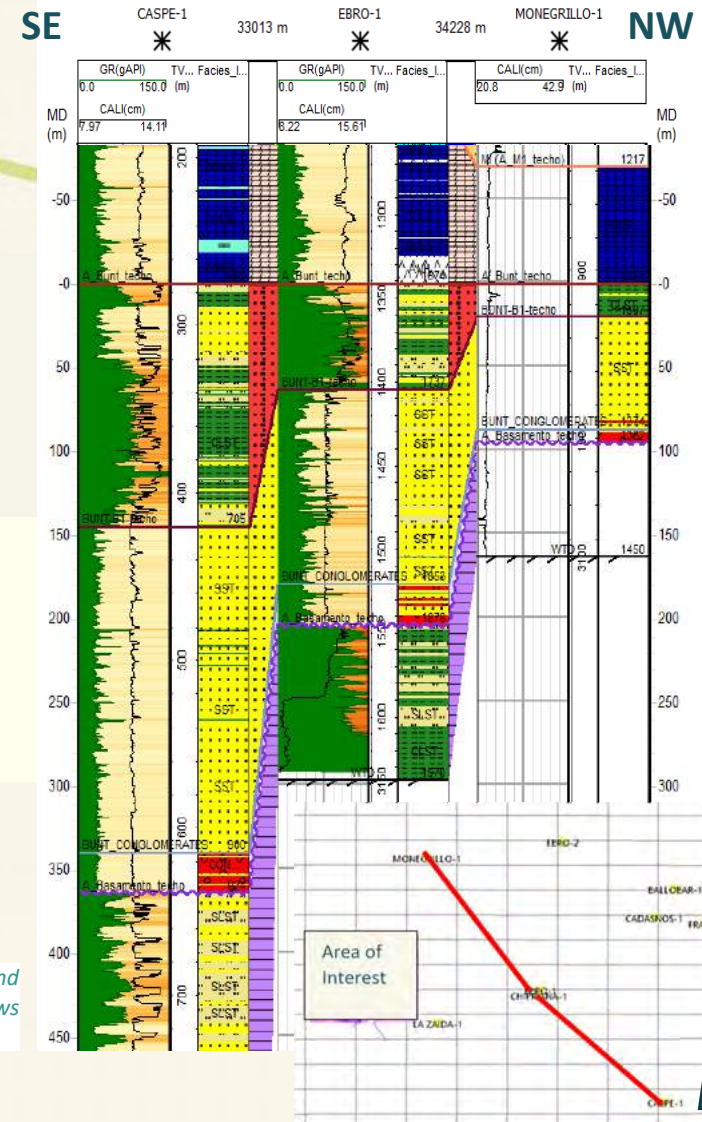
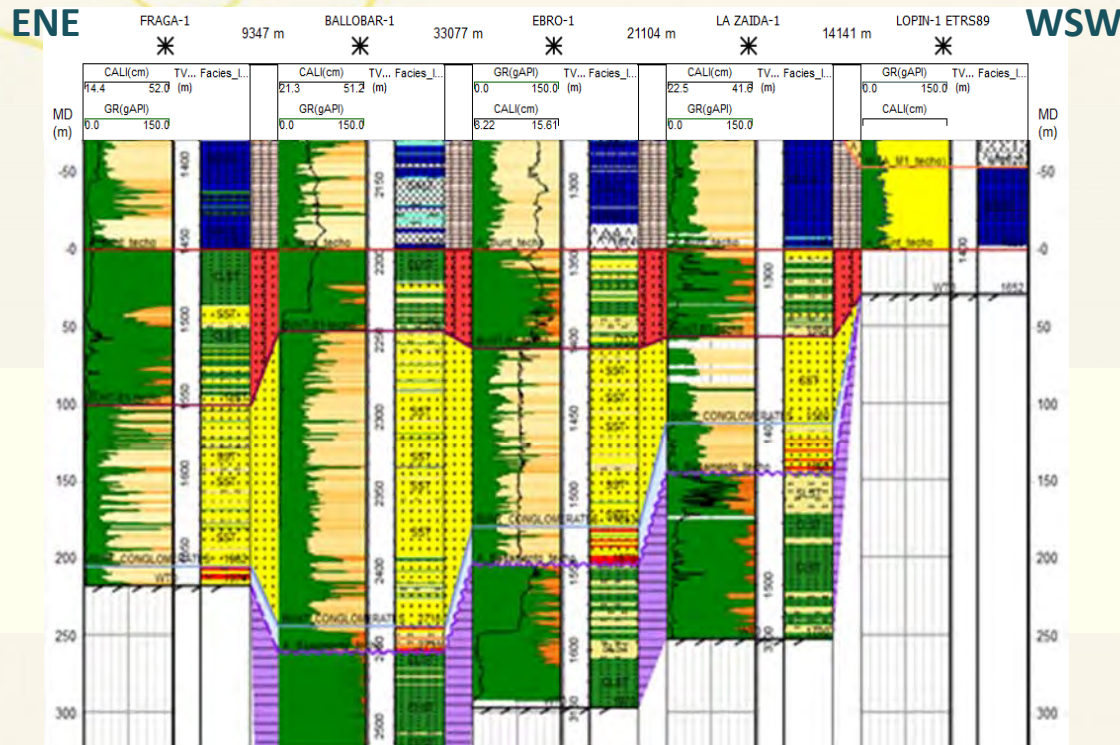


Figure 9-61 Formations correlation ENE-WSW and SE-NW, top of Buntsandstein flatten, note the increase in thickness to E and SE, as well as a slight increase in the Vsh (lower GR values) to the NE in the Buntsandstein formations (yellow). Caspe-1 shows a very thick Buntsandstein formation.

The PilotSTRATEGY project has received funding from the European Union's Horizon 2020 research and innovation programme under grant agreement No. 101022664



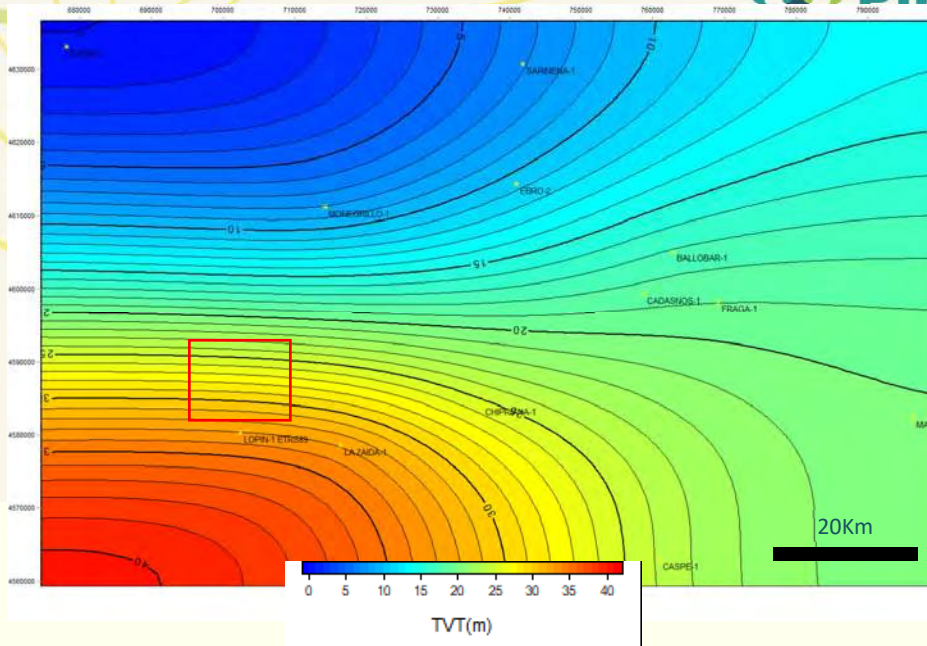


Figure 9-62 Buntsandstein conglomerates thickness interpolated (Discrete-Smooth-Interpolation-DSI).

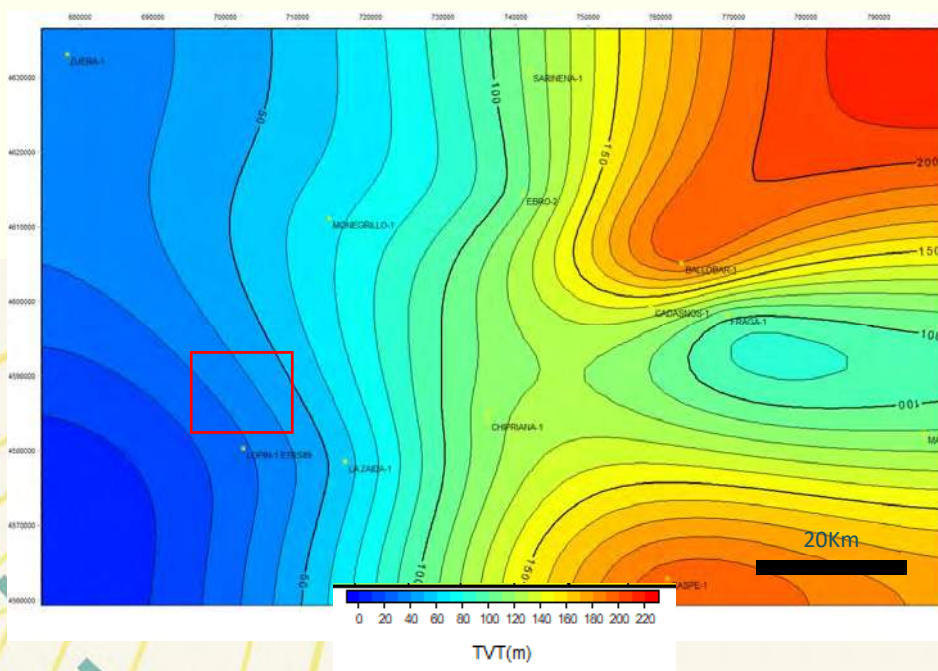


Figure 9-63 B1 TVT interpolated using Discrete-Smooth-Interpolation (DSI). The Buntsandstein thickness in this area increases slightly eastwards, but the eastern-most wells show huge increases.

The Net to Gross index in the B1 formation gives very high values (about 0.75 sandstones with porosities bigger than 8%). It shows a trend to less sandy formations towards the NE.

The B2 formation shows a much more complex thickness distribution, which may be linked to the paleo-geography (?) (Figure 9-64). The Net to gross shows an eastward trend, but the values are very low.

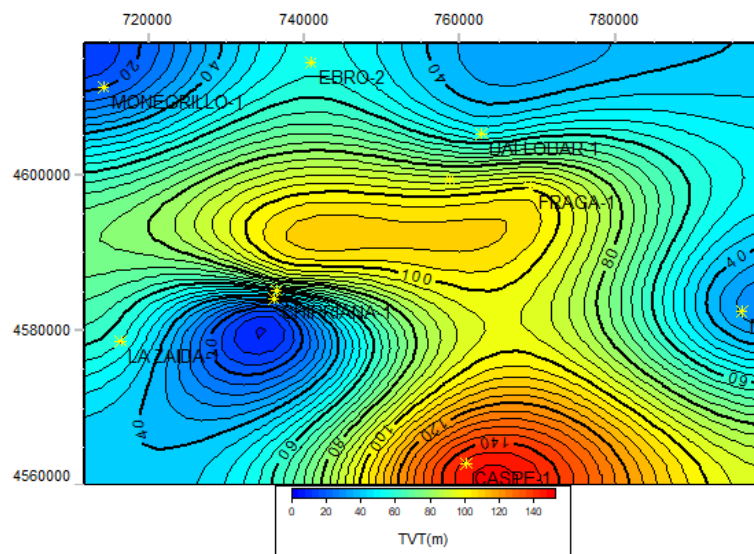


Figure 9-64 B2 TVT values interpolated, the distribution is much more complex than the other Buntsandstein formations.

9.6 Time-Depth Conversion

The interpretation of the horizons and the faults has been carried out on the existing 2D seismic profiles of previous exploration surveys. These profiles are part of the geophysical data repository hosted by IGME and they were scanned from the original documents and vectorized in SEGY format. Both the fault lines and the horizons have been drawn using the SKUA-GOCAD tools.

Prior to the geological interpretation, the conversion from time to depth was made. There are no deep wells in the area of interest. The closest one is the Lopín-1 well, which is located to the south, outside the area initially considered, so the study area was expanded to include it, as well as the seismic sections nearby. The main difficulty found is that the information of the geophysical data of the well is incomplete, so the calibration in time with the seismic profiles was not possible.

The conversion was done following a workflow consisting of transposing the average velocity data used in the seismic image processing, which appear in the scanned profiles, to a matrix of velocity as a function of depth on a time scale (Figure 9-65). These matrices were then transformed to a column format and the coordinates of each point, taken from the seismic line traces, were added. In SKUA-GOCAD these matrices of values were imported into curves with the velocity values and velocity functions were created. The velocity of each velocity function was transferred as an attribute to each seismic profile and an interpolation was applied using the median value, thus avoiding abrupt changes in velocity. Finally, the depth conversion of each seismic profile was performed using the interpolated mean velocity values (Figure 9-66).

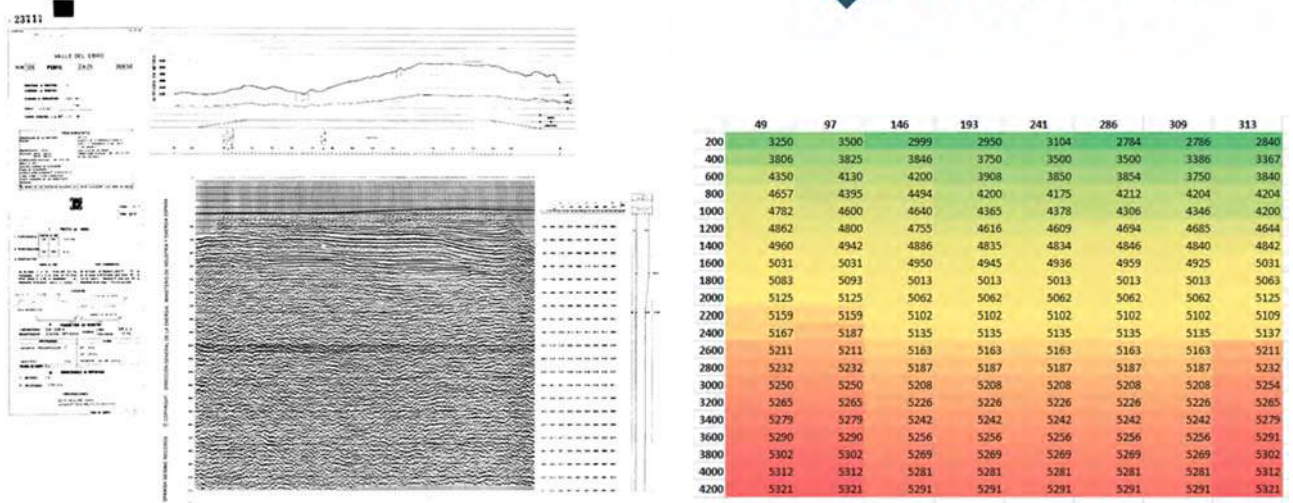


Figure 9-65 Example of one original seismic profile (left) and the velocities matrix extracted from the data on the image (right).

To test the validity of the method, the entire process was carried out on the ZA-25 profile, located close to the Lopín-1 well, and the correspondence between the well markers and the seismic reflectors was checked.

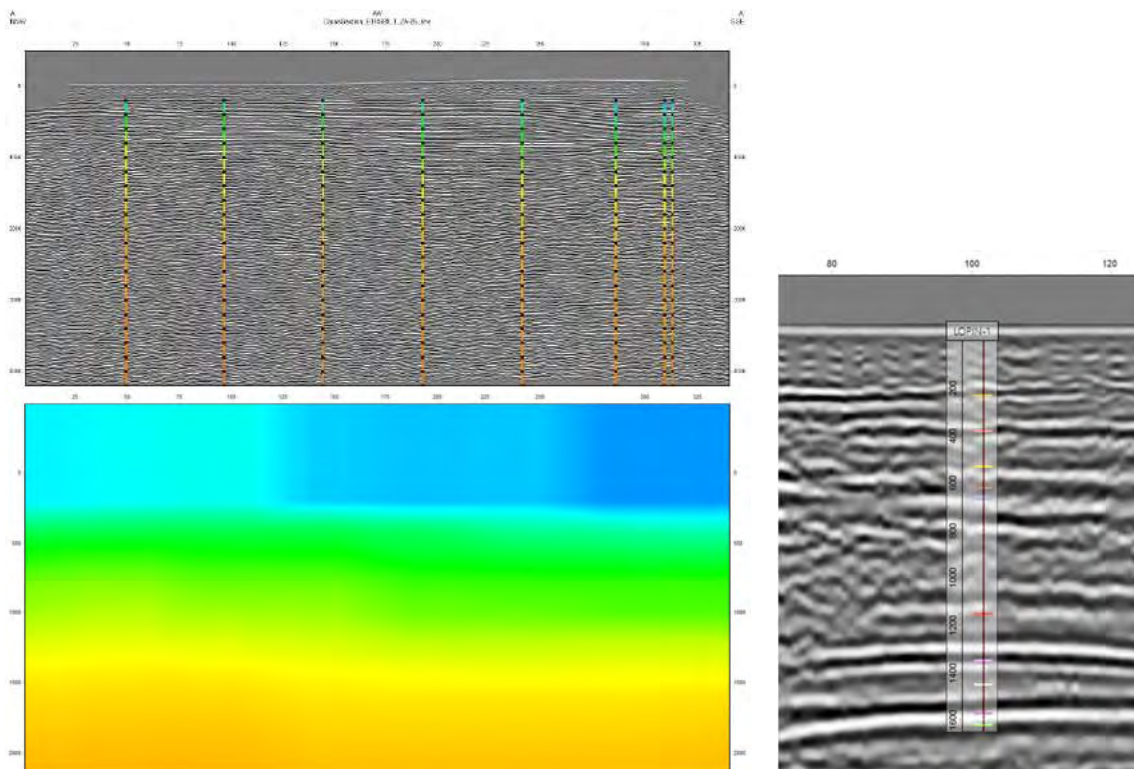


Figure 9-66 Velocity curves over the seismic profile (top left) and the velocities property interpolated (bottom left). On the right, detail of the seismic profile converted from time to depth and the Lopín-1 well with horizon markers in real depth to test the conversion.

9.7 Reservoir Facies

9.7.1 Stratigraphy

The detailed stratigraphy analysis has been carried out from the study of outcrops of the Iberian Range and the Chiprana-1 borehole core.

Triassic series lie unconformably on the Permian deposits or about the Paleozoic basement (Figure 9-67). The initial of the Triassic rifting can be observed by the syn-sedimentary faults that generates depocenters in the Triassic terrigenous units.



Figure 9-67 . Unconformity between the Buntsandstein Facies and the Hercynian basement. Terrigenous facies at the bottom of the Buntsandstein onlap on a Paleozoic paleorelief and synsedimentary faults. Montalban Anticline area (Aragonese Branch of the Iberian Range) ca. 5 km from Peñas Royas.

The Permian unit is a series of polymictic conglomerates (Figure 9-69a), very abundant in sub-angular Paleozoic quartzites and with some sand intercalations, which are structured in more or less horizontal strata from 0.5 to 2 m thick, quite well selected. Coarse sandy strata with cross-bedding may be interbedded. They are interpreted as gravel bars, from braided alluvial systems, in some cases passing laterally to sand bars.

The Triassic series is compounded of three Germanic facies: Buntsandstein, Muschelkalk and Keuper. The Buntsandstein facies has an average thickness of 100m. These facies is composed of the three formations: Aranda, Carcalejos and Rané (Figure 9-9). In this case, Aranda and Carcalejos formations correspond to units B-1 and B-2 respectively as they are usually named in the oil and gas industry in this area (Aurell et al., 2001. In the well logs analysis Rané formation is not defined, never the less B-2 unit gradually pass upwards to Rané formation. (Figure 9-68).

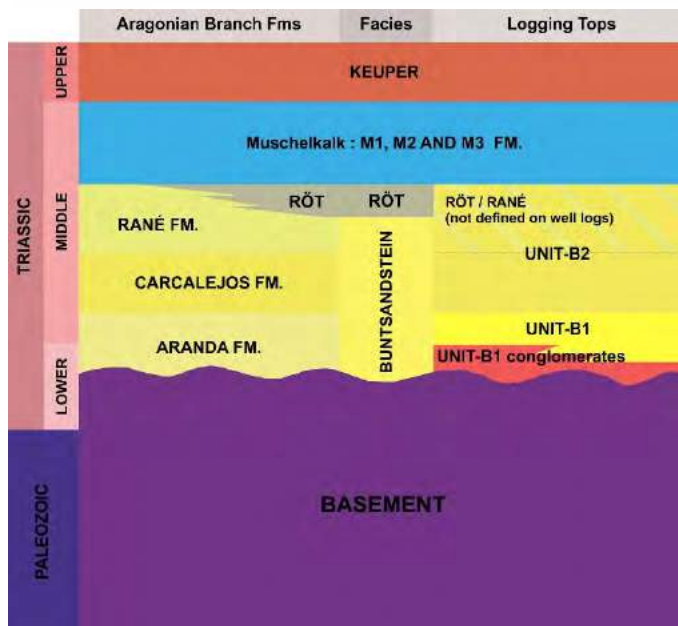


Figure 9-68. Correlation table between formations defined in this area and units set in this report, Triassic formations from Arche et al. 2004.

Unit B1

The lower section of the B1-Unit is recognised in the Montalban area (Iberian Range) by a succession of red to dark red conglomerate up to 1 to 5 m thickness. The conglomerate is matrix-supported and predominantly contains poorly rounded to subangular quartzite pebbles (Figure 9-69b). Lateral accretion conglomerates show cross-bedding with fining-upward cycles of the individual beds. Coarse sand layers occasionally mark the top of a cross-bed set. Medium to coarse-grained sand lenses of 0.1–0.5 m in thickness interfingers the breccia with variable frequency. Conglomerate have a smaller clast size of up to 4 cm and are limited to the bottom and top by

erosive surfaces.

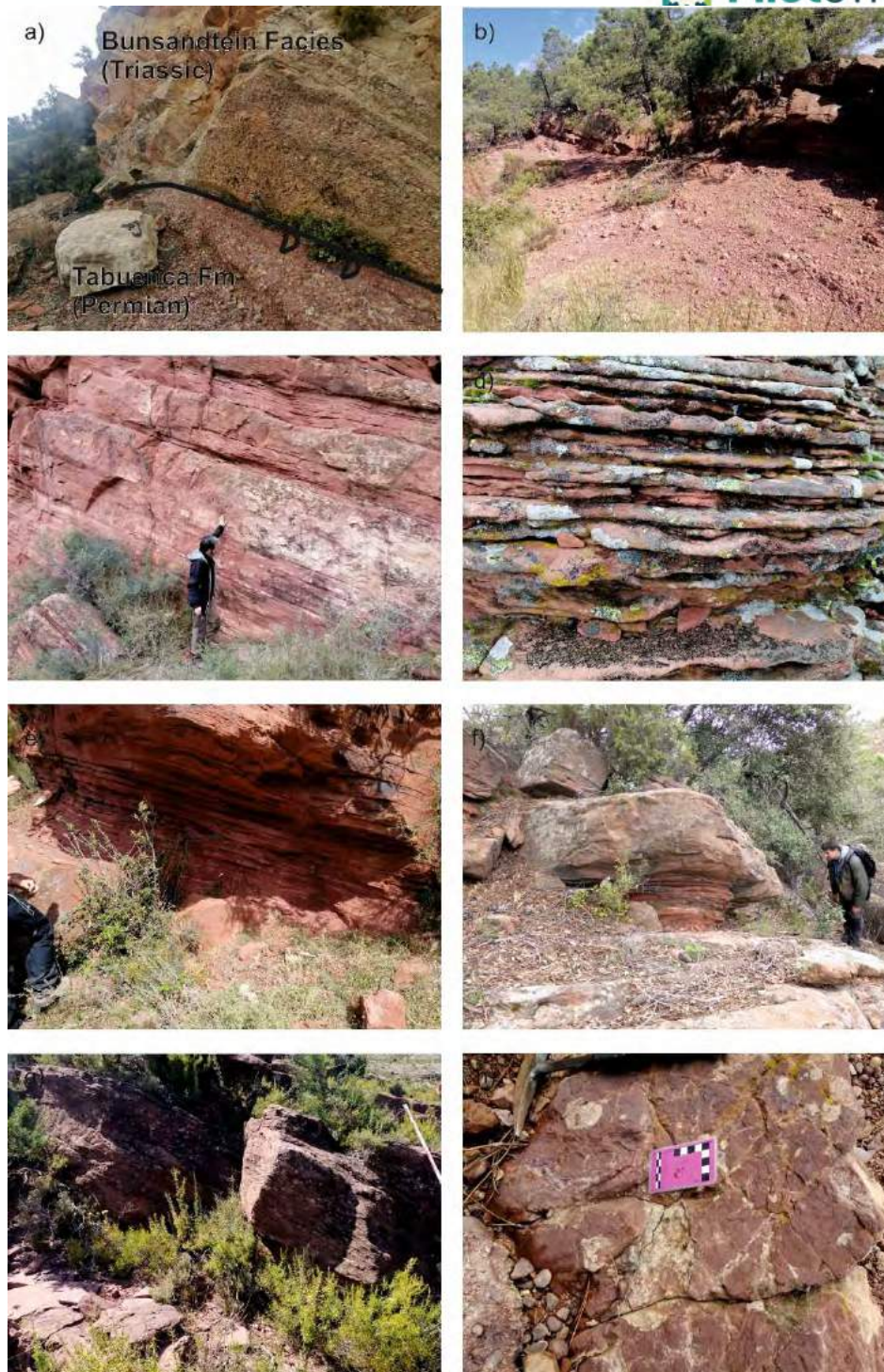


Figure 9-69 . a) Unconformity between the Permian conglomerate and the Buntsandstein facies with an immature paleosol; b) First level of Buntsandstein Facies with cross-bedding, Unit B1; c) Layers of ripples eroded by a cross-bedded sandstone strata, Unit B1; d) Interstratification of ripple, Unit B1s; e) Intercalation of sand layers that disappear laterally, slightly erosive, Unit B1; f) horizontal layer of sandstone with cross-bedded, Unit B1; g) Sandstone and pebbles with cross-bedding, Unit B2; h) Claystone and siltstone with carbonate nodules, Unit B2.

At the bottom and top of all wells and outcrops of Unit B1, red sandstones with grain and stratum decreasing trends are recognized, fining upwards from medium to fine grain size. The base is slightly channeled, with quartzite cobble lags, cross-trough bedding, and stream ripples (Figure 9-69b and c).

They are organized in tabular strata with an average thickness of 1.5 m. (Figure 9-70). Most of the sets are cross-trough bedding with clay chips and erosive base (Figure 9-72a and b).

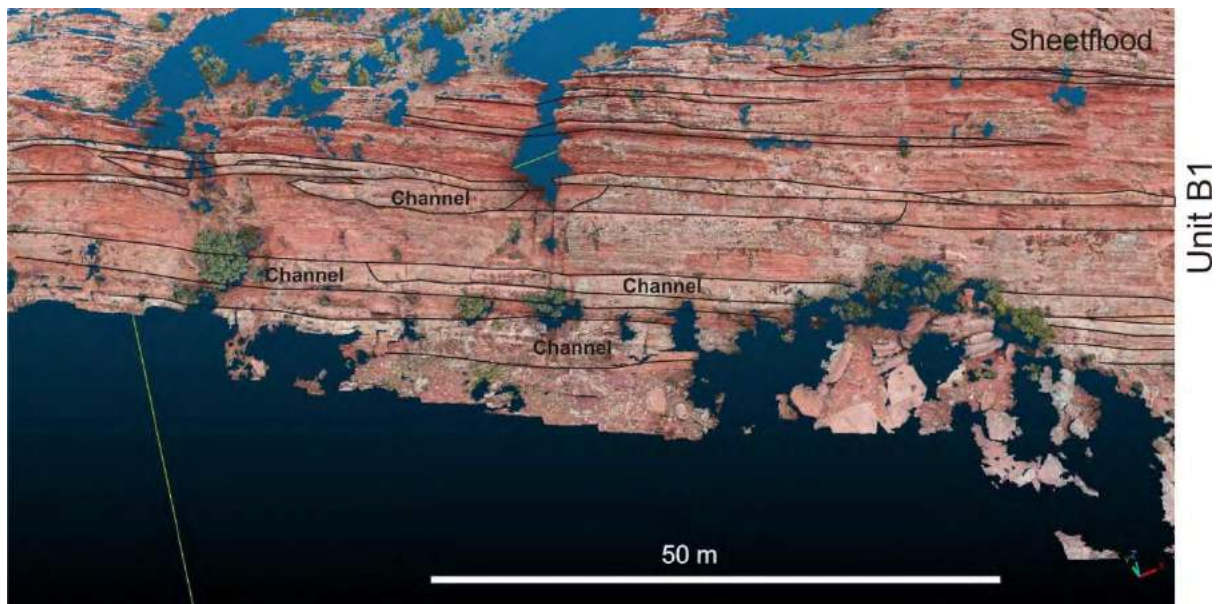


Figure 9-70 Drone generated photogrammetric model of Unit B1 in the Torre Arcas.

It is made-up of sub-rounded to sub-angular higher quartz contents, and lower feldspar and clay minerals contents and hematites coating (Figure 9-71a and c). Laterally and vertically passed to fine-grained red sandstones (Figure 9-71b and Figure 9-73). The strata are tabular with flat bottom and top. It is generated by an alternation of sets of 20-50 cm, mostly of planar cross-stratification, although, at the base, troughs are also observed. Oscillation ripples of combined flow appear at the top of the strata. Compositionally it is a subangular quartzarenite with hematite coating and quartz syntaxial cements (Figure 9-71b).

In the Chiprana-1 borehole, fine-grained green marly sandstones and marls can also be observed with a wavy lamination and current ripples (Figure 9-72c and d and Figure 9-73).

Unit B2

The boundary is marked by an increase in floodplain facies resulting in isolated sandstone beds and partly amalgamated complexes, but also single-storey bodies.

The section of this unit is recognised by tabular, sheetlike, pink to red sandstone bodies with a thickness ranging between 2 and 5 m and extending laterally for 100–200's of m, often beyond exposure. Several vertically and laterally stacking sand bodies, which erode into older units, often build the isolated sandbodies. Grain size ranges from medium to coarse sand with fining upward sequences within the individual bodies (Figure 9-71d and Figure 9-72d). The base often incorporates pebbles and cobbles up to 4 cm in diameter. Petrologically, a larger size of the sands can be observed. It is composed of monocrystalline quartz, muscovite is also very abundant.



Figure 9-71 Representative microphotographs of thin sections (parallel and crossed nicols). a) Cross-bedding sandstone, bottom of Unit B1; b) Interstratification of ripple; c) Cross-bedding sandstone, top of Unit B1; and d) Cross-bedding sandstone, top of Unit B2.

Alternating with the red sandstone bodies there is very fine sand to silt that separates the individual sand beds or amalgamated complexes and reach up to 20 m in thickness. These beds are dark red in colour, finely laminated and commonly include a high mica content. The top of these silts are frequently recognised by dark red to red muddy/silty palaeosols with calcretised rhizoliths, superficial

or very shallow trace fossils such as living burrows and feeding trails and dark red to medium grey colour mottling (Figure 9-69h and Figure 9-72e).



Figure 9-72 Chiprana borehole. a and b) Cross-bedding sandstone with clay chips to bottom of Unit B1; c and d) intervals of siltstone and very fine to fine grained sandstones, planar, ripple and wave-ripple laminations of the Unit 1B; e) silts with nodules of carbonate; f) Cross-bedding sandstone with clay chips to bottom of Unit B2.

Petrology of the Units B1 and B2.

The detrital mineralogy of Unit B1 is dominated by monocrystalline and polycrystalline quartz. Unit B1 samples are >75% quartz and are classified as quartzarenite. While in the detrital mineralogy the Unit B2 samples are mainly compound of monocristaline quartz and muscovite (Figure 9-71). Feldspar is the second most abundant detrital component and occurs almost exclusively as K-feldspar

Fe-oxide cements represent the major grain coating phases. On average, the three sample sets bear authigenic phases that include illite, syntaxial quartz overgrowths and kaolinite.

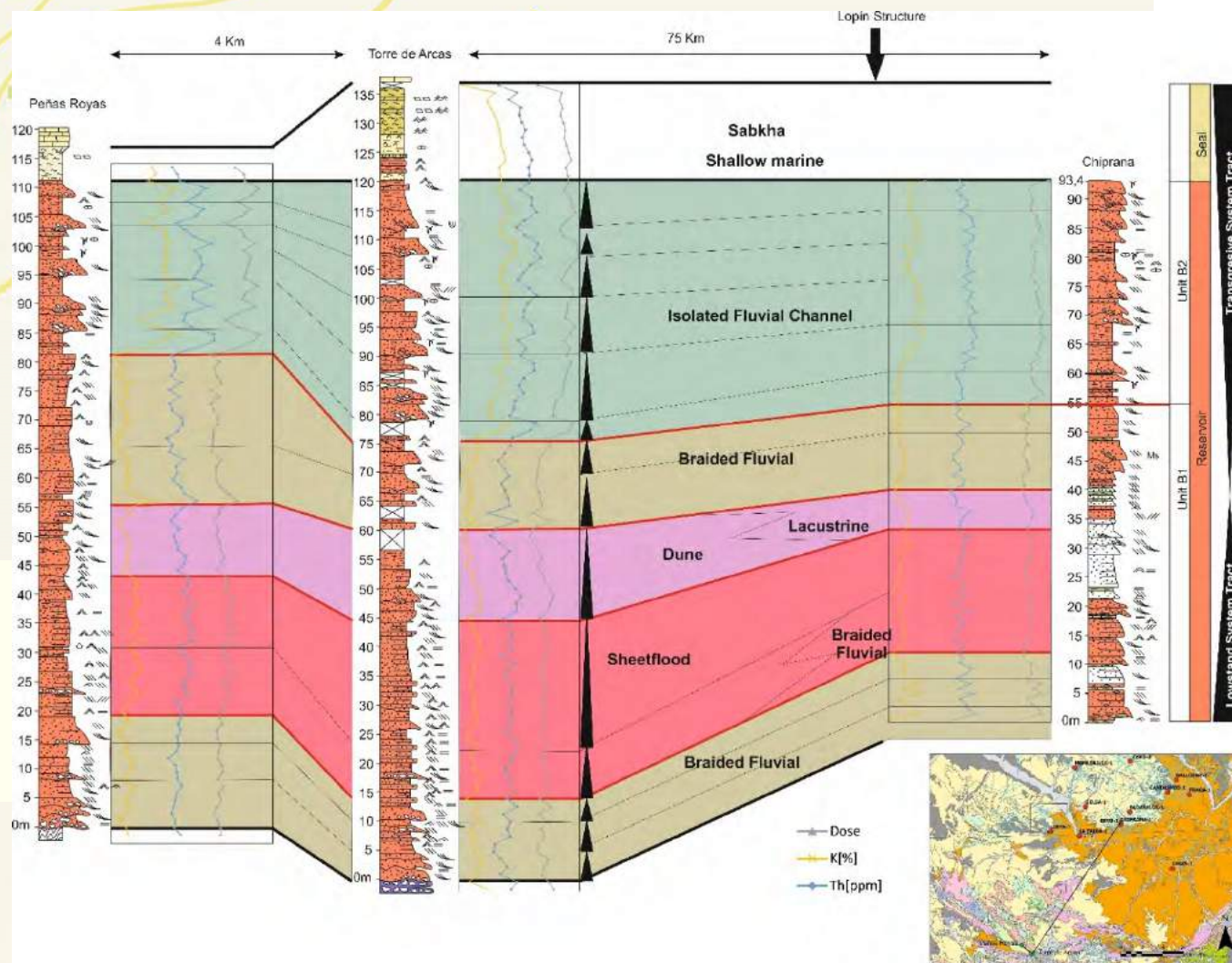


Figure 9-73 Stratigraphic correlation.

The PilotSTRATEGY project has received funding from the European Union's Horizon 2020 research and innovation programme under grant agreement No. 101022664



9.7.2 Reservoir Architecture

Reservoir architecture are constructed by field analogues (Montalbán area, to 50 km the southwest of Lopín structure) and Chiprana-1 borehole (to 20 Km the East from the structure) (Figure 9-74).

In general, the Buntsandstein Facies has fluvio-lacustrine origin, main sand fairways drained to the NE, with the main sediment supply to SW (Arche et al., 2004). The limit of SW of Iberian Ridge to these orientations there were palaeo-highs which control the drainage patterns. Finally, the entire basin was inundated by the Proto-Tethyan Sea from the E, resulting in the deposition of claystones and dolostones in a brackish to marine coastal plain, Rané and Muschelkalk Formations.

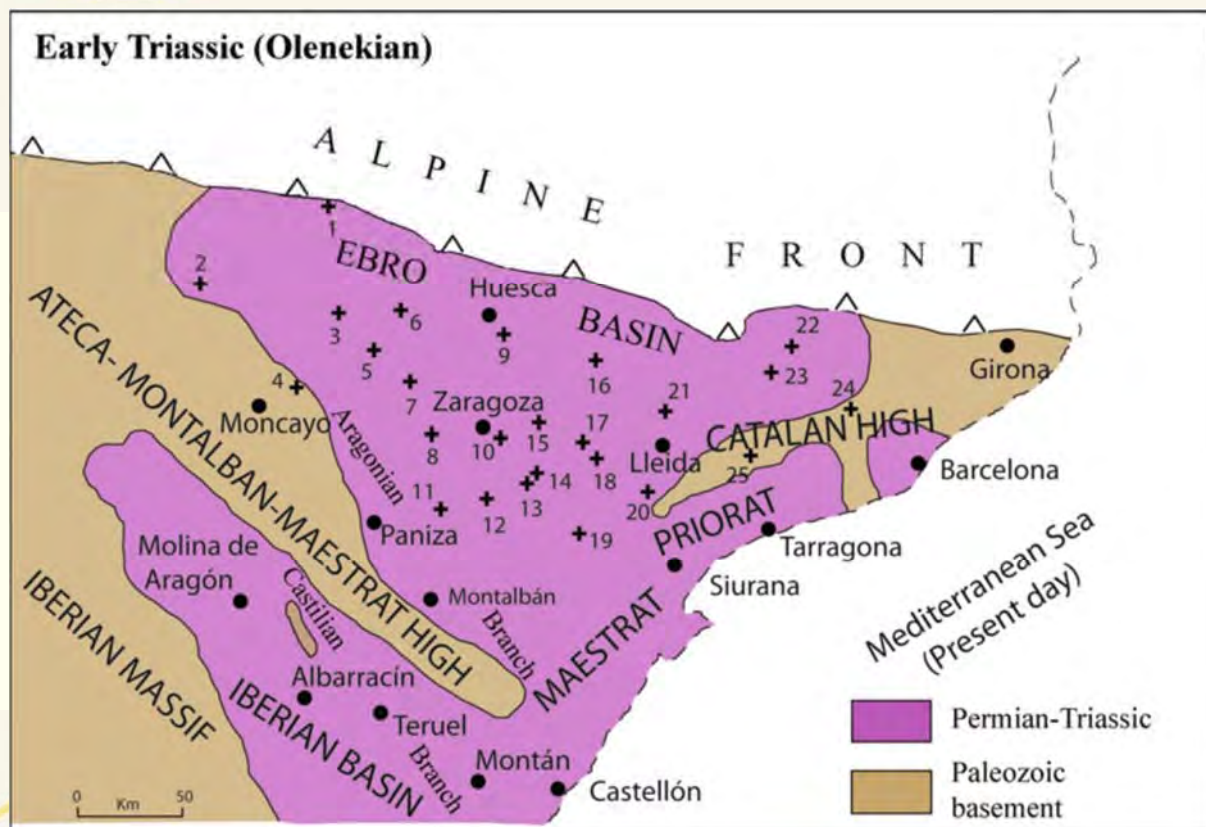


Figure 9-74 The Ebro Basin at the Olenekian, Early Triassic (Lopez et al., 2019).

The Unit B1 shows the internal channel stacking patterns and absence of preservation of significant amounts of mud in the system within this unit suggests little accommodation space availability and generally an overfilled basin state.

The high preservation of fine-grained lithologies of the Unit B2 can be explained by an increased subsidence rate creating abundant accommodation space favouring the deposition of floodplain, overbank and palaeosol fines.

Several depositional sequences are observed to go from coarse to fine grained from bottom to top (Figure 9-73).

9.7.3 Reservoir Properties

The optical porosity obtained is intergranular porosity and some secondary porosity from feldspars leaching. Porosity is mainly controlled by grain size (with a wide variability), clay content (conversely increase with grain size increase) and quartz cements presence (more quartz cements is related with

more porosity). Feldspars leaching can be also important. Porosity is, however, very variable producing strong vertical variations in porosity and permeability.

The kv/kh ratio is in general very low; the highest is located in the braided channel-fills (0.01). In contrast ephemeral channel-fills and sheetflood sandstones has kv/kh ratios of 0.001.

Sandbody continuity is bigger at the bottom and top of Unit B1. Upper sandbodies of the Unit B2 are more isolated which has along-channels linear flow. Sand bodies of the two units (B1 and B2) show the highest porosity values.

Samples	PS TA 1C	PS TA 2F	PS TA 6B	PS TA 7	PS TA 8	PS TA 9	PS TA 10A	PS TA 10B	PS TA 3F	PS TA 4B	PS TA 11	PS TA 5A	PS TA 12	PS TA 13C
Depth (m)	11	31	39	46	69	76	83	83.1	97	110	119	122	129	135
Sedimentary Feature	Trough X-Bedding	Ripple	Plannar X-Bedding	Trough X-Bedding	Plannar X-Bedding	Silt With nodules	Marls	Evaporites	Marls					
Facies	Channel	Bar	Bar	Dune	Crevasse	Bottom Channel	Channel	Channel	Channel	Bar	Paleosoil	Lake	Lake	Lake
Porosity (%)	13.48	10.80	7.87	15.26	12.40	13.39	17.81	19.39	10.84	6.85	7.90	9.82		5.21
Mineralogy														
Quartz	95.67	91.86	96.74	96.4	87.36	94.17	79.13	73.44	59.95	69.24	45.78	60.57	34.06	6.3
Phyllosilicates	2.17	5.94	1.82	3.18	11.53	3.4	9.36	12.95	3.71	8.74	31.39	8.44	34.97	4.85
Feldspars	1.73	1.26	1	0	0.57	1.24	10.04	11.94	35.61	12.36	8.45	9.01	12.79	3.18
Carbonates	0.14	0	0.04	0	0.05	0	0	0	0	8.17	6.49	21.82	12.69	85.58
Sulfates	0	0	0	0	0	0	0	0	0	0	0	0	0	0
Others	0.29	0.94	0.4	0.42	0.49	1.19	1.47	1.67	0.73	1.49	7.89	0.16	5.49	0.09
Total	100	100	100	100	100	100	100	100	100	100	100	100	100	100

TA samples are of the Torre Arcas outcrop.

The PilotSTRATEGY project has received funding from the European Union's Horizon 2020 research and innovation programme under grant agreement No. 101022664



Samples	PS PR 1	PS PR 2	PS PR 3	PS PR 4	PS PR 5	PS PR 6	PS PR 7	PS PR 8	PS PR 9	PS PR 11
Depth (m)	2	11.5	37	46	68.5	84	86	118	122.5	124
Sedimentary Feature	Trough X-Bedding	Plannar X-Bedding	Plannar X-Bedding	Trough X-Bedding	Trough X-Bedding	Silts with nodules	Trough X-Bedding	Trough X-Bedding	Marls	Carbonate
Facies	Channel	Bar	Bar	Dune	Bar	Palesoils	Bar	Channel	Sabkha	Sabkha
Porosity (%)	8.99	9.65	9.65	12.46	11.16	7.69	12.76	11.28	-	-
Mineralogy										
Quartz	93.68	73.7	94.76	94.89	92.64	70.83	82.61	8.21	11.47	2.15
Phyllosilicates	2.23	9.7	4.33	2.65	5.16	14.51	5.54	2.78	41.66	0.97
Feldspars	0	0	0	0.65	0	3.24	9.71	3.2	8.64	0.61
Carbonates	3.02	15.4	0.14	0.69	0	8.02	0.33	85.56	38.23	96.27
Sulfates	0	0	0	0	0	0	0	0.08	0	0
Others	1.07	1.2	0.77	1.12	2.2	3.4	1.81	0.17	0	0
Total	100	100	100	100	100	100	100	100	100	100

PR samples are of the Peñas Royas outcrop.



Samples	CHIPRANA 1743	CHIPRANA 1747,6	CHIPRANA 1752	CHIPRANA 1758	CHIPRANA 1764,5	CHIPRANA 1768	CHIPRANA 1773	CHIPRANA 1776	CHIPRANA 1788	CHIPRANA 1796,2	CHIPRANA 1816,2	CHIPRANA 1824,2
Depth (m)	1743	1747.6	1752	1758	1764.5	1768	1773	1776.8	1788	1796.2	1816.2	1824.2
Sedimentary Feature	Plannar X- Bedding	Trough X- Bedding	Plannar X- Bedding	Trough X- Bedding	Silt	Silt	Plannar X- Bedding	Trough X- Bedding	Plannar X- Bedding	Ripple	Trough X- Bedding	Trough X- Bedding
Facies	Fluvial Bar	Channel	Fluvial Bar	Channel	Flood plain	Flood plain	Bar	Channel	Bar	Bar	Bottom Channel	Bottom Channel
Porosity (%)	8.92	11.15	9.11	14.18	3.26	5.49	3.51	13.20	2.58	7.29	17.30	17.72
Mineralogy												
Quartz	85.46	77.41	56.41	85.2	29.63	43.48	65.98	88.86	80.31	93.76	88.15	86.69
Phyllosilicate s	5.26	6.59	15.36	6.96	14.15	42.02	25.36	5.73	10.49	3.27	8.89	3.51
Feldspars	6.45	11.49	25.84	2.11	1.83	5.15	3	2.92	8.16	0.95	1.67	6.68
Carbonates	0	0	0	0	50.15	0	0	0	0	0	0.07	0
Sulfates	2.5	2.96	0.02	5.73	0	0	0	1.72	0	2.02	0.19	3.12
Others	0.33	1.55	2.37	0	4.24	9.35	5.66	0	1.04	0	1.03	0
Total	99.67	100	100	100	100	100	100	99.23	100	100	100	100

Samples are of the Chiprana borehole.



9.8 Seal Facies

9.8.1 Stratigraphy

Röt facies or Rané formation (Arche et al., 2004) is the possible seal. It is formed by alternating shales and fine-grained red sandstones. Shales tend to be thicker towards the top. The fluvial sedimentation of sandstones and siltstones stops fairly abruptly and changes to interbedded, very fine to fine grained sandstone with mud and siltstone. The thickness of the individual beds varies from 5 to 10 cm and sandstone content decreases towards the top. This transition zone from continental to marine sedimentation also includes minor gypsum horizons within the mudstones (Figure 9-75), which are indicative of a periodical evaporation of sea water and a nearshore interplay of short-term marine transgression and regression.

In the field analogues, the bottom of Rané formation is composed by clay (smectite, chlorite and kaolinite) and carbonate (calcite and dolomite).

The thickness of this heterolithic unit had reached 15–40 m, from Peñarroyas to Ebro 1 well. The reduced thickness of unit is indicative of the transgression reaching its landward limit of progradation (Figure 10-1).

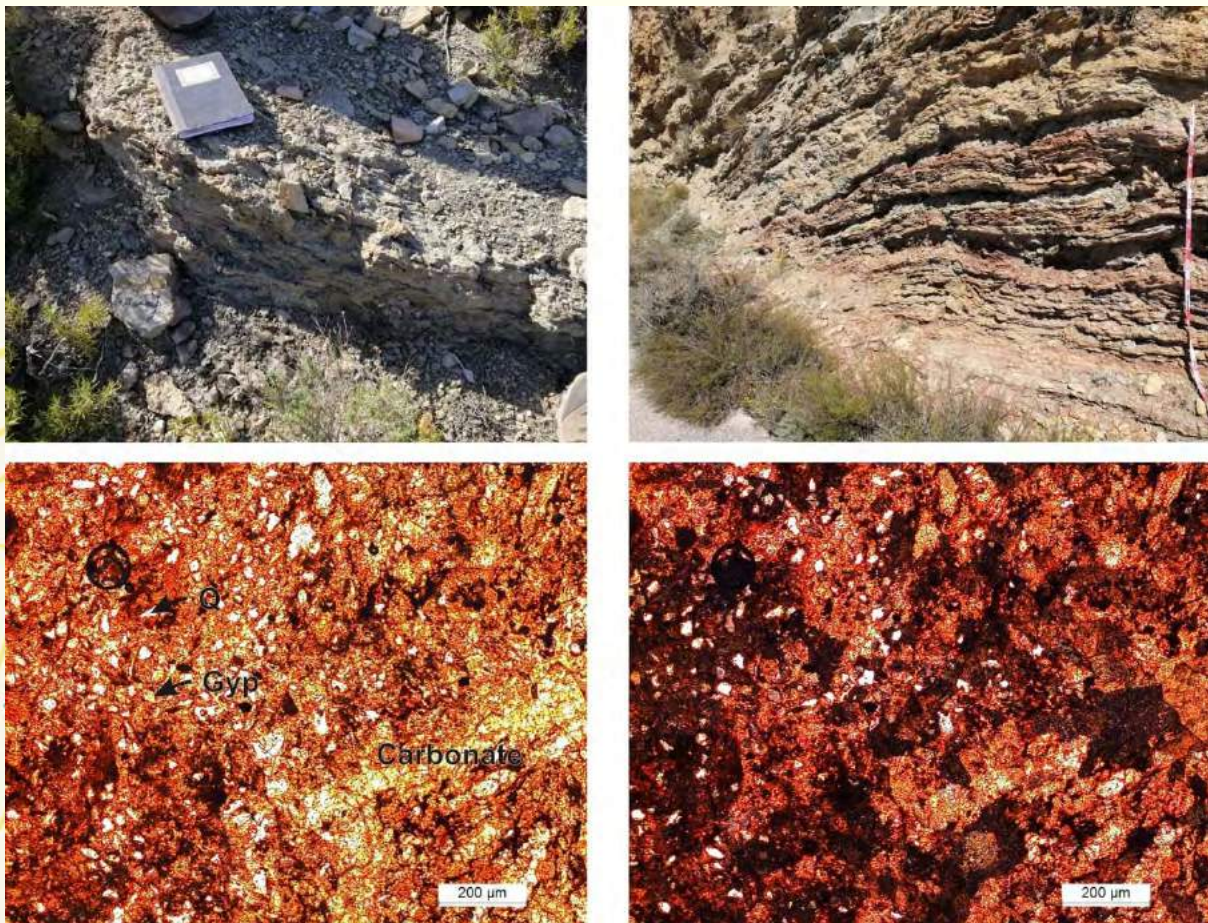


Figure 9-75 a) Marls, Peña Royas site; b) Carbonate layers, Torre de Arcas site; c) Microphotography of dolomite and gypsum.

9.8.2 Seal Properties.

In the XRD analysis, it is composed by quartz and phyllosilicates. In field samples, anhydrite appears as a trace mineral replaced by calcite or dolomite, but analysis carried out in the Monegrillo-1 borehole, to the north of the Lopín structure, indicate its common presence. Likewise, electrofacies analysis (Rueda, 2022) shows that the GR has serrated curves and varied geometries. In the case of Chiprana-1, Caspe-1 and Ebro-2, it is cylindrical, indicated shales with anhydrite and sandstone intercalations.

9.9 Surface Data

It is included in chapter of facies description. We have used the typical tools of the Basin analysis.

10. Depositional environments and geological conceptual model

Buntsandstein Facies from bottom to top is composed of: Aranda Formation or Unit B1, which corresponds with fluvial braided; Carcalejo Formation (Unit B2) which represents isolated fluvial systems with flood plain; and Rané Formation (included in Unit B2) which represents transition to sabkha lake facies (Figure 9-73 and Figure 10-1). It constitutes the first major cycle of the Buntsandstein observed in that area similar to Aragonian Branch of Iberian Range (Diez et al., 2007), is characterized by fluvial system and lacustrine deposits. According to Arche et al. (2004), this cycle can be attributed to the Late Permian. These authors considered it as the second depositional cycle of the Permo-Triassic in the Central and NE Iberian domain, and attributed its basal unconformity to the Saalian and Pfalzic unconformities of western Europe.

Unit B1 is formed by the following facies associations:

- **Channel fill deposits:** ≈1,5-m thick, with cross stratification, fine to medium grained, presence of intraclast, typically scour-based and fine-upwards. They have an extension of several hundred meters to several kilometres. There are mainly two main subunits of channel facies at the base and at the top of unit B1. The top subunit has a much larger grain size, with the appearance of muscovite and the polycrystalline quartz gradually vanishing, it is possibly because there was a change in the origin of the sands. It is frequent the presence of crevasse splay deposits because the channels are not embedded and overflows are common.
- **Sheetflood deposits:** ≈10m thick, low angle and planar laminated, fine-grained, presence of current-ripples, dewatering structures, rare burrows and root traces. It is possibly the most common environment in field outcrops, but in the Chiprana-1 wellbore they pass laterally to shallow lacustrine environments of green marls.
- **Aeolian Deposits:** <2m intervals, well-sorted, fine-grained sandstones, grading laterally and vertically to sheetflood deposits.
- **Lacustrine deposits:** heterolithic, abundant wave-ripples, mud-cracks, and locally root traces.

Unit B2 is formed by the following facies associations:

- **Channel fill deposits:** ≈2-5m thick, with cross stratification, fine to coarse grained, presence of intraclast, typically scour-based and fine-upwards. They have an extension of several hundred meters.
- **Floodplain deposits:** <10m intervals of siltstone and very fine to fine grained sandstones, planar, ripple and wave-ripple laminations, root traces. Carbonate paleosols may develop.

Rané Fm or seal is composed by:

- **Lacustrine coastal deposits:** heterolithic, abundant wave-ripples, root traces, mud-cracks and evaporites. In analogues field is composed by dolomite and carbonate with tepee structure.

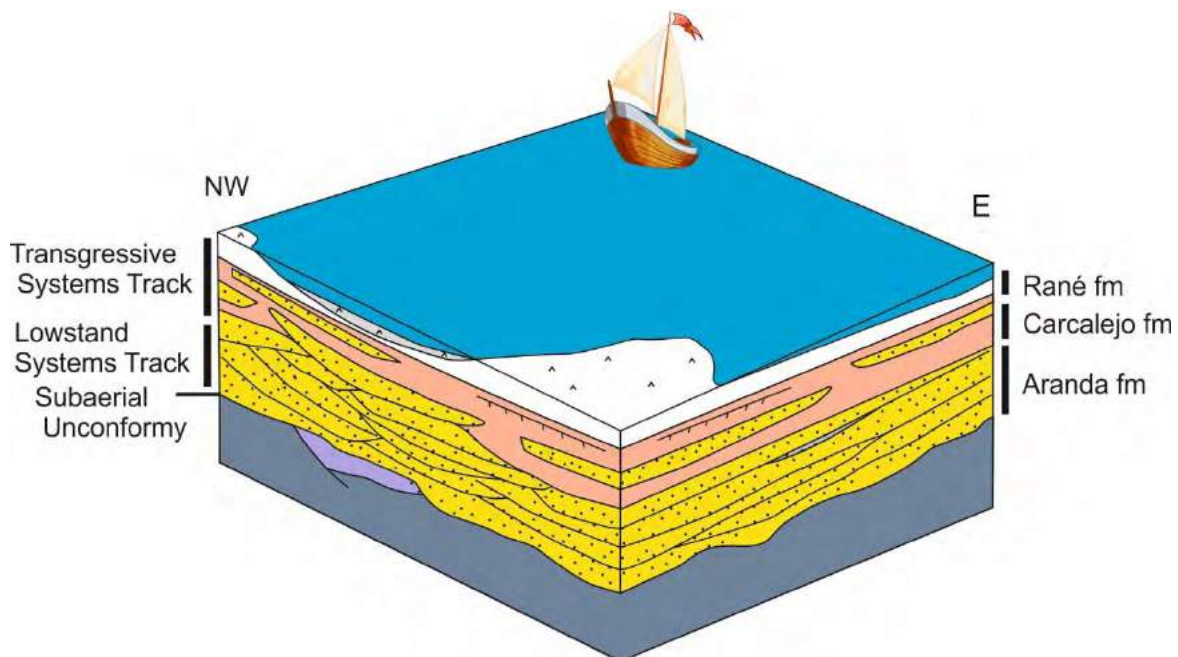


Figure 10-1 Representative stacking model of Buntsandstein facies. It shows the progressive transgressive from the east to west.

10.1 Field Analogues

Three analogues have been considered for this basin: Berkine Basin TAGI (Algeria), Wytch Farm Field-Sherwood Sandstone (UK) and Lower Triassic Buntsandstein (European Central Basin).

Reservoir	Setting	Main Structure	Sedimentology	Boundaries/traps
TAGI	After Variscan orogeny, extensional basin (erosive unconformity), tectonic inversion in the Alpine orogeny	NE-SW, NW-SE, basement lineaments	Semi-arid conditions Fluvio-lacustrine facies. Fairway to NE.	Sealing Faults, sealing facies at top (TAC lacustrine and shallow marine shales, salts). Alpine folds structures. Stratigraphic traps.
Sherwood SST	After Variscan orogeny, extensional basin (erosive unconformity), tectonic inversion in the Alpine orogeny	Orientation W-E. subdivided in sub-basins by normal faults with several depocentres.	100-300m thick, semi-arid conditions, fluvial braided, alluvial fans, occasionally aeolian. Fairway to the NE.	Sealing Faults, dip-closing, sealing facies at top (300-800m thick mudstones). Alpine folds structures.
L. Triassic Buntsandstein (ECB)	After Variscan orogeny, extensional basin (erosive unconformity), tectonic inversion in the Alpine orogeny	Complex W-E striking basin	Arid to Semi-arid. Braided-meandering rivers to playa lakes and hypersaline endorheic sea toward the basin	Grenzletten mudstones Keuper evaporitic mudstones.

			centre. Aeolian toward basin borders.	
--	--	--	---------------------------------------	--

Reservoir	ϕ/K	N/G-Kv/Kh	Petrology	P/T
TAGI	$\Phi=17-20\%$ K= 0.1-1000mD	Huge variations, frequent shale interbedding.	well sorted fine- to medium-grained quartzarenites.	n/a
Sherwood SST	$\Phi=14-23\%$ (Avg: 18%) K= 1-1500mD	0.45-0.95 (Avg: 0.7) Kv/Kh=0.001 (max: 0.1)	well-sorted, fine- to coarse-grained arkosic sandstones and conglomerates	At 1530m SS: 168 bars 66°C
L. Triassic Buntsandstein (ECB)	$\Phi=7.9-21.5\%$ K= 0.001-515mD (Avg: 40)	n/a	fine- to medium-grained poor sorted Arkoses. Occ. well sorted aeolian quartzarenites	n/a

Reservoir	Salinity	Reservoir Quality	Others	
TAGI	Cl- 5 (to south) to >250 g/L (to north)	Control: sandstones source rocks (Clay content), Q cements, Dolomite cements (fault linked)	Sandbodies linked to fluvial channels (braided to anastomosed)	
Sherwood SST	Cl- 109 to 136 g/L	Controls: grain size, sorting and detritical clay .	Vertically and laterally compartmentalization.	
L. Triassic Buntsandstein (ECB)	n/a	Controls: widely vary, even at very short distances, sedimentology, composition and diagenesis. Grain size, grains composition and Q-cements.	quite heterogeneous, varying and interfingering depositional settings	

11. References

Ábalos, B., Carreras, J., Druguet, E., Escuder, J., Gómez-Pugnaire, M.T., Lorenzo Álvarez, S., Quesada, C., Rodríguez-Fernández, R. and Gil-Ibarguchi J. I. 2002. Variscan and Pre-Variscan tectonics. In: Gibbons W, Moreno T (eds) *The Geology of Spain*. Geological Society, London, Special Publications, 155-183, <http://doi.org/10.1144/GOSP.9>

Angrand, P., Mouthereau, F., Masini, E., Asti, R. 2020. A reconstruction of Iberia accounting for Western Tethys–North Atlantic kinematics since the late-Permian–Triassic. *Solid Earth*, 11(4), 1313-1332.

Arche, A., Gómez, J. L., Marzo, M., & Vargas, H., 2004. The siliciclastic Permian-Triassic deposits in Central and northeastern Iberian Peninsula (Iberian, Ebro and Catalan basins): a proposal for correlation. *Geologica Acta*, 305-305.

Archie, G.E. 1942. The Electrical Resistivity as an Aid in Determining Some Reservoir Characteristics. *J. Pel. Tech.* (Jan) 5, No. 1.

Arenillas, A., Mediato, J. F., García Crespo, J., Nita, R., Molinero, R., G^a Lobón, J.L., Heredia, N, Marín, C., López, F.L., Pueyo, E.L., Martínez-Orio, R., et al. 2014. Atlas de estructuras del subsuelo susceptibles de almacenamiento geológico de CO₂ en España. ISBN: 978-84-7840-935-8; 211 pp.

Arlegui, L. and Simón, J.L. 2001. Geometry and distribution of regional joint sets in a non-homogeneous stress field: case study in the Ebro basin (Spain). *J. Struct. Geol.* 23, 297–313.

Arribas, J., 1984. Sedimentología y diagénesis del Buntsandstein y Muschelkalk de la Rama Aragonesa de la Cordillera Ibérica (provincias de Soria Zaragoza). Tesis Doctoral. Universidad Complutense de Madrid. 354 pp.

Arribas, J., 1985. Base litoestratigráfica de las facies Buntsandstein y Muschelkalk en la Rama Aragonesa de la Cordillera Ibérica (Zona Norte). *Estudios Geológicos* 41, 47-57

Aurell, M., Bádenas, B., Casas, A., & Alberto, S., 2001. La Geología del Parque Cultural del Río Martín. Asociación Parque Cultural del río Martín.

Ayala, C., Torné, M. and Pous, J., 2003, The lithosphere-asthenosphere boundary in the western Mediterranean from 3D joint gravity and geoid modelling: tectonic implications. *Earth and Planetary Science Letters*, 209, 3-4, pp 275-290

Ayala, C., Rubio, F. M. and Rey-Moral, C. 2011. Caracterización microgravimétrica de la estructura geológica seleccionada para Planta de Desarrollo Tecnológico de Almacenamiento Geológico de CO₂ en Hontomín (Burgos). [Confidential]. Fondo documental del IGME, Código 64091. 44 pp.

Ayala, C., Benjumea, B., Mediato, J. F., García-Crespo, J., Clariana, P., Soto, R., Rubio, F., Rey-Moral, C., Pueyo, E. L., Martín-León, J., García, A. G., Fernández-Canteli, P., Martínez-Orio, R. 2022. DeveLopíng a new innovative methodology to integrate geophysical techniques into characterization of potential CO₂ storage sites: Lopín structure (southern Ebro Basin, Spain). *Geological Society, London, Special Publications*, 528 (1). <https://doi.org/10.1144/SP528-2022-70>

Benjumea, B., Macau, A., Gabàs, A., Bellmunt, F., Figueras, S. and Cirés, J. 2011. Integrated geophysical profiles and H/V microtremor measurements for subsoil characterization. *Near Surface Geophysics*, 9 (5), 413-425, DOI: <https://doi.org/10.3997/1873-0604.2011021>

Bonnefoy-Claudet, S., Cotton, F., & Bard, P. Y. 2006. The nature of noise wavefield and its applications for site effects studies: A literature review. *Earth-Science Reviews*, 79(3-4), 205-227.

Brocher, T. M. 2005. Empirical relations between elastic wavespeeds and density in the Earth's crust. *Bulletin of the seismological Society of America*, 95 (6), 2081-2092, DOI:10.1785/0120050077

Butillé, M., Ferrer, O., Granado, P., Roca, E., Muñoz, J.A., Ballesteros, J.C., Gimenez, A., Vallejo, R.A., González, P., 2012. Evidencias de deformaciones salinas en las sucesiones mesozoicas del sector sur de la Cuenca del Ebro, 13. *Geotemas*, p. 176.

Casas-Sainz, A.M. and Faccenna, C. 2001. Tertiary compressional deformation of the Iberian plate. *Terra Nova* 13, 281–288.

Colomer i Guilera, V., Navarro-Juli, J.J., Hernández-Samaniego, A., Ramírez-Merino, J.I. 1994. Mapa Geológico de España E. 1:50.000, Hoja 412 (Pina de Ebro), 2^a Serie MAGNA. Instituto Geológico y Minero de España, Madrid.

Cortés, A.L. and Casas, A.M. 1996. Deformación Alpina del zócalo y cobertera en el borde norte de la Cubeta de Azuara (Cordillera Ibérica). *Revista de la Sociedad Geológica de España*, 9 (1-2), 55-66.

Cortés, A.L. and Casas, A.M. 1999. Estructura y cinemática de los pliegues y cabalgamientos de Belchite-Sierra de Arcos (Cordillera Ibérica). *Cuadernos de Geología Ibérica*, número 25, 213-227.

Cortés, A.L.; Liesa, C.L., Soria, A.R., Meléndez, A. 1999. Role of extensional structures in the location of folds and thrusts during tectonic inversion (Northern Iberian Chain). *Geodinámica Acta*, 12(2) 113-132.

Cuevas-Martínez, J.L. 2022. La Formación Caspe: análisis sedimentológico y estratigráfico de los depósitos fluviales del Oligoceno – Mioceno inferior del SE de la Cuenca del Ebro. Tesis doctoral, Universitat de Barcelona, 273pp.

Díez, J. B., Bourquin, S., Broutin, J., & Ferrer, J., 2007. The Iberian Permian Triassic ‘Buntsandstein’ of the Aragonian Branch of the Iberian Range (Spain) in the West-European sequence stratigraphical framework: a combined palynological and sedimentological approach. *Bulletin de la Société Géologique de France*, 178(3), 179-195.

Gabàs, A., Macau, A., Benjumea, B., Queralt, P., Ledo, J., Figueras, S. and Marcuello, A. 2016. Joint audio-magnetotelluric and passive seismic imaging of the Cerdanya Basin. *Surveys in Geophysics*, 37 (5), 897-921. DOI:10.1007/s10712-016-9372-4

García Lobón, J.L., Reguera, M.I., Martín León, J., Rey Moral, C. and Berrezueta, E.R. 2010. Plan de selección y caracterización de áreas y estructuras favorables para el almacenamiento geológico de CO2 en España: Resumen ejecutivo. IGME, 76 pp.

García-Quintana, A. 1977. Jurásico terminal y Cretácico inferior en la región central de la provincia de Valencia y noreste de la provincia de Albacete. *Seminario de Estratigrafía*. Serie Monográficas, 1, 1-334.

Girard, A. J., & Shragge, J. 2020. Automated processing strategies for ambient seismic data. *Geophysical Prospecting*, 68, 293-312. Romero, P., & Schimmel, M. [2018]. Mapping the basement of the Ebro Basin in Spain with seismic ambient noise autocorrelations. *Journal of Geophysical Research: Solid Earth*, 123, 5052–5067.

Gomez, J.J., Goy, A. and Barron, E. 2007. Events around the Triassic-Jurassic boundary in northern and eastern Spain. A review. *Palaeogeography, Palaeoclimatology, Palaeoecology*, 244, 89-110, DOI:10.1016/j.palaeo.2006.06.025

González, A. 1989. Análisis Tectosedimentario Del Terciario Del Borde SE de La Depresión Del Ebro (Sector Bajoaragonés) y Cubetas Ibéricas Marginales. Tesis doctoral, Universidad de Zaragoza, 507 pp.

Greenberg, M. L. and Castagna, J. P. 1992. Shear-wave velocity estimation in porous rocks: theoretical formulation, preliminary verification and applications1. *Geophysical prospecting*, 40 (2), 195-209, DOI/10.1111/j.1365-2478.1992.tb00371.x

Guimerà, J. 2018. Structure of an intraplate fold-and-thrust belt- The Iberian Chain. A synthesis. *Geologica Acta*, 16, 427–438, doi: 10.1344/GeologicaActa2018.16.4.6.

Guimerà, J. and Álvaro, M., 1990. Structure et évolution de la compression alpine dans la Chaîne Ibérique et la Chaîne Côtière Catalane (Espagne). *Bull. Soc. Géol. Fr.* 8 (VI), 339–348.

Hernández-Samaniego, A. and Ramírez-Merino, J.I. 1993. Mapa Geológico de España E. 1:50.000, Hoja 441 (Hijar), 2ª Serie MAGNA. Instituto Geológico y Minero de España, Madrid.

Horner, D. R., 1951. Pressure build-up in wells, Proc. Third World Petroleum Congress, 34, 316, The Hague.

Iaffa, D. N., Sàbat, F., Bello, D., Ferrer, O., Mon, R., Gutierrez, A. A. 2011. Tectonic inversion in a segmented foreland basin from extensional to piggy back settings: The Tucumán basin in NW Argentina. *Journal of South American Earth Sciences*, 31(4), 457-474.

Ibs-von Seht, M. and Wohlenberg, J. 1999. Microtremor measurements used to map thickness of soft sediments. *Bulletin of the Seismological Society of America* 89 (1), 250–259, <https://doi.org/10.1785/BSSA0890010250>

ITGE, 1990. Documentos sobre la Geología del subsuelo de España. Tomo VI: Ebro-Pirineos. ITGE, Madrid.

Izquierdo-Llavall, E.; Ayala, C.; Rodríguez Pintó, A.; Pueyo, E.L.; Oliva-Urcia, B.; Casas, A.M.; Rubio, F.M.; García Crespo, J.; Llorente Delgado, J.M.; González Durán, A.; Suárez, I.; Rey Moral, C.; Mediato Arribas, J.F.; Pérez Ortiz, I. 2015. Informe de la investigación del reservorio potencial de CO₂ “Zona de Enlace” (Cordilleras Ibérica y Costero Catalanas), 229 pp. Instituto para la Reestructuración de las Comarcas Mineras (Ministerio de Industria).

Izquierdo-Llavall, E., Ayala, C., Pueyo, E.L., Casas, A.M., Oliva-Urcia, B., Rubio, F., Rodríguez-Pintó, A., Rey-Moral, C., Mediato, J.F. and García-Crespo, J. 2019. Basement-cover relationships and their along-strike changes in the Linking Zone (Iberian Range, Spain): a combined structural and gravimetric study. *Tectonics*, 38, 2934-2960, DOI: 10.1029/2018TC005422

Jurado, M.J., 1990. El Triásico y Liásico basal evaporíticos del subsuelo de la cuenca del Ebro. In: Ortí, F., Salvany, J.M. (Eds.), *Formaciones evaporíticas de la Cuenca del Ebro y cadenas periféricas y de la zona de Levante*. Enresa, pp. 21–28.

King, M. T., Welford, J. K., Tugend, J. 2023. The role of the Ebro Block on the deformation experienced within the Pyrenean realm: Insights from deformable plate tectonic models. *Journal of Geodynamics*, 155, 101962.

Klimowitz, J., 1992. Estratigrafía y disposición estructural del Terciario Inferior en el subsuelo del Sector Central de la Cuenca del Ebro. *Acta Geol. Hisp.* 27 (1–2), 117–125.

Konno, K. & Ohmachi, T., 1998. Ground-motion characteristics estimated from spectral ratio between horizontal and vertical components of microtremor, *Bull. seism. Soc. Am.*, 88, 228–241.

Lanaja, J. M., 1987. Contribución de la exploración petrolífera al conocimiento de la Geología de España. Instituto Geológico y Minero de España Ed., 465 pp., 17 mapas.

Letouzey, J., Werner, P., Marty, A. 1990. Fault reactivation and structural inversion. Backarc and intraplate compressive deformations. Example of the eastern Sunda shelf (Indonesia). *Tectonophysics*, 183(1-4), 341-362.

López-Gómez, J., Alonso-Azcárate, J., Arche, A., Arribas, J., Fernández Barrenechea, J., Borrueal-Abadía, V. (...) Ángela Suárez-Rodríguez, A., Tubía, J.M., Ubide, T., Valero Garcés, B., Vargas, H. and César Viseras, C. 2019. Permian-Triassic Rifting Stage. *The Geology of Iberia: A Geodynamic Approach*, C.

Quesada and J. T. Oliveira (eds.), *Regional Geology Reviews*, 29-112 https://doi.org/10.1007/978-3-030-11295-0_3

Mediato, J. F., García-crespo, J., Izquierdo, E., García-lobón, J. L., Ayala, C., Pueyo, E. L. & Molinero, R. 2017. Three-dimensional reconstruction of the Caspe geological structure (Spain) for evaluation as a potential CO₂ storage site. *Energy Procedia*, 00, 14–18.

Nakamura, Y., 2000. Clear identification of fundamental idea of Nakamura's technique and its applications, *Proceedings of the 12th World Conference on Earthquake Engineering*, Auckland, New Zealand.

Ortí, F., Pérez-López, A. and Salvany, J. A. 2017. Triassic evaporitic of Iberia: Sedimentological and palaeogeographical implications for the western Neotethys evolution during the Middle Triassic-Earliest Jurassic. *Palaeogeography, Palaeoclimatology, Palaeoecology*, 471, 157–180, <https://doi.org/10.1016/j.palaeo.2017.01.025>

Pardo, A., Arenas, C., González, A., Luzón, A., Muñoz, A., Pérez, A., Perez-Rivarés, F.J., Vázquez-Urbez, M. y Villena, J. 2004: La Cuenca del Ebro. En: *Geología de España*. (J.A. Vera ed.). SGE-IGME, Madrid, 533-542.

Pueyo, E. L., Izquierdo-Llavall, E., Rodríguez-Pintó, A., Rey-Moral, C., Oliva-Urcia, B., Casas, A. M., ... & Rubio, F. M. 2016. Petrophysical properties in the Iberian Range and surrounding areas (NE Spain): 1-density. *Journal of Maps*, 12(5), 836-844.

Quirantes, J., 1978. Estudio sedimentológico y estratigráfico del Terciario Continental de los Monegros. Publicación 681. Institución Fernando el católico (CSIC), Diputación de Zaragoza, 207 p.

Ramírez-Merino, J.I. 1991. Mapa Geológico de España E. 1:50.000, Hoja 413 (Gelsa), 2ª Serie MAGNA. Instituto Geológico y Minero de España, Madrid.

Raymer, L.L., Hunt, E.R., and Gardner J.S., 1980. An Improved Sonic Transit Time-To-Porosity Transform. Paper presented at the SPWLA 21st Annual Logging Symposium, Lafayette, Louisiana, July 1980

Romero, P. and Schimmel, M. 2018. Mapping the basement of the Ebro Basin in Spain with seismic ambient noise autocorrelations. *Journal of Geophysical Research: Solid Earth*, 123, 5052–5067.

Rueda Fort, M., 2022. Caracterización a partir de diagráfia del posible almacén de CO₂ de Lopín. Trabajo Fin de Master, Universidad Complutense de Madrid, 57 pp

Ruiz, V. and Lendínez, A. 1986. Mapa Geológico de España E. 1:50.000, Hoja 440 (Belchite), 2ª Serie MAGNA. Instituto Geológico y Minero de España, Madrid.

Salas, R., Guimera, J., Mas, R., Martín-Closas, C., Meléndez, A., Alonso, A., 2001. Evolution of the Mesozoic Central Iberian Rift System and its cainozoic inversion (Iberian Chain). In: Ziegler, P.A., Cavazza, W., Robertson, A.H.F., Crasquin-Soleau, S. (Eds.), *Peri-Thetys Memoir 6: Peri-Thetyan Rift/Wrench Basins and Passive Margins*. Mem. Mus. Nac. Hist. Nat., vol. 186, pp. 145–185.

Schimmel M., 1999, Phase cross-correlations: design, comparisons and applications, *Bull. Seismol. Soc. Am.*, 89, 1366-1378.

Schimmel, M., & Gallart, J. 2007. Frequency-dependent phase coherence for noise suppression in seismic array data. *Journal of Geophysical Research*, 112, B04303. <https://doi.org/10.1029/2006JB004680>.

Schlumberger (2009) "Log interpretation Charts", Schlumberger, p279

Sopeña, A., López-Gómez, J., Arche, A., Pérez-Arlucea, M., Ramos, A., Virgili, C., Hernando, S., 1988. Permian and Triassic Rift basins of the Iberian Peninsula. In: Manspeizer, W. (Ed.), *Triassic-Jurassic Rifting. Continental Breakup and the Origin of the Atlantic Ocean and Passive Margins*. Elsevier, Amsterdam, pp. 757–786.

Soto, R., Casas-Sainz, A. M., & Del Río, P. 2007. Geometry of half-grabens containing a mid-level viscous décollement. *Basin Research*, 19(3), 437-450.

Soto, R., Larrasoña, J. C., Arlegui, L. E., Beamud, E., Oliva-Urcia, B., Simón, J. L. 2009. Reliability of magnetic fabric of weakly deformed mudrocks as a palaeostress indicator in compressive settings. *Journal of Structural Geology*, 31(5), 512-522.

Soto, R., Juan C. Larrasoña, J.C., Beamud, E., Garcés, M. 2016. Early–Middle Miocene subtle compressional deformation in the Ebro foreland basin (northern Spain); insights from magnetic fabrics. *C. R. Geoscience* 348, 213–223

Soto, R., Casas-Sainz, A. M., Oliva-Urcia, B., García-Lasanta, C., Izquierdo-Llavall, E., Moussaid, B., et al. 2019. Triassic stretching directions in Iberia and North Africa inferred from magnetic fabrics. *Terra Nova*, 31(5), 465-478.

Talwani, M., Worzel, J. L., & Landisman, M. 1959. Rapid gravity computations for two-dimensional bodies with application to the Mendocino submarine fracture zone. *Journal of geophysical research*, 64(1), 49-59.

Talwani, M., and Heirtzler, J. R., 1964, Computation of magnetic anomalies caused by two-dimensional bodies of arbitrary shape, in Parks, G. A., Ed., *Computers in the mineral industries, Part 1: Stanford Univ. Publ., Geological Sciences*, 9, 464-480.

Tugend, J., Manatschal, G., Kuszniir, N. J., Masini, E., Mohn, G., Thion, I. 2014. Formation and deformation of hyperextended rift systems: Insights from rift domain mapping in the Bay of Biscay-Pyrenees. *Tectonics*, 33(7), 1239-1276.

Vera, J.A. 2004. *Geología de España*. Sociedad Geológica de España-Instituto Geológico y Minero de España, 884 p. Madrid.

Villa, E., Escuder, J. & Ginkel, A. C. 1996. Fusulináceos y edad de los afloramientos carboníferos de Puig Moreno (Cordillera Ibérica, Teruel, España). *Spanish Journal of Palaeontology*, 11, 207–215.

Villena, J., González, A., Muñoz, J. A., Pardo, G. & Pérez, A. 1992. Síntesis estratigráfica del Terciario del borde Sur de la Cuenca del Ebro: unidades genéticas. *Acta geológica hispánica*, 27, 225–245.

Wathelet, M., Chatelain, J.-L., Cornou, C., Di Giulio, G., Guillier, B., Ohrnberger, M. and Savvaidis, A. 2020. Geopsy: A User-Friendly Open-Source Tool Set for Ambient Vibration Processing. *Seismological Research Letters*, 91(3), 1878--1889, doi: 10.1785/0220190360.

Won, I. J., and Bevis, M., 1987, Computing the gravitational and magnetic anomalies due to a polygon: Algorithms and Fortran subroutines, *Geophysics*, 52, 232-238.

Wyllie, M. R. J., Gregory, A. R., Gardner, G. H. F., 1958. An experimental investigation of factors affecting elastic wave velocities in porous media. *Geophysics*; 23 (3): 459–493.

